Control and optimization methodologies to enable the energy and ancillary services through microgrids

Politecnico di Bari

Department of Electrical and Information Engineering

Electrical and Information Engineering

Ph.D. Program

SSD: ING-IND/33-Electrical Energy Systems

Final Dissertation

Control and Optimization Methodologies to Enable the Energy and Ancillary Services through Microgrids

---

by

Muhammad Muzammal Islam

Supervisor:
Prof. Massimo LA SCALA

Co-Supervisor:
Prof. Maria Dicorato

Coordinator of Ph.D. Program:
Prof. Mario Carpentieri

XXXVII Cycle - November 1st, 2021 - October 31st, 2024

LIBERATORIA PER L'ARCHIVIAZIONE DELLA TESI DI DOTTORATO

Al Magnifico Rettore
del Politecnico di Bari

Il/la sottoscritto/a Muhammad Muzammal Islam nato/a a Faisalabad, Pakistan il 15/10/1994

residente a BARI (BA) in via STRADELLA PETRERA, 4/H e-mail muzammalislam3232@gmail.com

iscritto al III° anno di Corso di Dottorato di Ricerca in Ingegneria Elettrica e dell'Informazione ciclo XXXVII

ed essendo stato ammesso a sostenere l'esame finale con la prevista discussione della tesi dal titolo:

Control and optimization methodologies to enable the energy and ancillary services through microgrids

DICHIARA

1) di essere consapevole che, ai sensi del D.P.R. n. 445 del 28.12.2000, le dichiarazioni mendaci, la falsità negli atti e l'uso di atti falsi sono puniti ai sensi del codice penale e delle Leggi speciali in materia, e che nel caso ricorressero dette ipotesi, decade fin dall'inizio e senza necessità di nessuna formalità dai benefici conseguenti al provvedimento emanato sulla base di tali dichiarazioni;
2) di essere iscritto al Corso di Dottorato di ricerca Ingegneria Elettrica e dell'Informazione ciclo XXXVII, corso attivato ai sensi del "*Regolamento dei Corsi di Dottorato di ricerca del Politecnico di Bari"*, emanato con D.R. n.286 del 01.07.2013;
3) di essere pienamente a conoscenza delle disposizioni contenute nel predetto Regolamento in merito alla procedura di deposito, pubblicazione e autoarchiviazione della tesi di dottorato nell'Archivio Istituzionale ad accesso aperto alla letteratura scientifica;
4) di essere consapevole che attraverso l'autoarchiviazione delle tesi nell'Archivio Istituzionale ad accesso aperto alla letteratura scientifica del Politecnico di Bari (IRIS-POLIBA), l'Ateneo archivierà e renderà consultabile in rete (nel rispetto della Policy di Ateneo di cui al D.R. 642 del 13.11.2015) il testo completo della tesi di dottorato, fatta salva la possibilità di sottoscrizione di apposite licenze per le relative condizioni di utilizzo (di cui al sito http://www.creativecommons.it/Licenze), e fatte salve, altresì, le eventuali esigenze di "embargo", legate a strette considerazioni sulla tutelabilità e sfruttamento industriale/commerciale dei contenuti della tesi, da rappresentarsi mediante compilazione e sottoscrizione del modulo in calce (Richiesta di embargo);
5) che la tesi da depositare in IRIS-POLIBA, in formato digitale (PDF/A) sarà del tutto identica a quelle **consegnate**/inviate/da inviarsi ai componenti della commissione per l'esame finale e a qualsiasi altra copia depositata presso gli Uffici del Politecnico di Bari in forma cartacea o digitale, ovvero a quella da discutere in sede di esame finale, a quella da depositare, a cura dell'Ateneo, presso le Biblioteche Nazionali Centrali di Roma e Firenze e presso tutti gli Uffici competenti per legge al momento del deposito stesso, e che di conseguenza va esclusa qualsiasi responsabilità del Politecnico di Bari per quanto riguarda eventuali errori, imprecisioni o omissioni nei contenuti della tesi;
6) che il contenuto e l'organizzazione della tesi è opera originale realizzata dal sottoscritto e non compromette in alcun modo i diritti di terzi, ivi compresi quelli relativi alla sicurezza dei dati personali; che pertanto il Politecnico di Bari ed i suoi funzionari sono in ogni caso esenti da responsabilità di qualsivoglia natura: civile, amministrativa e penale e saranno dal sottoscritto tenuti indenni da qualsiasi richiesta o rivendicazione da parte di terzi;
7) che il contenuto della tesi non infrange in alcun modo il diritto d'Autore né gli obblighi connessi alla salvaguardia di diritti morali od economici di altri autori o di altri aventi diritto, sia per testi, immagini, foto, tabelle, o altre parti di cui la tesi è composta.

Luogo e data BARI, 02/01/2025 Firma _____

Il/La sottoscritto, con l'autoarchiviazione della propria tesi di dottorato nell'Archivio Istituzionale ad accesso aperto del Politecnico di Bari (POLIBA-IRIS), pur mantenendo su di essa tutti i diritti d'autore, morali ed economici, ai sensi della normativa vigente (Legge 633/1941 e ss.mm.ii.),

CONCEDE

- al Politecnico di Bari il permesso di trasferire l'opera su qualsiasi supporto e di convertirla in qualsiasi formato al fine di una corretta conservazione nel tempo. Il Politecnico di Bari garantisce che non verrà effettuata alcuna modifica al contenuto e alla struttura dell'opera.
- al Politecnico di Bari la possibilità di riprodurre l'opera in più di una copia per fini di sicurezza, back-up e conservazione.

Luogo e data BARI, 02/01/2025 Firma _____

Politecnico di Bari

Department of Electrical and Information Engineering

Electrical and Information Engineering

Ph.D. Program

SSD: ING-IND/33-Electrical Energy Systems

Final Dissertation

Control and Optimization Methodologies to Enable the Energy and Ancillary Services through Microgrids

---

by

Muhammad Muzammal Islam

Supervisor:
Prof. Massimo LA SCALA

Co-Supervisor:
Prof. Maria Dicorato

Coordinator of Ph.D. Program:
Prof. Mario Carpentieri

XXXVII Cycle - November 1st, 2021 - October 31st, 2024

Contents

List of Figures

List of Tables

Abstract

This doctoral thesis presents the results of the author's research conducted during the three-year activities of the XXXVII cycle of the Ph.D Program in Electrical and Information Engineering at Politecnico di Bari, Italy. The primary objective of this research was to develop and explore control and optimization methodologies for enabling energy and ancillary services through microgrids, with the goal of enhancing their reliability and stability. Furthermore, the research focused on facilitating the integration of renewable energy sources, ensuring their secure and stable operation, minimizing overall system operational costs, and maintaining synthetic inertia to reduce the rate of change of frequency, all while meeting load demands.

Control and optimization methodologies for microgrids have been extensively studied, ranging from optimal resource management to the dynamic control of microgrid components. These studies primarily focus on microgrid operations in both islanded and grid-connected modes. Within the proposed framework, robust control and optimization methodologies have been developed to manage demand response, enable ancillary services, and implement high-level hierarchical control. These methodologies address hierarchical control levels, encompassing short-term dynamics and long-term scheduling, and provide comprehensive strategies for achieving optimal coordination and energy trading among multi-microgrids. Furthermore, these robust control and optimization approaches have been analyzed to enhance frequency and voltage regulation, enabling the synthetic inertia, while also accounting for system uncertainties. To tackle challenges related to power converter control actions, such as grid-forming control for frequency regulation, this thesis introduces a novel variational control approach based on the modified Bolza problem. This method enhances active optimal control capabilities in power electronic systems, significantly improving frequency regulation in microgrids. Overall, the proposed control and optimization methodologies contribute to improving the reliability, security, and stability of microgrids, while also reducing operational costs and greenhouse gas emissions.

Acknowledgments

The research activities were made possible through financial support from Next Intelligence Research (NIR srl) company.
I extend my heartfelt gratitude to my Ph.D supervisors, Prof. Massimo La Scala and Prof. Maria Dicorato for their kind support, guidance, and encouragement throughout my PhD journey and for the cherished moments we shared. I am also thankful to everyone, both past and present, who has been part of the LabZERO Laboratory research group. I would like to express my sincere gratitude to Prof. Jie Wang and Prof. Lidan Zhou for giving me the opportunity to explore my research topics at the State Energy, Smart Grid R&D Center in Shanghai, within the Department of Electronic, Information, and Electrical Engineering at Shanghai Jiao Tong University, China. I am also grateful to the members of their research group for warmly welcoming me and enriching my experience abroad. I am thankful for the technical support from LabZERO at Politecnico di Bari, Italy, and the State Energy and Smart Grid R&D Center at Shanghai Jiao Tong University (Minhang Campus), whose resources, equipment, and software access enabled me to complete my research from start to finish. My deepest gratitude goes to my family, who always have supported and continue to believe in me, regardless of the challenges and choices I have faced. I also extend my thanks to my friends, whose presence throughout these three years of hard work has helped me navigate even the most stressful moments with greater peace of mind.

Author's Publications

Publications resulting from this research work are listed below in chronological order.

Conferences

1. S. Bruno, G. Giannoccaro, M. Muzammal Islam, C. Iurlaro, M. La Scala, M. Menga, and C. Rodio, "Control and power hardware-in-the-loop tests for low-inertia power systems," in *2022 AEIT International Annual Conference (AEIT)*, 2022, pp. 1–6

2. S. Bruno, G. Giannoccaro, M. M. Islam, C. Iurlaro, M. L. Scala, M. Menga, and C. Rodio, "Predictive control based energy management of a residential hybrid ac-dc nanogrid," in *2022 4th International Conference on Electrical Engineering and Control Technologies (CEECT)*, 2022, pp. 1183–1187

3. M. M. Islam, S. Bruno, C. Iurlaro, and M. La Scala, "Robust adaptive integral back-stepping control of fc-sc-battery and traction motor based hybrid electric vehicles," in *2022 AEIT International Annual Conference (AEIT)*, 2022, pp. 1–6

4. T. Yu, M. M. Islam, J. Wang, and M. L. Scala, "Robust optimization in energy management under ress uncertainties through bess integration," in *2023 5th International Conference on Electrical Engineering and Control Technologies (CEECT)*, 2023, pp. 85–91

5. M. M. Islam, T. Yu, M. L. Scala, and J. Wang, "Robust integral terminal sliding mode control for frequency regulation in islanded microgrids incorporating ress and hess using a disturbance observer," in *5th International Conference on Electrical, Communication and Computer Engineering (ICECCE)*, 2024 in press 2024, pp. 1–6

6. Z. Zhang, P. Lin, M. M. Islam, L. Zhou, and G. Yao, "Developing control strategies to enhance power quality in grid-connected natural gas pressure differential generation

systems: Advancing clean energy practices," in *IEEE International Humanitarian Technologies Conference*, 2024 in press 2024, pp. 1–7

7. J. Kunqi, S. Zhang, M. M. Islam, T. Yu, Y. Wenda, and Z. Yating, "Optimization of multi-microgrid energy trading in distribution networks using a master-slave game approach," in *IEEE International Humanitarian Technologies Conference*, 2024 in press 2024, pp. 1–5

8. M. M. Islam, T. Yu, M. La Scala, J. Wang, and L. Chengdong, "Optimizing cooperative alliance transactive energy framework for pv-based multi-microgrids using scheduling and cooperative game theory," in *2024 4th International Conference on Electrical Engineering and Informatics (ICon EEI)*, 2024, pp. 96–101

9. M. N. Rajabi, R. Cometa, C. Iurlaro, M. M. Islam, S. Bruno, and M. La Scala, "Stand-alone dc microgrids for rural areas: A decentralized energy management and voltage regulation approach," in *IEEE International Humanitarian Technologies Conference*, 2024 in press 2024, pp. 1–7

10. P. Lin, W. Song, Z. Zhang, L. Zhou, G. Yao, and M. M. Islam, "Sensorless control of high-speed dual three-phase permanent magnet synchronous motor," in *The Proceedings of the 19th Annual Conference of China Electrotechnical Society*. Singapore: Springer Nature Singapore, 2025, pp. 1–10

11. Z. He, S. Li, M. M. Islam, and G. Chen, "Study on the effect of plate rib-channel ratio on the performance of pemfc: a cleaner and sustainable energy practice," in *Springer*, 2024 in press 2024, pp. 1–8

Journal

1. T. Yu, M. M. Islam, L. Zhou, Z. Wang, M. La Scala, X. Guan, and G. Yao, "A novel hierarchical control framework for enhancing stability, security and reliable power dispatch tracking in islanded microgrids," *IEEE Transactions on Smart Grid*, pp. 1–10, 2024 in press 2024

2. M. M. Islam, T. Yu, M. La Scala, and J. Wang, "Robust nonlinear control design with optimal coordination methodology for bidirectional bev chargers in v2g/g2v applications," *Journal of Energy Storage*, pp. 1–18, 2024 in press 2024

3. T. Yu, M. Muzammal Islam, J. Wang, Z. Wang, M. La Scala, B. Yang, and G. Yao, "A novel augmented bolza problem and its applications in power systems to support grid services," *IEEE Transactions on Smart Grid*, pp. 1–9, 2024, (under-review)

4. M. Muzammal Islam, T. Yu, G. Giannoccaro, Y. Mi, M. la Scala, M. Rajabi Nasab, and J. Wang, "Improving reliability and stability of the power systems: A comprehensive review on the role of energy storage systems to enhance flexibility," *IEEE Access*, vol. 12, pp. 152 738–152 765, 2024

5. W. Ziqiang, Y. Haosen, X. Linyun, H. Wentao, M. Muzammal Islam, M. La Scala, and Y. Chen, "Voltage-frequency constrained control for dc-link voltage synchronization of renewable energy," *IEEE Power Engineering Letters*, vol. 12, pp. 1–3, 2024, (under-review)

Introduction

Background and Research Motivation

A Microgrid (MG) is commonly described as "an electricity distribution network that includes loads and distributed energy resources, such as the generators, storage systems or controllable loads that can be managed in a coordinated and controlled manner, whether connected to the main power grid or operating in isolated mode, as defined by the *Conseil International des Grandes Réseaux Électriques (CIGRÉ) Working Group C6.22*. This thesis emphasizes control and optimization methodologies developed to provide energy and ancillary services through MG, ensuring stable and reliable power operations.

In isolated microgrids located in remote regions, the absence of large rotating generators and the integration of renewable energy sources (RESs), which are primarily connected through power converters like inverters, pose significant challenges. These inverters can decouple the inertia of the RESs from the distribution network, rendering the inertial contribution of energy resources, such as wind generators, ineffective. Therefore to maintain smooth operation during sudden load fluctuations, it is crucial to implement grid-forming control actions or faster resources. These measures are necessary to quickly adjust power exchange references and provide ancillary services support such as voltage and frequency regulation and enabling the inertia in the early stage of transient events.

Moreover, in grid-connected microgrids, the involvement of power converter control actions can also lead to voltage and frequency regulation issues, due to their switching operations which can also cause power quality problems. Therefore, grid-forming and grid-following control actions are crucial for maintaining the stability and reliability of these power networks. However, the unique characteristics of isolated MGs provide an ideal environment for testing new control and optimization methodologies while considering the energy resources. It is important to note that in isolated microgrids, the aforementioned issues are typically not a concern for extended periods, as disconnection from them is

usually temporary. Such disconnection is often short-lived, intended for exploring control and optimization methodologies following an unintended trip due to transient events on the main microgrid.

The variable nature of RESs coupled with fluctuating load demands and the power converter control actions, can cause passive power fluctuations that may compromise the stability and reliability of the MG. Therefore, it is crucial to enable energy and ancillary services through MGs. Furthermore, a critical aspect is increasing the hosting capacity on the MGs side, particularly for islanded microgrids, while integrating the growing share of RESs and reducing dependence on fossil fuels. Fuel costs have a disproportionately higher impact on islands compared to mainland systems, significantly affecting overall energy expenses for the entire state. This poses additional challenges in achieving the decarbonization targets set by governments and non-governmental organizations. Developing control and optimization methodologies through MGs provides quick, cost-effective, and extensively researched solutions that can be implemented immediately. Thus, it is essential to design robust control and optimization strategies to enable energy and ancillary services through MGs, enhancing the reliability and stability of power system networks

Research contributions

The thesis explores various robust control and optimization methodologies that facilitate the provision of energy and ancillary services through MGs. These methodologies not only enhance the reliability and stability of power networks but also improve the flexibility of power distribution networks and end-user applications, including residential buildings. The main contributions are summarized below:

- Evaluating the role of various types of energy storage systems in demand response management and in enabling energy and ancillary services through MGs and exploring the impact of ESSs on the flexibility of the power networks;
- Assessing the impact of increasing renewable energy penetration on small islands in solving optimal dispatch problems, and how this affects the choice of the reserve assessment methods to be adopted;
- Assessing the energy consumption issues of clusters within the distribution network when integrating two or more MGs, while providing a transactive energy framework to encourage the installation of renewable-based MGs.

- The development and analysis of various optimal control methodologies, including economic scheduling, load management, and energy service provision, aim to support transactive energy frameworks within MMGs systems. These methodologies account for real-time power exchanges among participants and the power distribution network, ensuring that load demands are met and benefits are equitably distributed among all participants;

- Designing robust optimization methodologies using efficient algorithms, such as column-and-constraint generation, facilitates economic dispatch and optimal energy management of high voltage power networks while addressing the uncertainties associated with RESs;

- Developing a robust controller for frequency regulation in islanded MGs involves incorporating a disturbance observer to estimate the impact of random disturbances, such as solar irradiance and wind speed, while also accounting for load variations;

- Assessing the traditional three-layer hierarchical control framework of microgrids and designing a novel hierarchical control framework for islanded microgrids focuses on improving frequency regulation across control layers, as well as enhancing security, stability, and reliable power dispatch tracking;

- Developing novel optimal control problems, such as modified Bolza optimal control, using optimal control theory and variational calculus, and applying them to MGs while considering power converter control actions for efficient frequency regulation and load demand fulfillment with hybrid energy storage systems;

- Designing a low-cost controller to introduce synthetic inertia into the system aims to mitigate the effects of the rate of change of frequency, implement the designed control laws, and enhance overall system stability. Additionally, the effectiveness of the proposed methodologies will be evaluated through power hardware-in-the-loop simulation tests;

- Evaluating the voltage regulation response in standalone DC-MGs and enhancing their efficiency by integrating battery energy storage and utilizing electric springs to improve overall system flexibility.

Outline of the thesis

The introductory section provides the basic motivation and research background of the topic, offering context for the study and outlining the main contributions of this thesis. The thesis is organized into the following chapters:

Chapter 1 - Overview of Energy and Ancillary Services in MGs: This chapter provides an overview of energy and ancillary services in MGs, offering the reader a solid foundation about these services. It includes a comprehensive discussion of these services and their roles in enhancing MGs stability and reliability. Additionally, a detailed discussion on the role of ESSs in microgrids is provided, focusing on how ESSs enable energy and ancillary services within these systems.

Chapter 2 - Demand Response Management: This chapter explores the impact of demand response management in MGs, addressing electricity consumption and utilization issues within power distribution networks. It focuses on how demand response enhances flexibility and improves the reliability of MMGss by presenting novel research on optimal coordination among multi-microgrids and with the DSO.

Chapter 3 - Frequency Regulation and Inertia Control This chapter explores the challenges associated with frequency regulation and inertia control, offering solutions through novel robust optimization and control methodologies. These methodologies are essential for improving frequency regulation and inertia control, which are critical ancillary services that enhance the reliability and stability of microgrids, contributing to resilient power operations. Additionally, the chapter discusses various real-time power hardware-in-the-loop tests related to frequency regulation and synthetic inertia enablement.

Chapter 4 - Voltage Regulation: This chapter explores the impact of voltage regulation in DC-MGs, addressing electricity consumption and utilization issues within power distribution networks. It focuses on how voltage regulation enhances flexibility and improves the reliability of power system networks by using flexible sources, such as electric springs and BESS.

Chapter 1

Overview of Energy and Ancillary Services in Microgrids

Microgrid (MG), which are a promising solution for meeting energy demands, are localized networks of power generation, storage, and consumption systems. They can operate either in isolated mode or in coordination with the main grid, offering flexible and resilient power operations that support the main grid or function autonomously when needed.

The depletion of fossil fuels, rising demands for clean energy, and increased awareness of greenhouse gases (GHGs) are accelerating the installation and integration of renewable energy sources, such as solar and wind. Consequently, the growing demand for green energy is driving the deployment of more distributed generations (DG)s and renewable energy sources (RESs), not only improving energy service continuity but also increasing end-users participation in the electricity market to generate more revenue. However, the increasing integration of RESs introduces several challenges, such as maintaining the stability and reliability of the power network due to the high intermittency and variability of these sources [17]. According to the 2024 annual renewable market forecast report by the International Energy Agency (IEA), global renewable energy deployment is expected to grow by approximately 2.7 times by 2030, surpassing current national ambitions by about 25%, though still falling short of the goal of tripling capacity. The IEA Report 2024 also forecasts, that the European Union (EU) and the United States will double the pace of renewable capacity growth between 2024 and 2030, while India is expected to see the fastest rate of growth among large economies. It is worth mentioning that tripling of global renewable capacity is within reach, however, further policy improvements are needed in the future [18].

Over the past few years, the EU has made significant progress in advancing the deployment and adoption of renewable energy, setting both short- and long-term goals while introducing supportive policies and regulatory frameworks. Building on insights from directives 2001/77/EC and 2009/28/EC of the European Parliament and Council, Directive EU 2018/2001 addressed these challenges by setting a 32% renewable energy target for 2030, with provisions for increasing this target and revising permitting processes for renewable energy developers by 2023 [19, 20]. To further accelerate renewable deployment, the Council, following a Commission proposal, has introduced measures to support renewable projects and facilitate power purchase agreements. These amendments represent a significant increase in the EU's renewable energy share. At the heart of this transformative ecosystem are microgrids, which can help decentralize renewable energy generation and integrate RESs, while ensuring resilient and sustainable power operations to enhance the system's overall flexibility [21].

Climate change is a significant concern. According to an EU-wide survey published in September 2017, over 92% of European citizens view climate change as a serious issue. In November 2018, the European Commission unveiled a long-term strategic vision to minimize GHGs emissions, highlighting the following key vision points [22];

- To fully harness the benefits of energy efficiency and support the complete decarbonization of Europe's energy supply, the focus is on achieving zero-emission buildings.
- To maximize the expansion of renewable energy and increase electricity usage,
- To promote the clean, safe, and sustainable mobility,
- A competitive EU industry and the circular economy play a crucial role in reducing GHGs emissions,
- To establish a suitable smart network infrastructure and interconnections,
- To fully leverage the advantages of the bioeconomy and create vital bio sinks,
- To address the remaining CO_2 emissions through carbon capture and storage.

As part of its long-term strategy, the European Commission has established goals for 2050 aimed at achieving net-zero GHGs emissions. This key objective, which is central to the European Green Deal, is legally enforceable under the European Climate Law.

1.1 Fundamentals of microgrid

A microgrid is a localized energy system that primarily distributes and manages electricity for distributing and managing electricity within specific areas, such as communities, commercial complexes, and industrial sites. Although numerous definitions of MGs exist in the literature, however, they all converge on the same concept as mentioned in the following studies [23–25]. MGs are generally powered by distributed energy resources (DERs), such as solar panels, generators, wind turbines, energy storage systems, and various kinds of loads. Furthermore, power generation and demand-side management, which integrates RESs and traditional power generation, along with the demand-side management system, is a crucial aspect of the MG. This combination allows for the support of diverse energy sources while enhancing the system's stability and reliability. MGs have clearly defined boundaries that separate them from the main power grid. These boundaries generally appear on a smaller scale, allowing MGs to operate at different voltage levels, such as low voltage (LV) and medium voltage (MV).

As aforementioned, MG rely on various RESs, energy storage systems, and various distribution system configurations. The benefits associated with RESs can be outlined as follows:

- Incorporating clean energy sources like solar and wind into MGs helps decrease carbon footprints and mitigate the effects of climate change.
- MGs powered by RESs can operate independently in islanded mode, increasing resilience during power outages or extreme weather conditions.
- MGs utilizing RESs can easily be scaled or reconfigured to adapt to changes in energy demand and resource availability to enhance the flexibility and scalability of the system.

In the case of energy storage systems, MGs receive numerous benefits, including:

- ESSs help maintain stable power operations by balancing demand and supply effectively.
- ESSs can deliver ancillary services, including voltage and frequency regulation, black start capabilities, and enhancements to the overall performance of the system.
- MGs utilizing ESSs benefit from cost savings by minimizing expensive peak-time energy purchases and enhancing the efficiency of RESs.

Moreover, the benefits linked with the end-user applications can be written down as follows:

- End-user applications allow consumers to produce their own energy by utilizing DERs.
- Enhancing the reliability of the end-user systems.
- Lowering the carbon emissions.
- MGs offer end-user backup power during emergencies or natural disasters.
- MGs can support electric vehicles (EV) charging stations, fostering sustainable energy and transportation development while aiding in the transition to electric mobility.

Despite the numerous advantages of MGs, they also face several limitations primarily associated with barriers such as regulatory challenges, technical complexity, limited scalability, high operational and maintenance costs, and economic viability.

1.1.1 Operation of microgrids

MGs can operate in two primary modes; grid-connected and islanded modes. Each mode provides distinct benefits based on the specific energy needs and how well they support the utility grid [26]. A brief overview of both operational modes is provided below:

1.1.1.1 Islanded mode

In islanded mode, the microgrid operates independently from the main grid. To achieve this, the MGs must have its own generation capacity, such as diesel generators, which enable disconnection from the main grid while ensuring a continuous power supply [27].

- This mode of operation is particularly useful in remote locations or during power outages, as it improves resilience.
- The main challenges during islanded operation involve balancing power demand and supply, as well as frequency and voltage regulation.
- Additionally, achieving black start capability is crucial for operating independently without support from the main grid.

1.1.1.2 Grid-connected mode

In this mode, the microgrid is connected to the main utility grid, allowing for energy exchange between the two systems [28]. The following points should be considered:

- During the grid-connected mode of operation, the MG can either draw power from the main grid when local generation is insufficient or feed the power back into the main grid, when there is an excess amount of power available.
- In grid-connected mode the MG can take advantage of lower grid electricity prices during off-peak hours and sell the power back during the grid's higher energy demands or peak hours.
- Additional operations in grid-connected mode include demand response and peak shaving, which help reduce power consumption and better align load demand with real-time pricing.

MGs can also be implemented based on their configuration levels, such as different voltage levels, whether they operate on Direct Current (DC), alternating current (AC), or as hybrid systems depending on ownership. For instance, large-scale industrial plants, constrained by geographical limitations, often have limited interaction with distribution networks. In this context, significant advancements have been made in the design and implementation of various types of MGs, such as those for residential buildings, educational institutions, research campuses, and industrial-based nano grids. A prominent example of these configurations and typologies is in the MGs for Microgrids for Efficient, Reliable, and Green Energy (MERGE) projects as illustrated in [29]. The MG functions work across multiple control levels and various time frames, targeting diverse components and assets within the MG. They encompass everything from device-level operations typically integrated into DERs, to higher-level supervisory and grid-interactive functions within the MG.

1.2 Control framework of microgrids

The control framework of a MG typically consists of multiple hierarchical control layers that manage the interaction between various types of DERs, ESSs, and the grid. A well-designed control framework is essential for ensuring stability, optimizing power quality, improving economic performance, and enhancing the resilience of the MGs in both

islanded and grid-connected modes [30, 31]. Some of the main functions of the control system include:

- The control architecture guarantees smooth operation and stability of the MG, whether it is connected to the main grid or operating independently in islanded mode.
- During power system disturbances like blackouts, the control system enables an automatic switch from grid-connected to islanded mode to ensure a continuous power supply.
- Ensure the capability to safely re-synchronize and reconnect the grid after operating in an islanded mode without compromising the overall system stability.
- The control system optimizes the balance between real and reactive power generation and consumption within the MG.
- The MGs control system also supports the wider distribution grid by providing ancillary services, such as frequency regulation, voltage support and even participating in energy markets, helping to improve grid reliability and efficiency [32].

1.2.1 Hierarchical control framework

The control framework is divided into three hierarchical layers: primary, secondary, and tertiary control layers [33, 34]. The functionalities of each of these control layers are described in the following sections:

1.2.1.1 Primary control

The primary control is tasked with quickly stabilizing voltage and frequency at the local level. Its main functions include maintaining the local voltage and frequency stability, providing a fast dynamic, and enabling operation without communication between the units. It typically includes the following:

- **Droop control**: The droop control shows the behavior of the large synchronous generators by regulating the power output of DERs in response to voltage and frequency fluctuations. This enables efficient load sharing among multiple generators without the need for communication.

- **Inverter control**: Inverter-based DERs, like PV and BESS systems, must enhance the system's response while ensuring a smoother absorption of power supply.

1.2.1.2 Secondary control

The secondary control layer focuses on returning voltage and frequency to their nominal levels following the primary control actions. It operates on a slower timescale and may require efficient communication between the various MG components. The objectives of the MGs secondary control are outlined as follows:

- Once the droop control stabilizes the system, the secondary control adjusts any deviations to return the system to its nominal values.
- If any discrepancy arises among the generators regarding load sharing, then the secondary control adjusts the sent points accordingly.
- Secondary control assists in improving the power-sharing accuracy.

1.2.1.3 Tertiary control

Tertiary control is tasked with optimizing the economic operation of the MG, particularly in grid-connected mode. This control layer also facilitates the management of power flow between the MG and the main grid while optimizing the response of energy resources.

- It guarantees that power generation and consumption occur at the lowest cost by taking into account fuel, maintenance, and operational expenses.
- It assists in managing the power flow between the main grid and MG through an Energy management system (EMS), ensuring compliance with contractual agreements and market signals.
- It assists in implementing demand-side management and load forecasting. Both centralized and decentralized control approaches are also present at this level of control.

Fig.1.1 illustrates the basic hierarchical control framework of the MG, based on its three control layers and corresponding timescales. From the figure, it is evident that device-level functions operate on shorter timescales, typically from milliseconds to several seconds, while management spans several longer timescales, from seconds to several days.

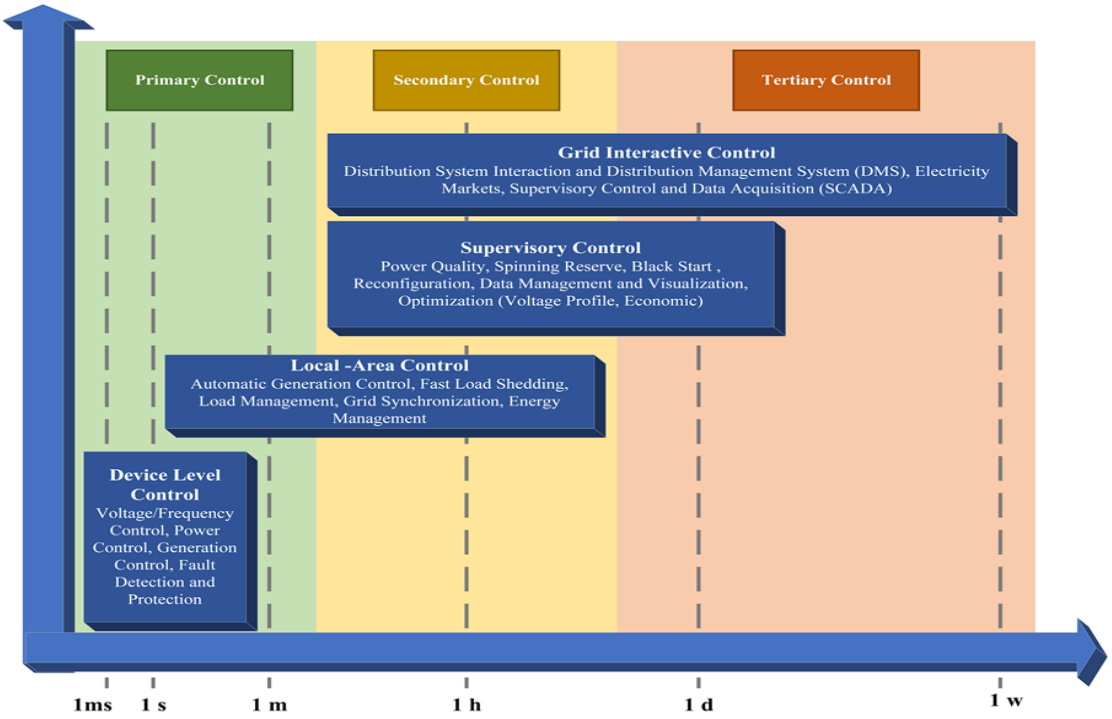

Figure 1.1: Hierarchical control framework with three control layers representing different timescales

Functions managing the transition between several connections and disconnections, as well as those responsible for dispatching DERs assets, operate on distinct timescales. However, in the case of unplanned disconnections, the transition function needs to act promptly with minimal delay, operating on a shorter timescale. In contrast, the dispatch function occurs regularly at intervals, generally within longer timescales of minutes (15 minutes or less) [35]. However, the technical requirements may change based on the location.

1.2.2 IEEE standards regarding operation and control of microgrids

Regarding the operation and control of MGs, IEEE has established specific standards. For example, in [36], the three-layer hierarchical control is analyzed in accordance with the IEEE 2030.7-2017 standard, considering dispatching and transition control from the lowest level (level 1) of field device automation to the highest level of monitoring and control, (level 3). This standard has become a key reference for designing control architecture in MGs. However, this standard is complemented by other standards, such as the IEEE standard 2030.8-2018, as mentioned in [37], which addresses the evaluation of the performance of the MG controller.

Similarly, in [38], IEEE standard 1547-2018 outlines the regulations for the intercon-

nection and interoperability of DERs with the associated electric power system interfaces. Furthermore, following the guidelines of IEEE standard 2030.7, IEC 62898-2 explores the key principles of MG control and operation. IEC 62898-2 places greater emphasis on operational modes, mode transitions, EMS, and MG operations, while also considering communication and monitoring procedures as referenced in [39]. In contrast, IEC 62898-3 focuses on both general and specific technical requirements for MG monitoring, dynamic control, and fault protection, as described in [40]. According to the guidelines, outlined in this standard, non-isolated MGs can operate autonomously for a limited time, necessitating the eventual reconnection to the main power grid. In contrast, isolated MGs lack the capability to reconnect to a larger external grid, as mentioned by IEC 62898-2. However, IEEE 2030.7 simply categorizes MG states as either grid-connected or islanded. Furthermore, islanded MGs face fewer restrictions regarding the grid connection rules; however, their control functions must possess greater capabilities than those of the grid-connected MGs. These capabilities include the ability to perform a black start, continuous monitoring, energy management, load shedding for balance, and a significantly higher energy storage capacity.

1.3 Provision of Energy and Ancillary Services

MGs have the capability to provide a wide range of energy and ancillary services that support both local power needs and the main grid. This section presents a detailed analysis of various types of energy and ancillary services enabled by MGs.

1.3.1 Renewable energy integration

This section addresses the role of renewable energy integration and its implication for control and optimization within MGs. The increase in pollution level, resulting in higher GHGs emissions and the subsequent impact of global warming, along with the growing demand for green energy, is shifting the focus towards the installation of more RESs [41]. However, the intermittent nature of the RESs can hinder the stable and reliable operations of MGs. Therefore, energy cooperation among multiple MGs, supported by optimization methodologies, is crucial for enabling energy exchange and sharing, providing a promising solution [42]. Furthermore, integrating RESs into MGs may introduce challenges in providing ancillary services. Fig. 1.2 schematically illustrates the integration of renewable

energy within the architecture of isolated or weekly connected MGs. Some of the key challenges associated with the integration of RESs [43, 44], are as follows:

- Intermittency and variability of RESs, such as solar and wind, may lead to fluctuations in power generation, making it more challenging to consistently provide ancillary services like frequency and voltage regulation. Additionally, unlike conventional power plants, RESs lack mechanical inertia, which is crucial for maintaining frequency stability and ensuring smooth grid operations.
- To manage the variability of RESs, large-scale ESSs are often necessary to ensure that MGs can provide ancillary services like load balancing, during low-generation periods. However, ESSs technologies are costly and can cause efficiency losses, making the overall system economically less viable. Thus, robust optimization and control methodologies are needed to address the variability of RESs.
- Maintaining high power quality is a significant challenge when integrating RESs, as issues like harmonic distortion and voltage sags can affect the MGs ability to deliver high-quality services.
- Addressing the challenge of matching RESs generation variability with load demand is crucial for delivering ancillary services like load balancing and voltage support. Additionally, integrating flexible resources, such as batteries or demand-side management, is essential for supporting RESs-based ancillary services.
- The existing market framework may not sufficiently compensate MGs for providing ancillary services from RESs, leading to economic challenges for their integration. Additionally, regulations governing grid interconnection and ancillary services provision may not be fully adapted to the increasing use of RESs within MGs.

Despite challenges as outlined in the aforementioned section, integrating RESs into MGs offers numerous advantages [45, 46], including the following:

- Improved energy security arises from the ability of RESs to enable MGs to generate more power locally, thereby reducing dependence on centralized power plants, particularly in remote or isolated areas.
- The integration of RESs, such as solar and wind energy, offers environmental benefits, including a reduction in GHGs emissions, compared to fossil fuel-based energy sources, contributing to climate change mitigation.

- Moreover, by utilizing locally available renewable resources, communities can attain greater energy independence and minimize their reliance on fossil fuel markets.
- In the long run, integrating RESs can lower energy costs by reducing operational expenses and decreasing the prices of renewable technologies. Additionally, the development and maintenance of RESs infrastructure generate job opportunities within the local economy.
- Integrating RESs into MGs facilitates the development of charging infrastructure for EV, encouraging cleaner transportation options and further decreasing emissions.

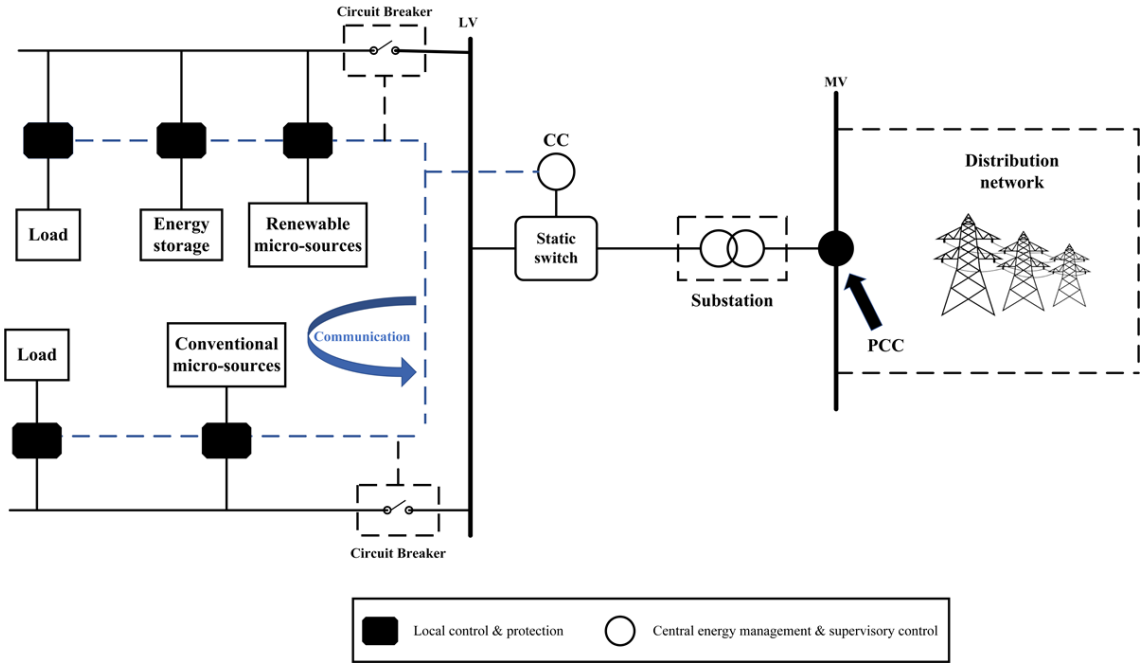

Figure 1.2: Integration of renewable energy into microgrids

Based on the above discussion, it can be analyzed that providing energy and ancillary services through MGs is crucial for maintaining balanced energy markets. The transition toward 100% is not as unrealistic as it may seem. As noted in [47], eight European countries are expected to achieve 100% renewable energy penetration on an hourly basis. MGs are seen as a fundamental solution for integrating RESs and ESSs to more efficiently meet various load demands. However, the integration of RESs into MGs may result in instability issues, such as voltage and frequency fluctuations, as well as demand variations [48]. Therefore, the provision of ancillary services is crucial to meeting load demands. Additionally, the European Network of Transmission System Operators for Electricity

(ENTSO-E), has analyzed ancillary services and evaluated the situation using data from transmission system operators.

1.3.2 Peak shaving and load management

Peak shaving and load management are important aspects of enhancing the flexibility of power networks. According to ENTSO-E guidelines, energy storage may improve supply security by smoothing load patterns. This is achieved by increasing the off-peak load, storing energy during periods of low demand, and reducing peak load by discharging during periods of high demand [49]. Furthermore, according to [50], a report on the design of the European electricity market highlights the proposed changes that emphasize the promotion of demand-side flexibility, which includes peak shaving and flexibility support schemes. The peak shaving product is a new service that system operators can procure from consumers. This service can be produced a few days prior to delivery and can be activated before, during, or after the day-ahead market. When activated, the consumer must reduce their consumption below a predetermined baseline, for which they receive financial compensation.

1.3.3 Energy arbitrage

Energy arbitrage is a crucial energy service that involves purchasing and storing electricity when prices are low. This practice optimizes energy costs for consumers and supports grid stability by balancing supply and demand. As a result, consumers or businesses participating in energy arbitrage can receive financial compensation for the energy they sell back to the grid or for their reduced consumption during peak hours [51].

1.3.4 Demand response and load flexibility

Demand response and load flexibility are energy services that adjust the electricity consumption patterns in response to external signals, such as price fluctuations or grid conditions. Additionally, within the context of MGs, these services are essential for optimizing energy use while improving grid reliability and flexibility, particularly in relation to the integration of more RESs [52]. Fig. 1.3 illustrates the various types of services that DERs can support within the scope of the analysis framework. From this figure, it can be analyzed that all quadrants of the analysis framework gradually opened to DR including the day thread

market in 2014, positioning France as the first European country to fully open all national markets at the distribution grid level.

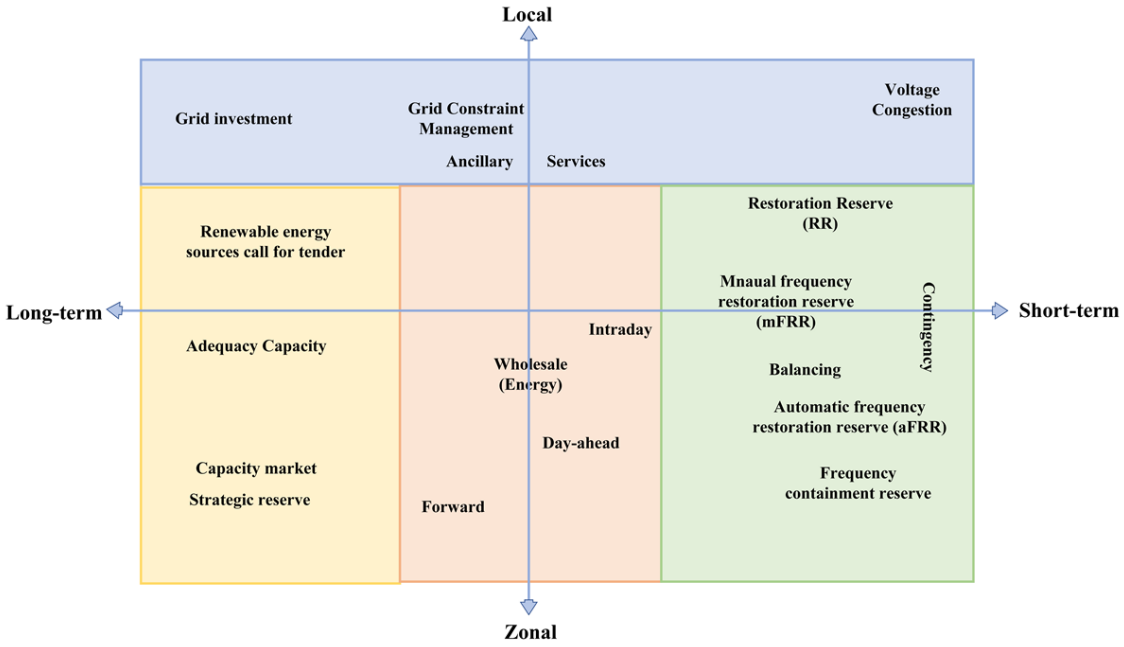

Figure 1.3: Types of services that DERs can support within the scope of the analysis framework

1.3.5 Energy security for remote/islanded microgrids

Energy security of the MGs, specifically the islanded MGs refers to the ability of these systems to provide reliable and continuous power supply independently from the central grid. This concept is particularly significant for MGs that serve isolated or remote areas, where connecting to the larger grid may be impractical or prohibitively expensive. As a result, energy security for these remote/islanded MGs strengthens overall system resilience and flexibility while promoting the installation of more RESs [53].

1.3.6 Classification of ancillary services

The system operator must uphold the required quality and safety standards to ensure the reliability and resilience of the power networks while fostering preventive measures for contingency control and managing other responsibilities. Ancillary services are typically provided through power trading and dispatch processes. Fig. 1.4 illustrates the classifications of numerous ancillary services. Various types of ancillary services are assessed

based on the classification and integration of various operations and resources, including frequency control, network control, and system restart services.

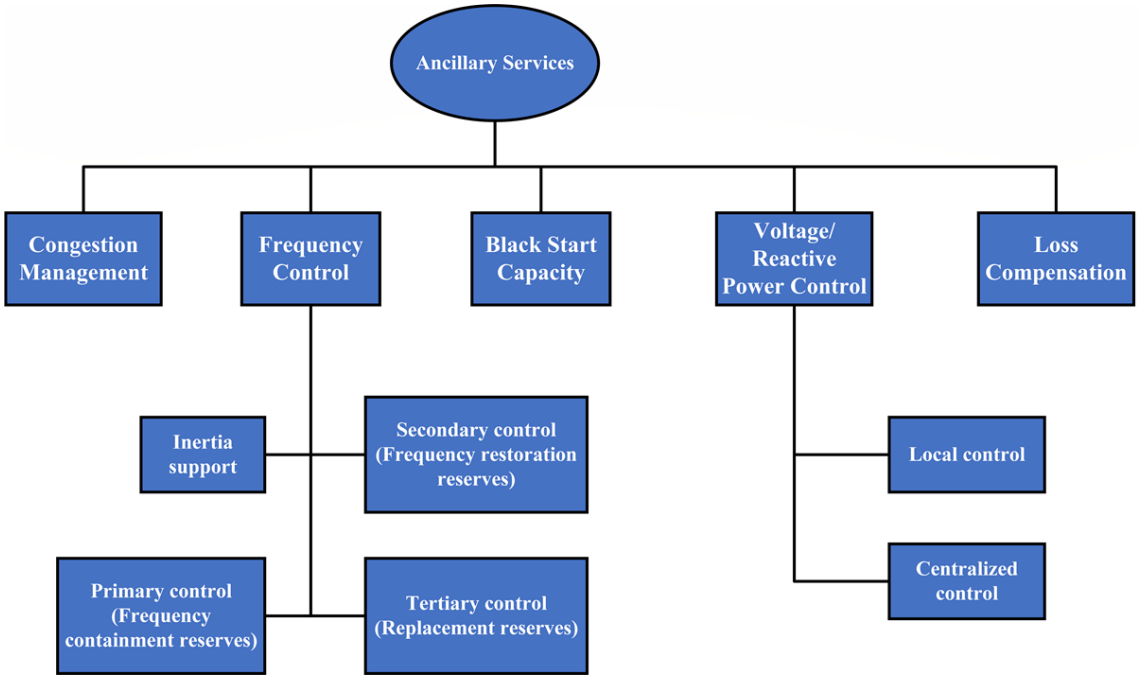

Figure 1.4: Classification of ancillary services

1.3.6.1 Frequency control services

Frequency indicates the balance between the generated and the consumed active power, both of which must be equal for an AC system to function properly. Hence, frequency serves as a key indicator for regulating active power output to maintain system balance. Additionally, system security depends on maintaining a stable frequency, and frequency variations are acceptable as long as they remain within a defined range to ensure the safe operation of connected devices. Since the power consumption varies, it is crucial to adjust the active power output accordingly [54]. Therefore, technical factors are fundamental to frequency control services, where deployment time plays a crucial role. The three control levels in the hierarchical structure differ from each other in terms of their operational approach. The primary control layer is activated within seconds by the relevant parties or Transmission System Operator (TSO), while secondary control takes over within minutes, enforced by the responsible entities. Tertiary control then partly supports and eventually replaces secondary control through generation rescheduling [55]. Additionally, some case studies have been conducted in [56], on drafting ancillary services and network code

definitions, related to frequency estimation, as well as the provision of the rate of change of frequency (ROCOF) and fast frequency control.

According to ENTSO-E, industrial demand response plays a crucial role in frequency balancing and voltage control within the power industry. With substantial and rapid response capabilities, industrial loads already contribute to frequency balancing reserves and can adjust both active and reactive power consumption to effectively support voltage control services. To offer a sufficiently faster response to help the frequency imbalances, the industry must enable its consumption to be changed relatively fast. The **fast frequency regulation (FFR)** requires that 100% of the power offered can be activated within a period of 1 second. So, according to the technical requirements the FFR requires that 100% of the power offered can be activated within a period of 1 second. Moreover, to participate in the Frequency Containment Reserve (FCR) market, 50% of the offered power must be activated within 15 seconds and 100% within 30 seconds. This technical requirement is applicable to the Nordic power system [57].

1.3.6.2 Emulation of virtual inertia

Virtual inertia emulation can be considered an ancillary service, using power electronics and control algorithms to replicate the natural inertia provided by conventional rotating generators. In traditional power systems, inertia resists changes in rotational speed and helps stabilize the grid frequency by automatically balancing short-term imbalances between supply and demand. In MGs, virtual inertia serves as an important ancillary service for several reasons: including maintaining frequency stability, enhancing reliability, supporting the system during islanded operations, and facilitating the integration of RESs [58]. An example of this is the transmission network of the Italian national power grid (TERNA), which includes a fast reserve project approved by the Autorita di Regolazione per Energia Reti e Ambiente (ARERA), as mentioned in [59]. This project aims to support system inertia and provide a rapid response to frequency variations caused by continuous set point changes.

1.3.6.3 Voltage control services

Voltage control is another key ancillary service that ensures optimal power quality by regulating the injection and absorption of reactive power within the power network. To maintain the system voltage at various nodes, precise limits, and adequate reactive power limits are managed. Primary voltage control is often handled by local automatic control,

which stabilizes the voltage at generation buses at node points through automatic voltage regulation (AVR). Moreover, the secondary voltage control integrates an automatic system to coordinate the actions of local controllers more effectively. Meanwhile, tertiary control focuses on optimizing the overall reactive power flow throughout the system [60].

1.3.6.4 Reactive power support

Various system operators for different networks, including distribution and transmission networks, may require different ranges of reactive power due to factors such as network topologies, the location of connection points at the interfaces between transmission and distribution systems, and embedded generation and load demands [61]. Reactive power support is crucial for maintaining voltage levels within safe limits. In power distribution networks, reactors, power banks, and power electronics help manage stable voltage and efficient power transfer by minimizing losses and reducing voltage instability [62].

1.3.6.5 Congestion management

Congestion management is a vital ancillary service that aims to prevent distribution and transmission lines from becoming overloaded by redirecting or adjusting power flows within the grid. When specific lines or segments reach or exceed their capacity limits, it can result in inefficiencies, higher costs, and reliability risks. Therefore, congestion management addresses these challenges, by reconfiguring the network topology, optimizing generation dispatch, or implementing demand-side management strategies [63]. Many recent studies in the literature focus on congestion management. One notable example is the optimal system mix of flexibility solutions for the European electricity (OSMOSE) project as mentioned in [64], which aims to improve congestion management in high-voltage grids and to promote renewable energy production by coordinating Dynamic thermal rating (DTR) and demand-response resources.

1.3.6.6 Black start capability

Black start capability is another essential ancillary service, allowing certain power stations to start independently from a shutdown state without relying on an external power supply. This capability enables these stations to connect to and support sections of the power system, ensuring proper coordination for system restoration regardless of production unit costs [65].

1.3.6.7 Load following

Load following is the capability to adjust generation to meet varying load demands throughout the day. This ancillary service accommodates predictable changes in demand patterns, ensuring sufficient generation to handle real-time load fluctuations [66].

1.3.7 TSO-DSO coordination and ancillary services provision

This section presents the concept of optimized interaction between TSOs and Distribution system operator (DSO) to manage the information exchange for monitoring and operating of ancillary services, including frequency control, frequency restoration, congestion management, and voltage regulation. Recently, several EU projects have focused on TSO-DSO coordination and the provision of Ancillary services (AS). A notable example is the SmartNet project, as mentioned in [67]. The project report suggests that local ancillary service needs within distribution systems should be compatible with system-wide requirements for balancing and congestion management. Additionally, resources within distribution systems are expected to contribute to ancillary services both locally and at the system-wide level within competitive ancillary services markets. There are several TSO-DSO coordination schemes designed to facilitate the operation of various transmission and distribution systems, as well as different market operations. The coordination schemes are mentioned as follows:

- **Centralized AS market model:** This framework allows the TSO to manage and coordinate the ancillary services across the entire power system. In this model, the TSO centralizes the procurement and dispatch of ancillary services, such as frequency control, voltage support, and reserve power to ensure grid stability and reliability. Additionally, this model provides an efficient solution with the TSO as the primary service buyer, creating a unified market that reduces operational costs, supports standardized processes, and aligns effectively with the existing regulatory framework.

- **Local AS market model:** In the context of the distribution system, the DSO prioritizes the use of local flexibility while actively supporting the procurement of ancillary services. Additionally, local markets may lower entry barriers for smaller-scale DERs.

- **Common TSO-DSO AS market model:** This collaborative framework allows both the TSO and DSO to jointly manage the procurement and coordination of ancillary services. Unlike the centralized model, where the TSO alone oversees Ancillary services (AS) markets, the common model enables shared responsibilities and joint participation in market operations. Additionally, this model minimizes the overall costs of ancillary services for the TSO and local services for the DSO. By working closely together, the TSO and DSO can optimize the use of available flexible resources.

- **Shared balancing responsibility model:** In this model, both TSO and DSO share responsibility for maintaining the balance between supply and demand within their respective network areas. Consequently, the TSO will need to procure a smaller amount of AS, while the local market can reduce entry barriers for small-scale DERs by taking into account the operational needs of both TSO and DSO.

- **Market model:** A market model in the context of power systems is a structured framework that outlines how transactions, pricing, and interactions take place within energy markets, particularly for services such as balancing, congestion management, and ancillary services. This model facilitates high liquidity and competitive pricing, driven by the presence of numerous buyers and sellers.

- **Integrated flexibility:** This model involves the coordinated use of various flexible resources, including DERs, energy storage, demand response, and flexible generation to improve the reliability and efficiency of the electricity grid. Additionally, it provides more opportunities for balance-responsible parties to better manage imbalances within their portfolios.

1.3.7.1 The Organization of ancillary services within various coordination schemes

As previously stated, various coordination schemes have been analyzed through several projects, as noted in [68]. However, the three ancillary services namely, frequency restoration/balancing, congestion management, and voltage control are more focused while considering their role in enhancing the flexibility and reliability of the transmission grid.

Regarding frequency restoration and congestion management, all coordination schemes adhere to pre-qualification requests that go through the market. However, the process may vary if the local market may exist in parallel to the central market. To better explain the

process for the centralized market organization. Fig. 1.5 represents the pre-qualification coordination scheme with a centralized market design.

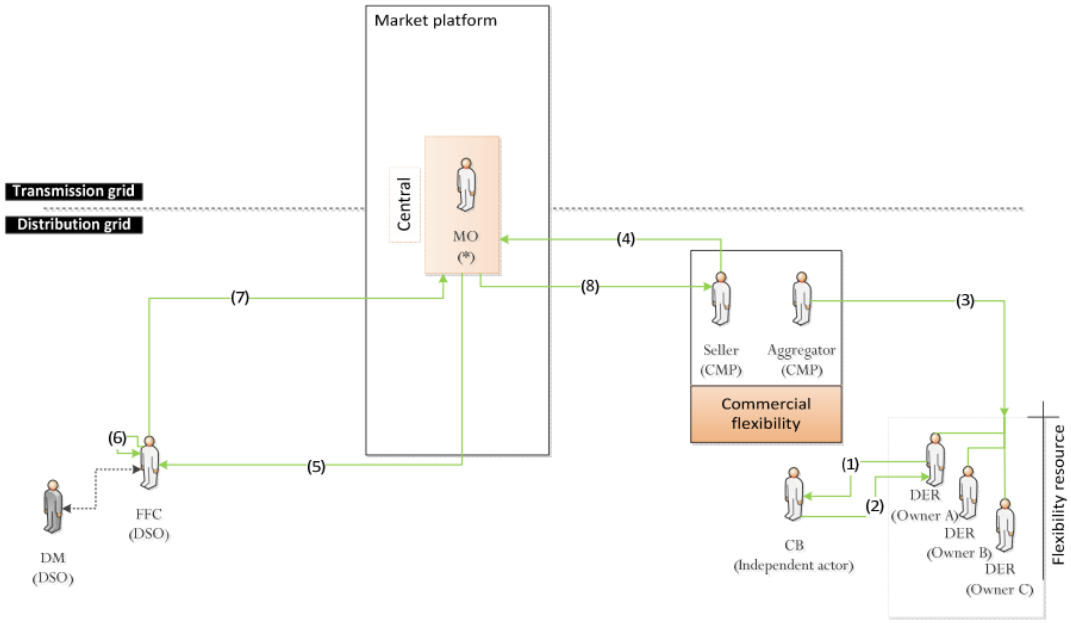

Figure 1.5: Pre-qualification coordination scheme with a centralized market design

In the context of procurement, activation, and settlement, the primary differences between coordination schemes lie in the procurement process, particularly concerning the organization and optimization of the market for resources connected to the distribution grid. Fig. 1.6 depicts the process for the procurement, activation, and settlement of the coordination schemes. The figure outlines all the steps, from determining the volume to be procured to the financial settlement of the flexibility activation for resources connected to both the distribution and transmission grids.

1.4 Role of Energy Storage System

The rising demand for green energy to reduce carbon emissions is accelerating the integration of renewable energy sources RESs like wind and solar power. However, this shift presents significant challenges due to the inherent variability and intermittency of RESs, which impact power system stability and reliability. As a result, there is a growing need for enhanced flexibility to maintain stable and reliable operations. This chapter provides a comprehensive overview of the role of energy storage systems ESSs in improving the flexibility and reliability of MGs. As mentioned in Chapter 1, MGs are generally powered

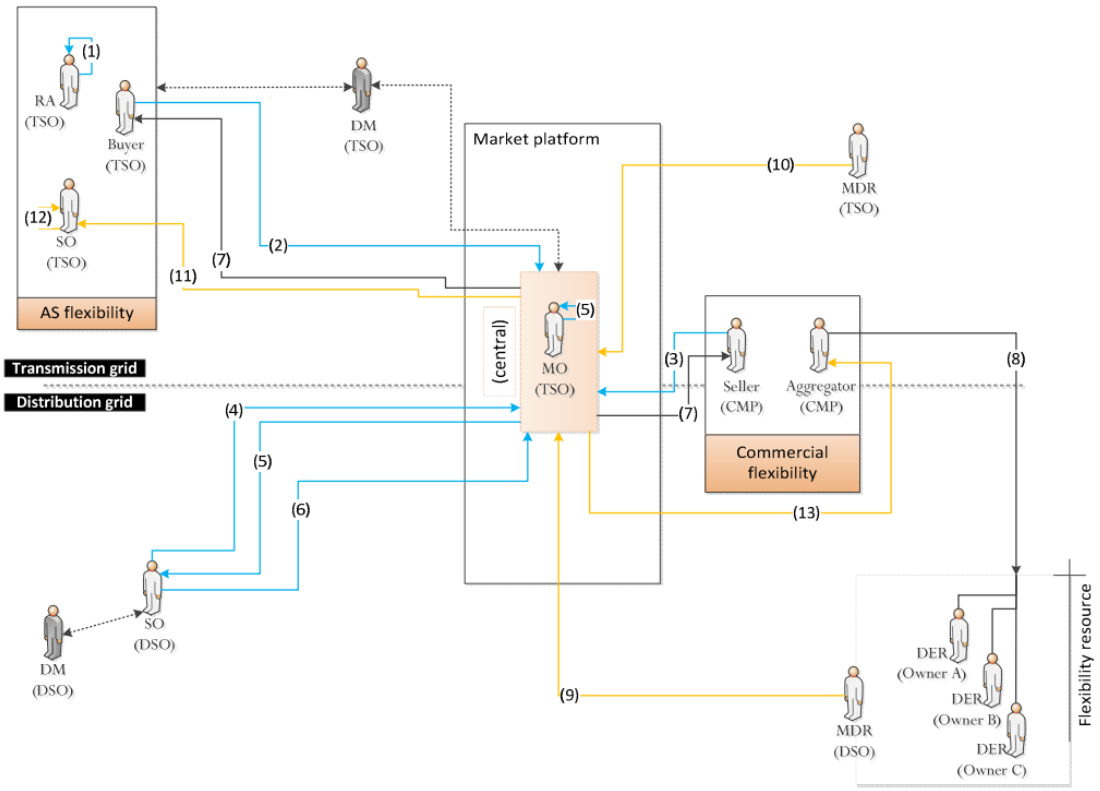

Figure 1.6: Procurement, activation, and settlement scheme for centralized market model

by DERs, which include photovoltaic (PV) systems, wind turbines, ESSs, and various types of loads.

ESSs play a vital role in addressing the variability of RESs, supporting grid stability, and enabling energy and ancillary services through MGs. This comprehensive chapter evaluates flexibility measures for renewable-based electricity in terms of reliability and stability, highlighting the importance of ESSs in power distribution networks, and end-user applications like residential buildings and vehicle-to-grid (V2G) technologies to enhance overall system flexibility. Additionally, it presents recent challenges, such as the increased risk of grid congestion, frequency deviations, and the need for real-time supply and demand balancing, which necessitate innovative ESSs applications. We propose future directions, including a transition pathway to promote the large-scale deployment of diverse ESSs technologies to support grid modernization, enhance resilience, and foster sustainable power supply development.

Numerous studies have defined power system flexibility by considering various types of ESSs and their applications across different sectors based on their categories, operations, and uses. Recent research highlights the role of ESSs in enhancing power system flexibility

through various applications. For instance, the techno-economic analysis of ESSs in power systems is discussed [69–71], while optimized economic planning operations of ESSs in power systems are covered in [72] and [73]. A study in [74], reviews scenarios for enhancing power system flexibility based on economic impacts and energy forecasting. The review in [75] discusses ESS applications with and without renewable energy integration. Studies in [76] and [77] address features, applications, and ancillary benefits of hybrid energy storage systems (HESS) for MGs. Furthermore, research in [78] and [79] highlights recent advancements in ESSs, their applications for RESs integration, comparative analysis among various ESSs, and their impacts on future power systems.

Power system reliability is crucial to maintaining a continuous power supply, supporting the integration of RESs, and enabling ancillary services, playing a vital role in improving reliability across various sectors of the power systems namely transmission, distribution, and end-user applications. Numerous studies in the literature address ESSs roles in maintaining power system reliability. For instance, a review in [80] evaluates ESSs reliability alongside other grid flexibility options, [81] investigates recent advancements and prospects of ESSs for improving reliability, and [82] explores ESS impacts on microgrid reliability in both grid-connected and isolated modes. Table 1.1 presents a comparison of various types of ESSs based on the different aspects, as mentioned in [80], [83], and [84]. Fig. 1.7 illustrates the significance and impact of ESSs applications within various power networks, as well as their role in enabling ancillary services across various power sectors. This figure differentiates between end-user and consumer services and identifies scenarios where no services are related to end-users, while also addressing the transmission and distribution networks.

1.4.1 Role of energy storage system in power distribution network

ESSs are crucial in power distribution networks, enhancing reliability and stability while increasing flexibility in managing the flow and quality of electric power. They serve as essential assets for load balancing and supply-demand matching within distribution networks, particularly important as power grids become more complex with the integration of RESs like wind and solar, along with the growth of distributed generation and variable loads [83–85].

Table 1.1: Comparison of various ESS on the basis of different aspects

ESSs categories	Types of ESSs	Life Span (Years)	Capacity	Energy Cost ($/kWh)	Efficiency (%)	Limitations
Electrical	SC	≥20	up to 300 kW	300-2000	90-95	• Low power density, • Low storage capacity, • Temperature influence on the environment.
	SMES	≥20	10 kW to 10 MW	1000-10,000	85-95	• Higher operational cost, • Higher maintenance cost, • Temperature influences the environment.
Electrochemical	Lead-acid	≤20	0.25-50 MWh	200-400	85-90	• Environmentally not friendly, • Thermal runaway due to inappropriate charging
	Li-ion	≤20	0.25-25 MWh	600-2500	85-97	• Deep charging is required for a long time, • Higher capital cost
	NaS	≤15	≤ 300 MWh	300-500	75-85	• Higher temperature is required, • Material degradation may appear due to corrosion.
	Ni-Cd	around 10	-	800-1500	70-90	• Lower energy density, • Toxicity issues, may cause environmental and health hazards.
	Vanadium redox flow	≤20	≤250 MWh	150-1000	75-80	• Higher design complexity, • Higher capital cost.
Mechanical	FESS	more than 20	kW range	1000-6000	85-90	• Lower energy density, • Higher capital cost, • Energy losses, friction, and aerodynamics losses occurrence.
	PHESS	40-60	up to 3 GW	5-100	75-80	• Geographic constraints, • Large land footprint: A large area is required for the reservoirs and associated infrastructure, • Ecological impacts, • Higher capital cost.

Table 1.1: (continued)

ESSs categories	Types of ESSs	Life Span (Years)	Capacity	Energy Cost ($/kWh)	Efficiency (%)	Limitations
	CAESS	20-40	25-350 MW	2-80	40-60	• Geological and environmental concerns, • High complexity design, • High capital cost
Chemical storage	Hydrogen based	5000 cycles in 15 years	-	5-30	45-75	• Low round-trip efficiency, • High cost of its production and transport infrastructure.
Thermal storage	Sensible heat storage	10-30	10-25 kWh/m^3	15-25	50-94	• Low energy density, • Limited temperature range, • High capital cost.
	Latent heat storage	10-30	50-150 kWh/m^3	25-35	75-90	• Limited suitable PCMs, • High capital cost, • Low thermal conductivity.
	High-temperature storage	20-30	120-250 kWh/m^3	16-43.6	75-95	• Maintenance of high-level thermal insulation, • Thermal expansion and contraction problems.

1.4.1.1 Load balancing and peak load shaving

ESSs helps to smooth demand fluctuation by discharging stored energy during peak demand periods and charging during low-demand times, a process known as peak shaving. This reduces the strain on distribution networks, improves load balancing, and can delay the need for costly infrastructure upgrades required to handle peak demands. By managing demand peaks and valleys, ESSs also enables distribution networks to maintain a more stable load profile, increasing the efficiency and lifespan of power grid components.

1.4.1.2 Backup power and resilience enhancement

Power system resilience and backup sources are crucial for ensuring a continuous power supply, especially during outages or grid failures, where backup sources play an essential role in maintaining uninterrupted service. ESSs, in this context, can be configured to operate in island mode, providing power independently to a localized section of the network or supplying critical loads until the main grid supply is restored.

1.4.1.3 Deferral of infrastructure upgrades

By managing peak demand and reducing load stress on existing assets, ESSs can delay the requirement for costly upgrades in distribution infrastructure, including substations, transformers, and transmission lines. This is especially beneficial in densely populated urban areas where expanding physical infrastructure is challenging. ESSs allow distribution operators to accommodate demand growth by considering the existing infrastructure, effectively deferring capital expenditures, and optimizing the current grid assets.

1.4.1.4 Demand response and energy arbitrage

Within a demand response framework, ESSs can respond to signals from grid operators to charge or discharge based on real-time demand conditions, offering added flexibility and supporting grid stability. By participating in the demand response programs, ESSs help balance grid demand during peak periods while also providing financial benefits and operational flexibility.

Additionally, ESSs can perform energy arbitrage by charging when electricity prices are low and discharging when prices are high, creating opportunities for cost savings and revenue generation, especially in deregulated markets where electricity prices frequently fluctuate.

1.4.1.5 Ancillary services provision

ESSs can support a wide range of ancillary services, such as spinning reserve, black start capability, and contingency reserve, which are generally provided by conventional power plants. By offering these services, ESSs enhance the operational flexibility and reliability of distribution networks while reducing reliance on conventional, often fossil-fuel-based sources. Moreover, as DERs become more common, ESSs offers a decentralized approach to delivering ancillary services, aligning well with the shift toward smart grid applications and distributed grid management.

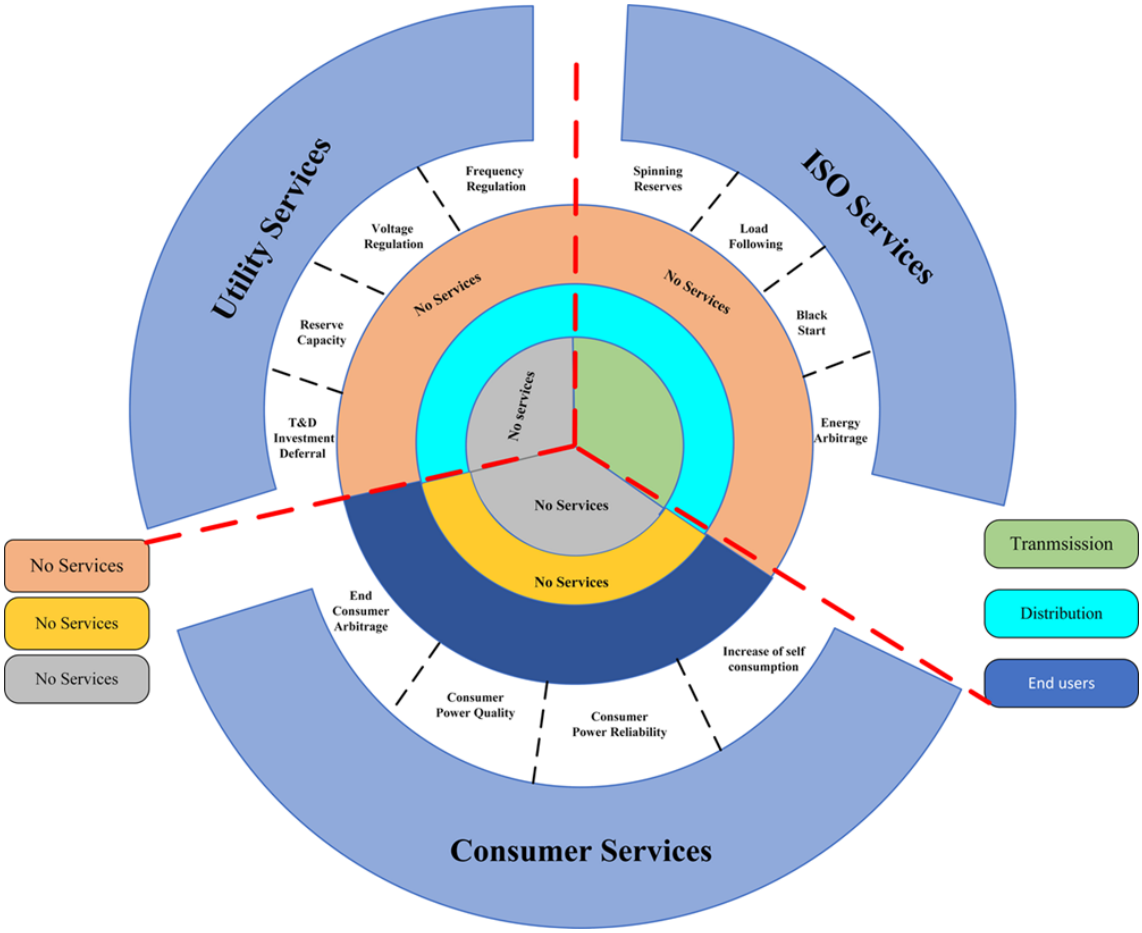

Figure 1.7: The significance of ESSs in diverse power networks and their role in facilitating ancillary services across various sectors

As discussed in detail in Section 1.4, the role of ESSs in various power system sectors enables the provision of energy and ancillary services alongside the contributions of RESs. In the subsequent Chapters 2, 3, and 4, we will explore how energy and ancillary services are delivered through MGs, considering the role of control and optimization methodologies both with and without the integration of storage systems.

Chapter 2

Demand Response Management

The previous chapters provided an overview of energy and ancillary services, highlighting the role of energy storage systems (ESSs) in supporting these services within power distribution, both for isolated and grid-connected Microgrid (MG)s, as well as in multi-energy storage systems. Furthermore, the previous studies were purely theoretical and did not incorporate the optimization program within a practical framework, such as integration into control architecture.

This chapter presents novel optimal control methodologies for demand response management in MGs and Multi-microgrids (MMGs), incorporating both open-loop and closed-loop formulations. These algorithms aim to optimize the operation of distributed energy resources (DERs) within MGs to manage demand response effectively, while also robustly attenuating the impacts of time-varying parameter variations and mitigating the effects of the variable nature of renewable energy sources (RESs) and load fluctuations. Similar to the approach discussed in previous chapters, this chapter addresses the optimal control architecture, developed using real-time data from a small Italian nanogrid-based building and a Chinese MMGs infrastructure, aimed at enhancing demand response management for end-users.

Nomenclature

u_i, s_i Vectors contain all continuous and integer control variables

g_i, h_i Sets of equality and inequality constraints

p_i, Set of input profile

C_{buy} Buying and selling cost of energy in €/kWh

C_{sell} Selling cost of energy in €/kWh

$\eta_{AC/DC}$ Efficiency of the bidirectional AC/DC converter

$\eta_{DC/AC}$ Efficiency of the bidirectional DC/AC converter

P_{sell}^{max} Maximum permissible power injection

P_{buy}^{max} Maximum allowable power purchase

η_{char} Charging efficiency

η_{dis} Discharging efficiency

α, β Weighting factors

SoC_{max} Maximum state of charge

SoC_{min} Minimum state of charge

R_1, R_2, and R_3 Number of ranges

Ψ_B^t Buying price

Ψ_S^t Selling price

$C_{bat,i}^t$ Overall charging and discharging cost of battery

$P_{char,i}^t$ Charging power of the BESS at time interval t

$P_{dis,i}^t$ Discharging power of the BESS at time interval t

$\alpha_{char,i}^t$ Boolean variable regarding the charging power state of the BESS

$\alpha_{dis,i}^t$ Boolean variable regarding the discharging power state of the BESS

Δt Scheduling time interval

$C_{sub,i}^{day}$ Subsidy provided by the governmental policies

C_{sup} Subsidy unit price value

$\mathcal{F}_i^t$ Cost function

γ Weighting factor

$|\beta|$ Number of participants in the subset β

$D_{b/s,i}^t$ Binary variable for power flow control

$\varphi_{b/s,i}^t$ Binary variable for power flow control

φ_{mS}^t Forecasted selling price of electricity

φ_{mb}^t Forecasted purchasing price of electricity

$D_{S,i}^t$ Selling electricity, decision variable

$D_{b,i}^t$ Buying electricity, decision variable

ω Auxiliary state variable

A, B, E, W Constant matrices

C_b Battery aging cost

$C_{gi}(t)$ Generation cost

σ Auxiliary decision variable
E_b Battery capacity
ζ State variable
E_{rated} Rated capacity
Y Admittance matrix
C_{ik} Auxiliary variable
S_{ik} Auxiliary variable
Γ Robustness factor

2.1 Optimal control algorithm for residential hybrid AC-DC nanogrid

The depletion of conventional energy sources and the growth of renewable distributed sources are rapidly shifting attention toward new smart systems and solutions to enhance energy efficiency and reduce energy costs in the residential sector, enabling the end-user to save more while managing the demand response [86, 87]. To meet these needs, a model predictive control-based energy management algorithm has been proposed and applied to a residential hybrid nanogrid in this section. Residential hybrid alternating current (AC)-Direct Current (DC) nanogrid is characterized by an innovative conductive flat tape, while a mixed-integer linear programming approach has been considered in the design of the proposed algorithm. Furthermore, simulation tests have been performed to check the effectiveness of the proposed algorithm for residential hybrid AC-DC nanogrid by considering various kinds of AC and DC loads.

Furthermore, incorporating a DC nanogrid into residential buildings can enhance the efficiency of the electrical system and reduce costs. However, implementing a hybrid AC-DC nanogrid often requires extensive and costly renovations. This challenge is addressed in the literature in [88], who propose a hybrid AC-DC MG architecture that avoids the need for a complete system redesign. Additionally, building modernization can be supported by new technologies, components, and cloud-based energy management systems with multi-protocol gateways, enabling compatibility with legacy devices. This section of the chapter presents an model predictive control (MPC) algorithm for optimal energy management in residential buildings with hybrid AC-DC nanogrids. The proposed optimization algorithm

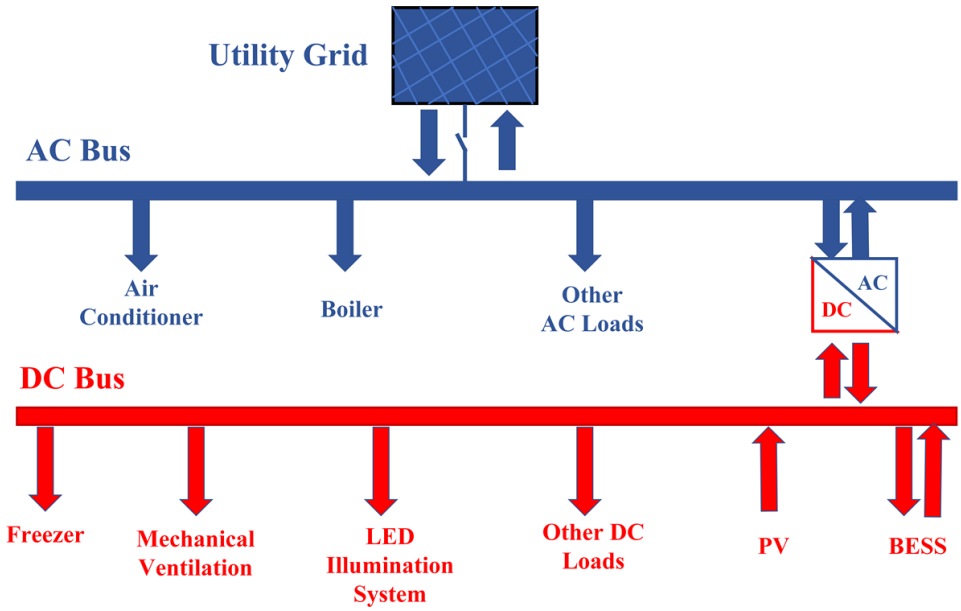

Figure 2.1: The AC-DC hybrid architecture of the residential building under investigation

is designed to maximize self-consumption and minimize energy purchases from the utility grid.

2.1.1 Residential hybrid AC-DC nanogrid architecture

This subsection outlines the architecture of the residential building that serves as the basis for this work, as depicted in (Fig. 2.1).

2.1.1.1 Optimization problem

The optimization problem begins at the start of the controlled time window T. By defining the number of time-steps in an hour as n (i.e. 12 with 5-minutes time-step), the optimization algorithm seeks to minimize operating costs and maximize self-consumption while adhering to technical constraints. Thus, a discrete predictive optimal management problem is formulated, assuming that state and control variables remain constant over each i-th time-step. The calculated optimal set points are then supplied to a real-time control layer. With a moving time window T of the fixed 24-hour duration, the proposed optimal control methodology allows for updating the optimal set-points every m hours. The iterative control scheme can be summarized as follows:

1. the index k, indicating the k-th hour, is initialized to 0;

2. the battery's state is initialized at the beginning of the optimization time window T;

3. formulation and solution of the discrete optimal control problem in the time window $T = [t_k, t_{k+24}]$ and determination of the set-points for all the controllable resources for each i-th time-step in that interval ($24 \cdot n$ time-steps);

4. application of the set-points and real-time operation during the time interval $[t_k, t_{k+m}]$ and acquisition of sate of charge (SOC) state at the end of the interval (SoC_{k+m});

5. shifting of the optimization time window: k is incremented by m and move to step 2.

The described recursive control scheme compensates for discrepancies between forecasts and real-time behavior. During operation, the optimal set points are applied to the actual system, where energy balance must be maintained despite unexpected net-load fluctuations.

2.1.1.2 Predictive optimal dispatch problem formulation

For each optimization time window T, the discretized optimal control problem can be formulated as follows:

$$\min_{\boldsymbol{u},\boldsymbol{s}} F = \min_{\boldsymbol{u},\boldsymbol{s}} \sum_{i=1}^{24\cdot n} f_i(\boldsymbol{u}_i, \boldsymbol{s}_i, \boldsymbol{p}_i), \tag{2.1}$$

subject to

$$\boldsymbol{g}_i(\boldsymbol{u}_i, \boldsymbol{p}_i) = 0; \tag{2.2a}$$

$$\boldsymbol{h}_i(\boldsymbol{u}_i, \boldsymbol{s}_i, \boldsymbol{p}_i) \leq 0, \tag{2.2b}$$

where for each i-th time-step within T, $\boldsymbol{g}_i$ and $\boldsymbol{h}_i$ represent the sets of equality and inequality constraints, respectively. The vectors $\boldsymbol{u}_i$ and $\boldsymbol{s}_i$ contain all continuous and integer control variables, respectively, which are used to linearize the system formulation, while $\boldsymbol{p}_i$ holds the forecasted input profiles. The variables $\boldsymbol{u}$, $\boldsymbol{p}$ and $\boldsymbol{s}$ have been selected based on the architecture shown in Fig. 2.1.

The proposed optimal control methodology also aims to optimize hot water consumption, the AC-DC nanogrid under consideration includes an AC boiler that can only be switched on twice a day during specific time intervals. For each i-th time-step in T, the set of control variables $\boldsymbol{u}_i$ consists of the following: the electric power purchased from and sold to the utility grid, denoted as u^i_{buy} and u^i_{sell}, respectively; the powers exchanged between AC and DC buses, represented by $u^i_{AC/DC}$ and vice versa $u^i_{DC/AC}$; the BESS charging power u^i_{cha} and discharging power u^i_{dis}; and the power demand variations $u^i_{1,AC}, \ldots, u^i_{n_{AC},AC}$ for the n_{AC} loads connected to the AC bus, as well as $u^i_{1,DC}, \ldots, u^i_{n_{DC},DC}$ of the n_{DC} loads

connected to the DC bus. As the optimization time window advances, the 24 h period can encompass two occurrences of either the first or second time slot designated for activating the boiler. Consequently, different control variables have been introduced to differentiate the control actions scheduled for the first and second slots over two consecutive days: $u^i_{boil,1'}$ and $u^i_{boil,2'}$ represent the boiler's power consumption in the first time slot of the current and following solar day, respectively, while $u^i_{boil,1''}$ and $u^i_{boil,2''}$ denote the power consumption of the boiler in the second time slot of the current and subsequent solar day, respectively.

Furthermore, to account for all the elements that introduce discontinuities in the formulation, the integer variable collected in $\boldsymbol{s}_i$ for each i-th time step are as follows: s^i_{buy} is 1, if power is purchased/bought from the grid, and 0 if it is sold; $s^i_{AC/DC}$ is 1, if power flows from the AC bus to the DC bus, and 0 otherwise; s^i_{cha} is 1, when the battery energy storage systems (BESS) is in charging mode, and 0 when it is in discharging mode; $s^i_{boiler,1'}, s^i_{boiler,2'}, s^i_{boiler,1''}, s^i_{boiler,2''}$ are each 1, if the boiler is on, and 0 if it is off during the respective time intervals indicated by the indices ($1'$, $2'$, $1''$ and $2''$). Finally, at each i-th time step, the set of input profiles $\boldsymbol{p}_i$ consists of the following forecasted powers: the production from photovoltaic (PV) modules p^i_{PV}, the demand profiles $p^i_{1,AC}, ..., p^i_{n,AC}$ for the n_{AC} AC loads, the demand profiles $p^i_{1,DC}, ..., p^i_{n,DC}$ for the n_{DC} DC loads, and the demand profile $p^i_{f,l}$ for a DC fixed load, such as freezer.

2.1.1.3 Objective function

The proposed optimal control methodology seeks to optimize power exchange with the grid over a designated time window T. The objective function to be minimized, consisting of two components, is formulated as shown in Eq. (2.3). The first term indicates the income from energy sales normalized against the maximum remuneration from PV power generation, assigning fixed unit costs c_{buy} and c_{sell} (€/kWh) to the purchased and sold energy, respectively. The second term accounts for the system self-consumption index (SSCI), as indicated in [89, 90]. This index is calculated as the ratio of the amount of generated PV power that supplies the nanogrid loads (including both AC and DC devices) and charges the battery to the total amount of generated PV power.

$$F = \alpha \cdot \frac{\sum_{i=1}^{24\cdot n} c_{buy} \cdot u^i_{buy} - c_{sell} \cdot u^i_{sell}}{\sum_{i=1}^{24\cdot n} c_{sell} \cdot \eta_{DC/AC} \cdot p^i_{PV}} + \beta \cdot \frac{\sum_{i=1}^{24\cdot n} \min\left(p^i_{eq,DC} + u^i_{cha}; p^i_{PV}\right)}{\sum_{i=1}^{24\cdot n} p^i_{PV}}, \tag{2.3}$$

with

$$p^i_{eq,DC} = \sum_{j=1}^{n_{AC}} \left(\frac{p^i_{j,AC} - u^i_{j,AC}}{\eta_{DC/AC}} \right) + \sum_{j=1}^{2} \left(\frac{u^i_{boil,j'} + u^i_{boil,j''}}{\eta_{DC/AC}} \right) + \sum_{j=1}^{n_{DC}} \left(p^i_{j,DC} - u^i_{j,DC} \right) + p^i_{f,l}. \tag{2.4}$$

At a specific i-th time step, the equivalent total power demand $p^i_{eq,DC}$ (kW) is calculated as shown in Eq. (2.4). The two components are weighted by factors α and β. A higher α relative to β, will favor maximizing energy sales; whereas a higher β, the solution will promote increased self-consumption.

2.1.1.4 Constraints in the optimization problem

1. **DC-bus and AC-bus energy balances**: Assuming injected power is positive, the energy balance for the DC bus at each i_{th} time step within the time window T is as follows:

$$\eta_{AC/DC} \cdot u^i_{AC/DC} + u^i_{dis} + p^i_{PV} = \sum_{j=1}^{n_{DC}} \left(p^i_{j,DC} - u^i_{j,DC} \right) + u^i_{cha} + u^i_{DC/AC} + p^i_{f,l}. \tag{2.5}$$

   The energy balance for the AC bus is formulated, as follows:

$$\eta_{DC/AC} \cdot u^i_{DC/AC} + u^i_{buy} = \sum_{j=1}^{n_{AC}} \left(p^i_{j,AC} - u^i_{j,AC} \right) + u^i_{sell} + u^i_{AC/DC} + u^i_{boil,1'} + u^i_{boil,2'} + u^i_{boil,1''} + u^i_{boil,2''}, \tag{2.6}$$

   where $\eta_{AC/DC}$, and $\eta_{DC/AC}$ represent the efficiency of the bidirectional converter for power flowing from the AC bus to the DC bus and vice versa, respectively.

2. **Power interaction between AC bus and DC bus**: At each i-th time step, the limits on maximum power flow from the AC bus to the DC bus, and vice versa, are taken into account as:

$$0 \leq u^i_{AC/DC} \leq s^i_{AC/DC} \cdot P^{max}_{AC/DC}; \tag{2.7a}$$

$$0 \leq u^i_{DC/AC} \leq \left(1 - s^i_{AC/DC} \right) \cdot P^{max}_{DC/AC}, \tag{2.7b}$$

   where $P^{max}_{AC/DC}$, and $P^{max}_{DC/AC}$ (kW) are maximum powers set for the bidirectional converter.

3. **Power exchange with grid**: At each i-th time step, Eq. (2.8) restricts the power

bought from the utility grid to a range of 0 to P_{buy}^{max} (kW), which represents the maximum allowable electric power purchase at the point of common coupling (PCC) as specified in the energy supply contract.

$$0 \leq u_{buy}^{i} \leq s_{buy}^{i} \cdot P_{buy}^{max}. \tag{2.8}$$

Similarly, at each i-th time step, Eq. (2.9) limits the power sold to the grid from 0 to P_{sell}^{max} (kW), which represents the maximum permissible power injection at the PCC.

$$0 \leq u_{sell}^{i} \leq \left(1 - s_{buy}^{i}\right) \cdot P_{sell}^{max}. \tag{2.9}$$

4. **Battery energy storage system**: Assuming storage efficiency is independent of state and control variables, the energy stored (kWh) at the start of each i-th time step is calculated as follows:

$$Q_b^i(\boldsymbol{u}) = Q_b^k + \sum_{j=k}^{i-1} \left(\eta_{cha} \cdot u_{cha}^j - \frac{u_{dis}^j}{\eta_{dis}} \right) \cdot \Delta t, \tag{2.10}$$

where Q_b^k (kWh) is the energy stored at the beginning of the optimization time window T, η_{cha} and η_{dis} are the charge and discharge efficiency, respectively.

At each i-th time step, Eqs. (2.11) and (2.12) accounts for the maximum charging and discharging powers, respectively, and Eq. (2.13) considers the minimum and maximum capacity of the BESS.

$$0 \leq u_{cha}^{i} \leq P_b^{max} \cdot s_{cha}^{i}; \tag{2.11}$$

$$0 \leq u_{dis}^{i} \leq \left(1 - s_{cha}^{i}\right) \cdot P_b^{max}; \tag{2.12}$$

$$Q_b^{min} \leq Q_b^i(\boldsymbol{u}) \leq Q_b^{max}; \tag{2.13}$$

$$Q_b^{min} = SoC_{min} \cdot Q_n \ , \ Q_b^{max} = SoC_{max} \cdot Q_n. \tag{2.14}$$

In equations (2.11)-(2.12) the factor P_b^{max} (kW) represents the rated power of BESS, while Q_b^{min} (kWh) and Q_b^{max} (kWh) in equations (2.13)-(2.14) denote the minimum and the maximum storable energy, respectively. These values correspond, through (2.14), to the minimum (SoC_{min}) and maximum (SoC_{max}) state-of-charge conditions (%) for a BESS with rated capacity of Q_n (kWh).

5. **Boiler management**: Assuming that the boiler requires always its rated power P_{boil} when is on, the constraints (2.15) have been considered:

$$u^{i}_{boil,w} = s^{i}_{boil,w} \cdot P_{boil}. \tag{2.15}$$

In this context, w represents the time slots during which the boiler can be activated, labeled as $1'$, $2'$, $1''$, and $2''$. As mentioned above, the boiler is allowed to switch on only twice a day, within designated time intervals, for a fixed duration T_{on} (i.e. 4.5 hours) to sufficiently heat water for domestic use. Given the start hour $h_{s,w}$ and end hour $h_{e,w}$ for each possible activation, various conditions must be incorporated into the optimization problem based on its start time. Although this part of the formulation is not given here in order to be concise, it is explained, and its impact is demonstrated through the simulation results.

On the current day (when w is either $1'$ or $1''$), if the optimization start hour k falls within the range $[h_{s,w}, h_{e,w}]$, the optimization algorithm first checks whether the boiler is already on. If so, it defines a time step interval R during which the boiler must remain on to satisfy the required duration T_{on}. In this interval, the boiler's state variable is set to 1, while for all other time steps, it is set to 0. If the condition is false or if the start hour of the optimization k is outside the range $[h_{s,w}, h_{e,w}]$, the proposed optimal control methodology defines three distinct time-step intervals:

- R_1: an interval during which the boiler must remain off (state variable set to 0).
- R_2: a range during which the boiler can be switched on.
- R_3: a range in which the boiler's state variable must equal 1 for at least one time step, ensuring that the boiler can remain for the fixed duration T_{on} within the specified time slot. Within this interval, the following inequality constraint is applied.

$$\sum_{i \in R_3} s^{i}_{boil,w} \geq 1. \tag{2.16}$$

By defining these ranges and conditions, all potential activation times for the boiler are accounted for, allowing the optimization methodology to select the optimal start time. Activation times on the following day (when 0 w can be equal to $2'$ or $2''$) are handled similarly. However, only the ranges R_1 and R_2 are defined for any given k. The range R_3 and constraint (2.16), are included in the optimization methodology only if the time $h_{e,w} - T_{on}$ falls within the time window T.

6. **Load power optimization**: At each i-th time step, for each j-th DC-connected load (n_{DC} in total), eq. (2.17) limits the power demand variations. Positive values indicate a reduction, in power demand, while negative values cause an increase in the j-th load's consumption. The upper limit is set to a fraction f_j of the forecasted consumption for the j-th load, whereas the lower limit permits an increase in consumption by a fraction f_j of the difference between the maximum $P^{max}_{j,DC}$ (kW) and the forecasted demand of the j-th load.

$$-f_j \cdot \min\left(P^{max}_{j,DC} - p^i_{j,DC}, p^i_{j,DC}\right) \leq u^i_{j,DC} \leq f_j \cdot p^i_{j,DC}. \tag{2.17}$$

Likewise, at each i-th time interval, Eq. (2.18) constraints the power demand variations for each j-th PV-connected load (with n_{AC} in total) with a maximum demand of $P^{max}_{j,AC}$ (kW).

$$-f_j \cdot \min\left(P^{max}_{j,AC} - p^i_{j,AC}, p^i_{j,AC}\right) \leq u^i_{j,AC} \leq f_j \cdot p^i_{j,AC}. \tag{2.18}$$

2.1.2 Simulation results and discussion

The effectiveness of the proposed MPC-based energy management was evaluated through interactive simulations involving an optimization methodology and a real-time control layer model. The optimization problem is solved using the GUROBI linear optimization solver within the YALMIP platform. The electrical system model was based on an actual implementation of a residential nanogrid, developed through a rapid and non-invasive refurbishment using innovative conductive tapes, allowing for integration without replacing any existing devices. Referring to the architecture shown in Fig. 2.1, the AC/DC converter is a $230/48$ V bidirectional converter with a rated power exceeding 10 kW. The PV system and the BESS have capacities of 9 kWp and $5/7$ kW/kWh, respectively. The AC bus can exchange active power with the utility grid up to 9.9 kW, accounting for the 10% tolerance on the 9 kW energy supply contract.

The investigation began with the potential forecasted power profiles for the AC and DC loads and the PV system of the residential nanogrid. These data profiles were utilized to achieve an optimal power dispatch of energy sources aimed at minimizing the total power supply cost and maximizing the SSCI. Small load variations and optimal BESS set-points, derived from the optimization problem solutions, were applied to the real-time control layer for a duration of $m = 4$ hours. The real-time SOC of the BESS was then used for further optimization to provide updated set-points for the real-time control of the

MPC implementation. The data profiles examined in this study span six consecutive days, however, for brevity, only the analysis from the first day is presented in detail.

For this day, the power balance for the base test case without optimization, as well as for open-loop optimization and post-optimization scenarios, is illustrated in Fig. 2.4. The no-optimization case is based on a real-time rule-based energy management strategy for commercial devices: the PV power is first utilized to supply the loads, with any surplus energy stored in the BESS. If there is additional power, it is sold to the utility. Conversely, if the PV power is insufficient, the remaining load is met by the energy stored in the BESS or, if necessary, supplemented by the utility grid. The boiler was activated during designated time slots, specifically from 2:30 to 7:00 AM and from 11:30 AM to 4:00 PM. Following this strategy, in the base test case, the BESS, starting with an initial SOC of 50%, is charged during the early hours when the PV generates enough energy to supply the loads and charge the BESS. This stored energy is not utilized again until around 5:00 PM when the BESS discharges to meet the loads due to insufficient PV energy. In this scenario, the total energy cost for the day amounted to € 17.23. In Fig. 2.2, and Fig. 2.3 the load power demands (dashed lines) are compared to the actual power consumption (solid lines) for both AC and DC loads. The optimization algorithm activates the boiler from 1:55 am to 6:25 am and again from 9:40 am to 2:10 pm, starting earlier than the fixed time slots in the non-optimized case.

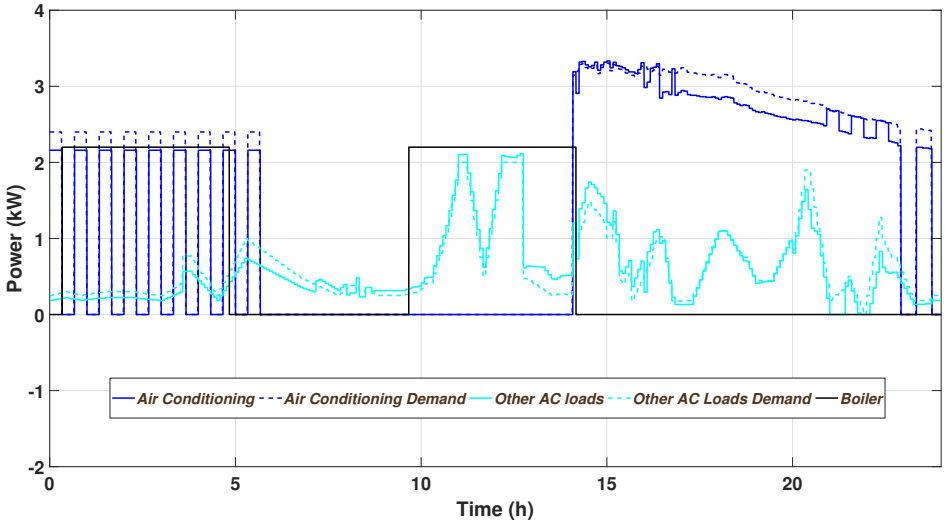

Figure 2.2: AC loads profiles

For the open-loop optimization, the same problem outlined in Section 2.1.1.1 was utilized, but without applying the MPC approach. The optimal set points for the nanogrid's resources were established at the beginning of the day. The weights and parameters set

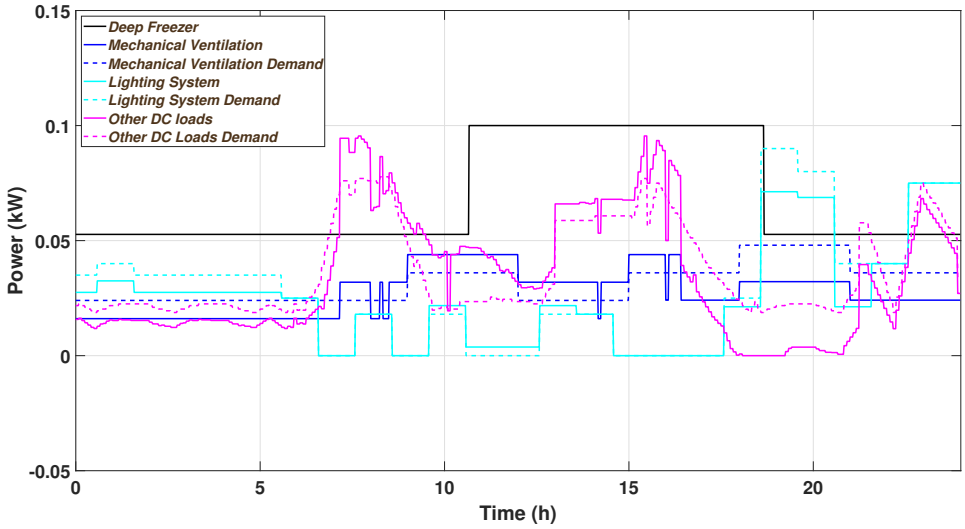

Figure 2.3: DC loads profiles

for the optimization problem are as follows: $\alpha = 1.00$, $\beta = 1.00$, $f_1 = 0.33$, $f_2 = 0.30$, $f_3 = 0.32$, $f_4 = 0.10$, and $f_5 = 0.26$. With the optimization algorithm, the BESS is utilized more effectively to maximize self-consumption and minimize the overall energy cost. As a result, the overall energy cost with optimization is reduced to € 13.77, reflecting a savings of approximately 20% compared to the base test case. When applying the proposed MPC approach, the energy cost for the same day is further reduced to € 13.51, slightly lower than that of the open-loop optimization, resulting in a savings of 21.6% compared to the base test case, with a remaining SOC of about 32% at the end of the day. This residual energy stored in the BESS is beneficial for supplying loads during the early hours of the next day when PV generation is unavailable. Over the six consecutive days simulated, optimization resulted in a total overall cost savings of 21.1% (total cost of € 68.68), while open-loop optimization achieved a savings of 18.6% (total cost of € 70.85) compared to the base test case (total cost of € 87.00).

The final activation is triggered by the PV plant's power production which is already substantial by 9:40 am (Fig. 2.4). Consequently, the optimization algorithm immediately switches on the boiler and increases the energy consumption of other controllable loads to maximize self-consumption.

This research activity concludes with the development and testing of an MPC algorithm for optimal energy management in a hybrid AC-DC residential nanogrid. The results demonstrate that the proposed optimization methodology effectively identifies the ideal times to activate the boiler and manages both the BESS and controllable loads to maximize energy self-consumption and minimize overall energy costs. Future work may focus

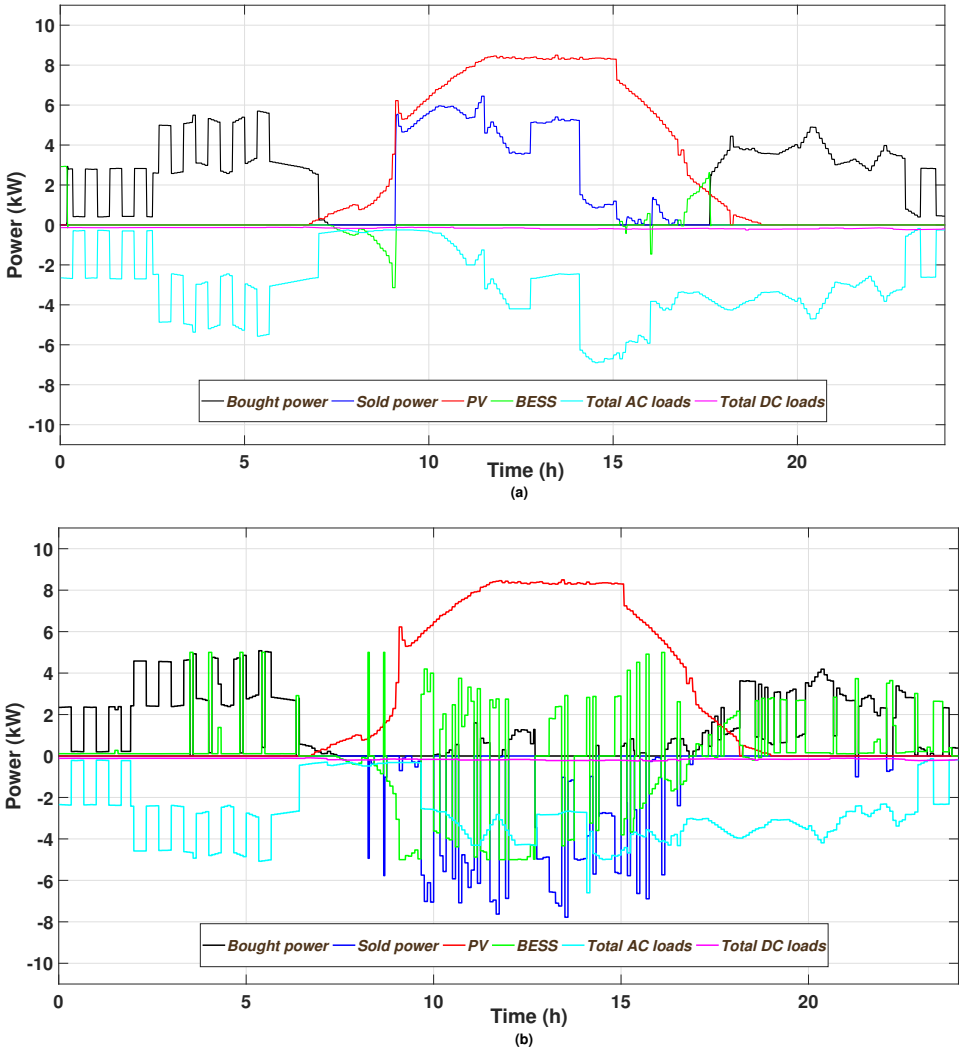

Figure 2.4: **(a)** Total power balancing without optimization **(b)** in the case of proposed controller.

on refining the methodology to reduce BESS charging/discharging cycles. Additionally, subsequent studies may explore integrating artificial neural network algorithms with MPC to forecast and manage large PV datasets for applications in historical and industrial buildings.

2.2 Optimizing cooperative alliance transactive energy framework for PV-based MMGs

As mentioned in Section 2.1, the variability and uncertainty of RESs can pose significant challenges, especially when combined with load variations. Consequently, a key issue

facing power distribution networks is managing energy consumption, particularly due to the integration of PV-based MG clusters on the distribution network side [91, 92]. To tackle these challenges and encourage greater self-consumption of PV energy—thereby, reducing the impact of PV-based MMGs on the main power grid—this section introduces an optimized cooperative alliance transactive energy framework. This proposed framework seeks to reduce the overall operational costs of the system while ensuring equitable benefits for all contributors. To achieve more effective scheduling of their operations, optimal scheduling has been implemented, incorporating the mathematical modeling of MGs. Additionally, a cooperative alliance framework based on the Shapley value method has been utilized to fairly distribute the benefits among all participants. The Time of Use (TOU) electricity pricing mechanism is employed to compare electricity prices for both independent and cooperative alliance operations of MGs during peak, valley, and flat conditions.

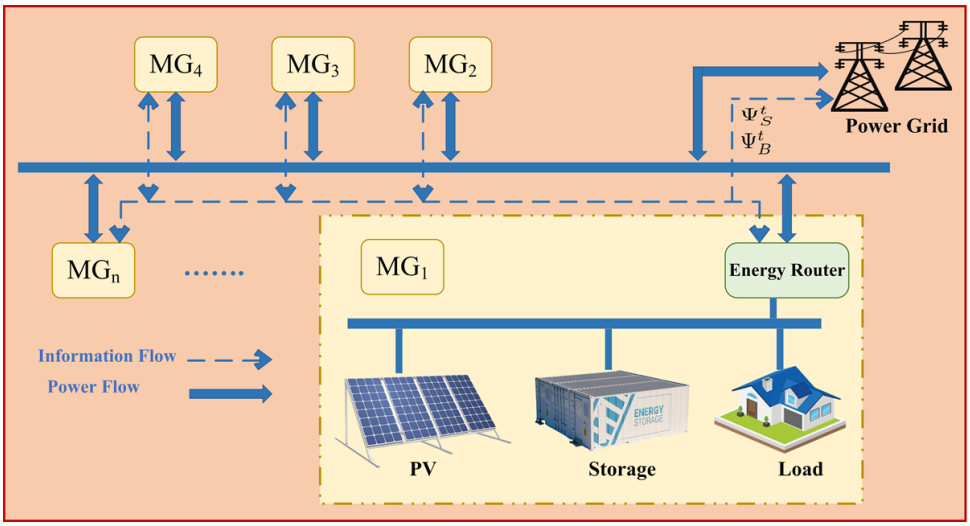

Figure 2.5: Control architecture of MMGs

2.2.1 Architecture of MMG

This section investigated a Chinese grid-connected PV-based MMGs model. Fig. 2.5 depicts the control architecture of PV-based MMGs. The proposed MMGs model comprises PV panels for power generation, the BESS, and loads with varying capacities. Each MG can communicate with the main power grid through an energy router and can also share power with other MGs within a cooperative alliance. At any given time interval t, the transaction electricity prices between the main power grid and the MG are denoted by

Ψ^t_B and Ψ^t_S, respectively. Here, Ψ^t_B refers to the buying price at which the MG purchases electricity from the main grid, while Ψ^t_S indicates the selling price at which the MG sells electricity back to the main power grid [8].

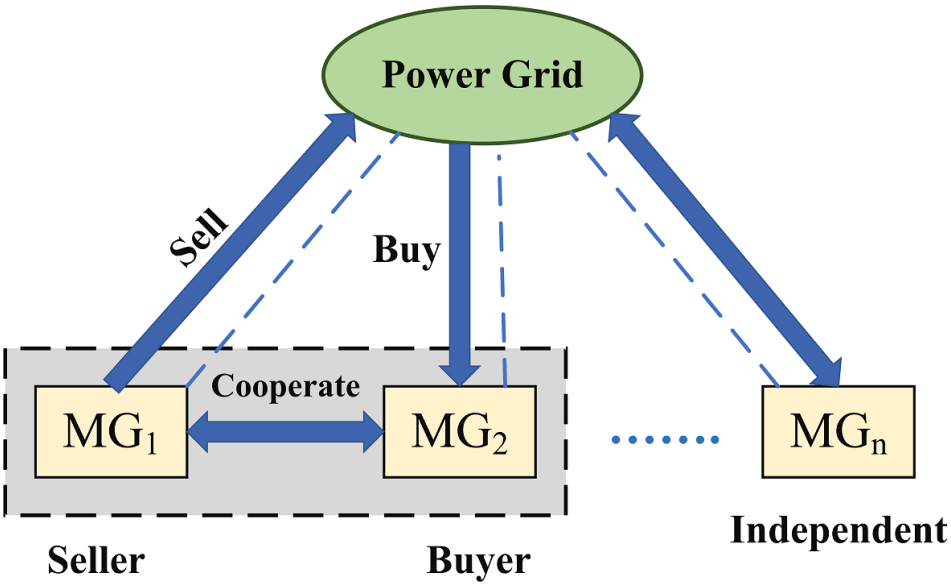

Figure 2.6: Transactive energy framework of MMGs

2.2.1.1 Energy transaction model of MMG

This subsection explains the energy transaction model for PV-based MMGss. Fig. 2.6 presents the proposed model for energy transactions in PV-based MMGss. During the same dispatch period, different MGs may experience varying conditions, leading to different net power outcomes for each MG. Furthermore, multiple MGs can operate under different conditions, either independently or cooperatively. In independent operation, an MG is considered self-sufficient and does not interact with other MGs. However, in cooperative mode, an MG can supply or share surplus energy with other MGs that are power-deficient and can also sell energy back to the main power grid. Thus, within the proposed framework, residual energy is efficiently utilized, reducing the electricity cost for each MG and generating additional revenue through the cooperative alliance model.

2.2.2 Mathematical formulation of MMG model under analysis

This subsection describes the modeling of PV systems, BESS, loads, and energy trading within the MMGs model being examined.

2.2.2.1 PV and load modeling

In this study, PV systems are treated as a source of clean, renewable energy. Since PV is a renewable resource, the costs associated with power generation from PV are not included in the analysis. Let $P_{PV,i} = \{P^1_{PV,i}, P^2_{PV,i}, P^3_{PV,i}, P^4_{PV,i}.....P^T_{PV,i}\}$ denote the set of PV power generation values for the ith MG over the period from 1 to T. Similarly, let $P_{L,i} = \{P^1_{L,i}, P^2_{L,i}, P^3_{L,i}, P^4_{L,i}.....P^T_{L,i}\}$ represent the set of load power values for the ith MG model during the same time period T.

2.2.2.2 BESS modeling

This subsection presents the modeling of the BESS for the system being analyzed. The cost function of the BESS is given by the following expression:

$$C^t_{bat,i} = C_{bat}(P^t_{char,i}.\eta + \frac{P^t_{dis,i}}{\eta}), \tag{2.19}$$

where $P^t_{char,i}$ and $P^t_{dis,i}$ represent the charging and discharging power of the BESS at time interval t, respectively, while η denotes the efficiency of the BESS. Additionally, $C^t_{bat,i}$ indicates the overall charging and discharging cost of the BESS, measured in RMB/kWh.

Due to the uniform scheduling interval Δt for BESS across multiple MGs, the BESS can only operate in one mode/state at a time, either charging or discharging state. Boolean variables have been introduced to indicate the BESS's operational state. The equation representing the storage capacity of the BESS during the scheduling time interval Δt can be expressed as follows:

$$\xi^{t+1}_i = \eta \Delta t \alpha^t_{char,i} \xi^t_i P^t_{char,i} - \frac{P^t_{dis,i} \alpha^t_{dis,i} \Delta t}{\eta}, \tag{2.20}$$

where $\alpha^t_{char,i}$ and $\alpha^t_{dis,i}$ are the boolean variables indicating the charging and discharging power states of the BESS, respectively, and let ξ_i represents the remaining storage capacity of BESS. The scheduling time interval Δt is considered to be 0.5h in this study.

The BESS must satisfy both the upper and lower limits, along with the constraints on

charging and discharging power. The initialization of the BESS is as follows:

$$0 \leq P^{t}_{char,i} \leq P^{max}_{char,i}\alpha^{t}_{char,i}; \tag{2.21a}$$

$$0 \leq P^{t}_{dis,i} \leq P^{max}_{dis,i}\alpha^{t}_{dis,i}; \tag{2.21b}$$

$$\xi_{min} \leq \xi^{t}_{i} \leq \xi_{max}; \tag{2.21c}$$

$$\alpha^{t}_{char,i} + \alpha^{t}_{dis,i} \leq 1; \tag{2.21d}$$

$$\xi^{0}_{i} = \xi^{T}_{i}, \tag{2.21e}$$

where $P^{max}_{char,i}$ and $P^{max}_{dis,i}$ denote the maximum charging and discharging power of the BESS in kW, respectively. Meanwhile, ξ_{max} and ξ_{min} represent the maximum and minimum storage capacity values of the BESS in kWh, and T indicates the scheduling period in hours.

2.2.3 Energy trading modeling with distribution network

The PV-based MG model used in this study is built on a framework that prioritizes local load demand. In this model, the independent MG is connected to the distribution network through power lines to maintain the power balance within the proposed network. The cumulative power balance between the distribution network and the MG can be defined as follows:

$$P^{t}_{accu,i} = P^{t}_{L,i} + P^{t}_{char,i} - P^{t}_{PV,i} - P^{t}_{dis,i}, \tag{2.22}$$

where $P^{t}_{accu,i}$ represents the cumulative energy transition between the independent MG and the power distribution during the dispatching time interval t. According to the proposed trading criteria, if $P^{t}_{accu,i} > 0$ then the MG will purchase electricity from the power distribution network. Conversely, if $P^{t}_{accu,i} < 0$, the MG will sell power to the distribution network to meet load demands.

Furthermore, within the same scheduling interval, only one transaction state can occur at any given time. To distinguish between selling and purchasing, the proposed study introduces an auxiliary variable that includes the following constraints in the transaction

model:

$$P^t_{accu,i} = P^t_{B,i} - P^t_{S,i}; \tag{2.23a}$$

$$0 \leq P^t_{B,i} \leq P^{max}_{accu,i}\alpha^t_{B,i}; \tag{2.23b}$$

$$0 \leq P^t_{S,i} \leq P^{max}_{accu,i}\alpha^t_{S,i}; \tag{2.23c}$$

$$\alpha^t_{B,i} + \alpha^t_{S,i} \leq 1, \tag{2.23d}$$

Eq.(2.23a) illustrates the relationship between the accumulative power and the power bought and sold by the MG, where $P^t_{B,i}$ denotes the power bought by the MG and $P^t_{S,i}$ represents the power sold by the MG. Eqs.(2.23b) to (2.23d) illustrate the maximum power capacity of the MG power line, and the boolean variables $\alpha^t_{B,i}$ and $\alpha^t_{S,i}$ represent the buying and selling states of the MG power, respectively.

At present, many countries are accelerating the adoption of PV-based MGs by promoting sustainable energy and providing economic incentives, such as subsidies [93]. In this study, we applied the subsidy factor as follows:

$$C^{day}_{sub,i} = \sum_{t=1}^{T} (\lambda_{dis,i}(t).P_{dis,i}(t)).C_{sup}, \tag{2.24}$$

where $C^{day}_{sub,i}$ represents the amount of subsidy provided by the governmental policies, $\lambda_{dis,i}(t)$ represents the discharging rate of BESS, and C_{sup} denotes the subsidy unit price value.

2.2.4 Independent operation of MG

In the proposed MG model, the operation cost is split into two components: the cost associated with energy transactions with the distribution network and the cost of optimizing the ESSs. The operational cost function of the MG is expressed as follows:

$$\mathcal{F}^t_i = \Psi^t_S P^t_{S,i} - \Psi^t_B P^t_{B,i} - C^t_{bat,i}, \tag{2.25}$$

where $\mathcal{F}^t_i$ represents the cost function, while Ψ^t_B and Ψ^t_S denote the electricity buying and selling prices for the MG, respectively. Given the independent operation of the MG, it interacts with the main power grid rather than engaging in the cooperative framework of MMGs.

In the independent operation of the MG, day-ahead forecasted data is used to minimize operational costs over the dispatching period T. The objective function is given by:

$$\min_{P^t_{char,i},P^t_{dis,i},\alpha^t_{char,i},\alpha^t_{dis,i}} \mathcal{F}_i^T = \sum_{t=0}^{T} \mathcal{F}_i^t, \tag{2.26}$$

$$s.t = (1) - (7),$$

Equation (2.26) outlines the optimization objective of minimizing the operational cost for the independent operation of the MG and is formulated as a mixed integer linear programming (MILP) problem.

2.2.5 Cooperative Alliance framework of MMGs based on the cooperative game theory

This section presents a cooperative alliance framework for multiple MGs based on a cooperative game approach. During a uniform dispatch time, MGs may operate under varying conditions: one may have surplus energy, while another may face a power shortage. By joining this cooperative alliance, MGs can exchange power among themselves, allowing them to meet load demands more efficiently, reduce operational costs, and increase revenue through the cooperative framework. For MGs to participate in this alliance, the total collective profit generated by all participants must be greater than the benefits they would achieve individually. This condition is represented by the following relation:

$$\mathcal{F}(\{1\}) + \mathcal{F}(\{2\}) + \mathcal{F}(\{3\}) + \mathcal{F}(\{4\}) + ... + \mathcal{F}(\{n\}) > \mathcal{F}(\{N\}), \tag{2.27}$$

where $\mathcal{F}$ represents the cost function, and let $1,2,3,4...n$ denote the participants in the cooperative alliance framework. The objective function for the cooperative alliance framework of MMGs can then be expressed as follows:

$$\min \mathcal{F}_N^T = \sum_{i=1}^{n} \sum_{t=0}^{T} \mathcal{F}_i^t, \tag{2.28}$$

where n denotes the total number of participants, and $\mathcal{F}_N^T$ represents the cost of the cooperative alliance.

2.2.5.1 Shapely Value method

To ensure fair benefit distribution among all participants in the cooperative alliance framework, we used the Shapley value method from cooperative game theory. This approach allocates benefits based on each participant's marginal contribution within the alliance framework [94–96].

For the calculation of the revenue, the calculation formula is considered as follows:

$$\gamma(|\beta|) = \frac{(|\beta|-1)!(n-|\beta|)!}{n!}; \tag{2.29a}$$

$$\sigma_i = \sum_{\beta \varepsilon N} \gamma(|\beta|)[\sigma(\beta) - \sigma(\beta - \{i\})], \tag{2.29b}$$

where $\gamma(|\beta|)$ denotes a weighting factor, where $|\beta|$ denotes the number of participants in the subset β. The total number of members is denoted by n, while N represents the total number of subsets in the cooperative alliance framework that include the i-th MG. The benefit of the i-th MG is denoted by σ_i, and $\sigma(\beta)$ refers to the revenue of the subset β.

2.2.6 Simulation results and discussion

In this section, we examine a configuration of four interconnected MGs that exchange power and communicate with each other, as well as with the main grid, through an energy router. The MG transmission line has a power capacity of up to 400 kW, while the energy storage system offers a storage capacity of 100 kWh and operates at an efficiency of 95%. The energy cost factor is set at 0.3 RMB/kWh, with a maximum charging and discharging power of 60 kW across all MGs.

To address the optimal scheduling problem, we utilized software tools including MATLAB and the Gurobi Optimizer solver, implemented via the YALMIP platform, to determine the optimal solution. This study adopts an optimization interval of 0.5 hours within a one-day optimization cycle, spanning a 24-hour optimization horizon. For enhanced performance analysis, real-time PV data from a specific region in China is integrated into the cooperative alliance framework, aiding in maximizing revenue generation. Fig. 2.7 illustrates the PV generation data and load profiles for all the MGs for the typical consideration of a day. Table 2.1 represents the Time of Use (TOU) index pricing for the Chinese region, along with a constant on-grid electricity pricing.

To underscore the importance of this research, we analyzed two modes of MG operation: independent operation and the cooperative alliance framework. In independent operation,

Table 2.1: Time of use electricity price index

Operational Mode	Time/h	Cost of Electricity (RMB/kWh)
Grid electricity price	7-8, 11-13, 16-18	Flat: 0.8
	8-11, 13-16, 18-22	Peak: 1.34
	0-7, 22-24	Valley: 0.31
On-Grid electricity price	0-24	0.21

Table 2.2: Cost analysis for independent Operation and Cooperative alliance framework for MGs

Operational Mode/ cost analysis	MG_1	MG_2	MG_3	MG_4	Accumulative
Independent operation/ RMB	881.17	518.62	908.45	932.37	3240.61
Cooperative alliance/ RMB	745.19	425.42	879.47	895.76	2945.84

each MG aims to minimize its own operational costs without interacting with other MGs, though it trades energy directly with the main grid. In contrast, within the cooperative alliance framework, we applied cooperative game theory to establish an alliance focused on minimizing total operational costs. This approach facilitates energy trading among the MGs and with the main grid, enhancing overall revenue generation.

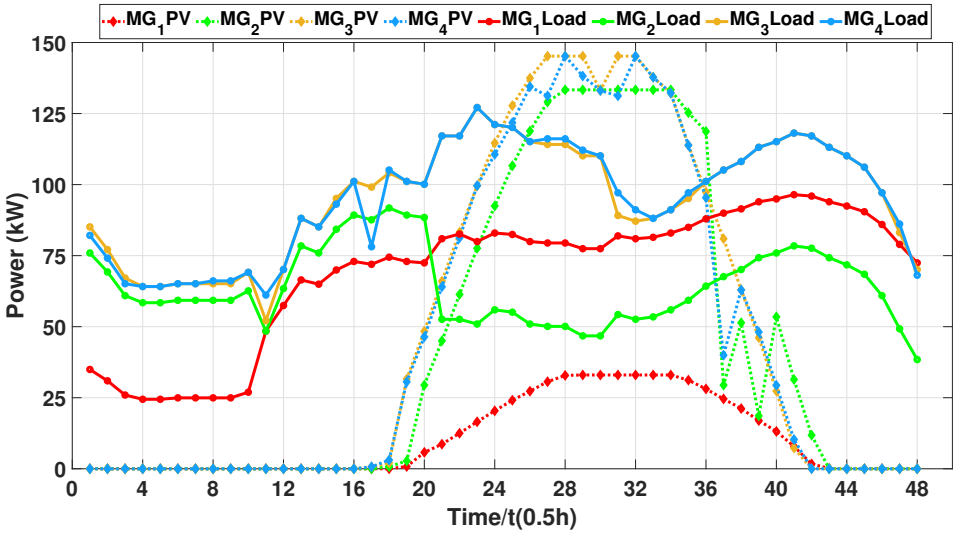

Figure 2.7: PV generation data and load profiles

Fig. 2.8 depicts the power distribution across each BESS along with the corresponding

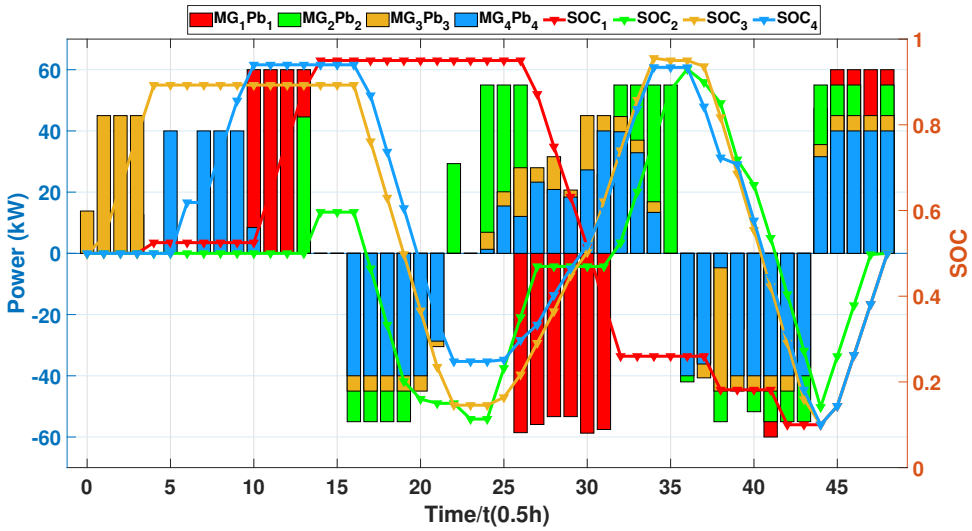

Figure 2.8: Optimal outcomes of BESS power and SOC

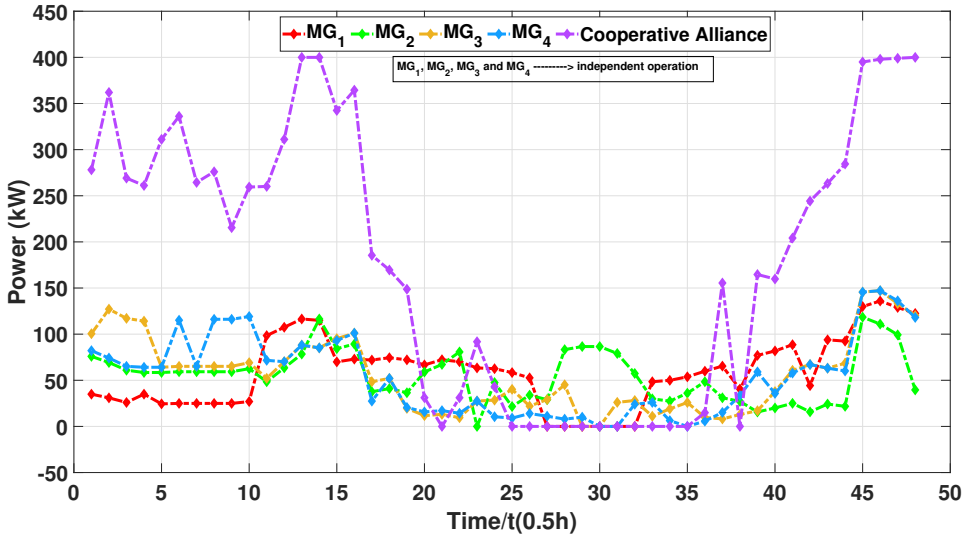

Figure 2.9: Independent and cooperative alliance operations of MGs

SOC levels based on the optimization results. This figure demonstrates that each MG in the cooperative alliance complies with SOC constraints while meeting the load requirements. Additionally, the cooperative alliance framework enables the MGs to support each other, during low demand periods, the BESS primarily charges, while at peak times, with higher energy prices, optimal scheduling facilitates BESS discharge, to support MG operations and reduce overall operational costs. Fig. 2.9 illustrates the power exchange between the MMGs and the main power grid under two operational modes: independent and cooperative alliance. From this figure, it is evident that, compared to the independent operations of all MGs, the cooperative alliance mode allows for better absorption of surplus energy during

periods of low load demand at lower prices. Additionally, optimizing the alliance reduces interactions with the main power grid during high PV production, as each MG operates independently of the main grid. Consequently, this proposed cooperative transactive alliance framework reduces the MMGs impact on the main power grid, increases revenue, and ensures fair profit distribution among the participants. To further demonstrate the advantages of the proposed study, Table 2.2 presents a numerical cost analysis for both modes of MG operation. This table shows that in the cooperative alliance mode, operational costs are notably lower due to the mutual coordination among all MGs, compared to the independent operation mode.

The MMGs are connected to the main power grid via an energy router, and a cooperative game-based Shapley value method is used to fairly distribute benefits among all participants. Optimization results show that the PV-based MG cooperative alliance improves power utilization through mutual support while also providing greater economic advantages.

2.3 Optimization of MMGs Energy Trading in Distribution Networks

As discussed in the previous section 2.2, the optimization of MMGs distribution networks faces several challenges due to the integration of RESs and load variations. These challenges include balancing supply and demand across the MGs, optimizing economic dispatch to minimize costs, and ensuring fair benefit distribution among the MGs [97–99]. In this section, we build upon the study presented in section 2.2 by introducing and analyzing another optimization methodology, the master-slave game approach. This proposed optimal control strategy plays a critical role in tackling both demand response management and energy trading challenges in distribution networks. Initially, the energy storage output and transaction status for each MG are determined through a single MG optimization strategy. These optimized results are then shared with the DSO, and a master-slave game model is developed, utilizing internal electricity prices and dispatchable energy as the decision-making strategies.

2.3.1 MMG energy trading system structure

The MMGs energy trading system proposed in this paper is depicted in Fig. 2.10, consisting of three main components: the power grid, the DSO, and the MGs. Each MG is equipped

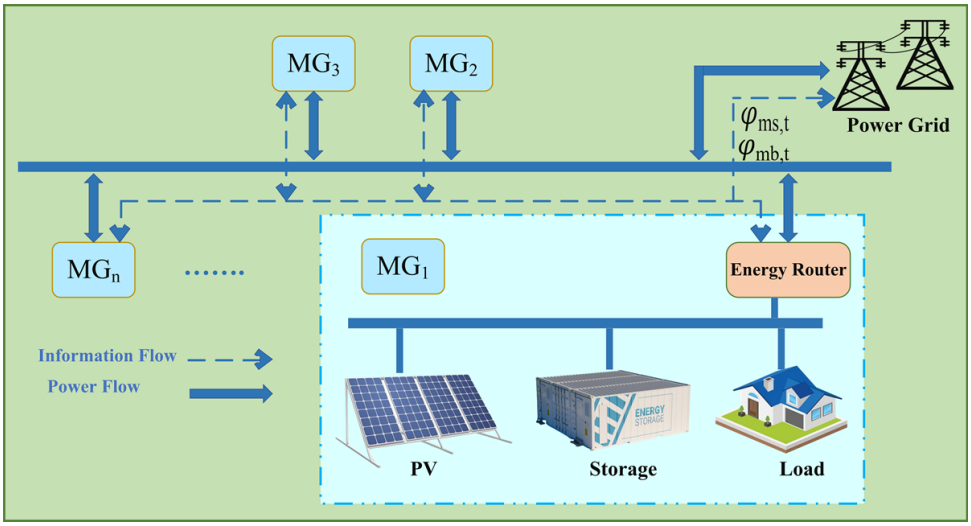

Figure 2.10: Energy trading model of MMGs

with its own independent energy management system, capable of optimizing the power output of each unit within the MG. The DSO enables the creation of a power market among the MGs by receiving and processing their interactive data. It is also responsible for setting the purchase and sale prices within the market and generating revenue from the price differences. In any scheduling period t, the purchase and sale price in the electricity market are denoted by $\phi_{mb,}$ and $\phi_{ms,t}$, respectively. Meanwhile, $\phi_{Db,t}$ and $\phi_{Ds,t}$ represent the electricity prices at which the DSO trades with the grid.

2.3.1.1 Master-slave game approach

In the game mode proposed in this paper, the DSO and the MG operate as independent stakeholders. Acting as the leader in the master-slave game, the DSO is primarily responsible for collecting data from the MG, establishing the power market, and optimizing its buying and selling price strategy to maximize its own profits. The MG, as the follower, responds to the DSO's pricing strategy by managing its distributed energy resources to minimize its operational costs. Thus, the DSO's pricing strategy must consider both its own objectives and the responses of the MG, capturing the master-slave game dynamics between these two entities [100–102].

In the proposed master-slave game model, the interaction is defined by the transaction volume between the MG and the DSO, with the DSO's pricing strategy influencing the MG's response decisions. Using day-ahead forecast data, the MG optimizes its energy storage scheduling to maximize operational benefits over a set timeframe, determining its role in electricity market transactions. In the DSO model, a master-slave-based energy

transaction model is established using information from the MG along with grid pricing, to optimize internal purchase and sale prices. This information is then relayed to the MG, guiding it to adjust its energy scheduling for the next period based on the DSO's decisions.

2.3.1.2 MG optimization model

1. **Distributed generator:** The operational cost function for a dispatchable distributed generator is formulated mathematically as follows:

$$C^t_{DG,i} = \alpha_1((P^t_{DG,i})^2 + \alpha_2((P^t_{DG,i}) + \alpha_3\delta; \tag{2.30}$$

$$0 \leq P^t_{DG,i} \leq P^{max}_{DG,i}, \tag{2.31}$$

where $C^t_{DG,i}$ denotes the operating cost of the distributed generator in MG i during dispatching time t, while $P^t_{DG,i}$ represents the output power of the distributed generator in i-th MG at the same dispatching time t. α_1, α_2, and α_3 correspond to the cost factors of the distributed generator, and δ is a binary variable.

2. **Energy storage system:** Define $E^t_{s,i}$ represents the remaining capacity of the energy storage system within the scheduling time t of the i_{th} MG. $P^t_{bat,i}$ represents the charge and discharge power of the energy storage system in the scheduling time t of i-th MG, when $P^t_{bat,i} > 0$, the energy storage system is in the charging state and the energy storage system is in the discharge state when $P^t_{bat,i} < 0$. The mathematical model of energy scheduling of the energy storage system is shown as follows:

$$\Delta P^t_{S,i}\Delta t = E^t_{S,i} - E^{t-1}_{S,i}. \tag{2.32}$$

The ESSs must define upper and lower limits for both capacity and charging/discharging power constraints. Furthermore, to ensure sustainable MG scheduling, the initial state of the energy storage system should be equal to its capacity at the end of the scheduling cycle. Consequently, the energy storage system must adhere to the following constraints:

$$\overline{E_{S,i}} \leq E^t_{S,i} \leq \underline{E_{S,i}}; \tag{2.33a}$$

$$\overline{P_{bat,i}} \leq P^t_{bat,i} \leq \underline{P_{bat,i}}; \tag{2.33b}$$

$$E^0_{S,i} = E^T_{S,i}. \tag{2.33c}$$

3. **PV and load:** Since photovoltaic power generation is a renewable energy source that does not rely on fossil fuels for MG energy trading, its generation costs are disregarded. Let $P_{PV,i} = \{P^1_{PV,i}, P^2_{PV,i}, P^3_{PV,i}, P^4_{PV,i}.....P^T_{PV,i}\}$ denote the set of PV power generation values within the i-th MG. Similarly, let $P_{L,i} = \{P^1_{L,i}, P^2_{L,i}, P^3_{L,i}, P^4_{L,i}.....P^T_{L,i}\}$ represent the set of load demand within the i-th MG.

2.3.1.3 Optimal scheduling objectives of MG

In the MMGs energy transaction model proposed in this section, the PV and distributed generators of an individual MG prioritize meeting the local load demand. When the generated energy exceeds local load requirements, the surplus is either stored or sold to DSO through power lines. The energy transaction volume between i-th MG and the DSO, denoted as $P^t_{net,i}$, is given by:

$$P^t_{net,i} = P^t_{DG,i} + P^t_{PV,i} - P^t_{bat,i} - P^t_{PL,i}, \tag{2.34}$$

where $P^t_{net,i}$ represents the energy transaction volume between i-th MG and DSO during dispatch time t, when $P^t_{net,i} > 0$ then i-th MG sells electricity to DSO and i-th MG purchase electricity from DSO when $P^t_{net,i} < 0$.

Within the same scheduling time in each scheduling time interval, only one transaction state is allowed—either a power purchase state or a power sale state. Therefore, auxiliary variables are introduced to impose the following constraints on $P^t_{net,i}$, as follows:

$$P^t_{net,i} = P^t_{S,i} - P^t_{b,i}; \tag{2.35a}$$

$$0 \le P^t_{S,i} \le D^t_{S,i}\overline{P^t_{net,i}}; \tag{2.35b}$$

$$0 \le P^t_{b,i} \le D^t_{b,i}\overline{P^t_{net,i}}; \tag{2.35c}$$

$$D^t_{B,i} + D^t_{S,i} \le 1, \tag{2.35d}$$

where $P^t_{s,i}$ and $P^t_{b,i}$ denote the electricity purchased and sold, respectively, while $\overline{P_{net,i}}$ represents the maximum power that can be transacted with the grid. The binary variable $D^t_{b/s,i}$ is used to control the direction of power flow. For an MG, its operational benefits primarily consist of economic gains from local electricity consumption, energy transactions with the DSO, and the costs associated with distributed generation within the MG. Its

mathematical expression is as follows:

$$f_{m,t} = \ln(1 + P^t_{L,i})^{k_i} + \hat{\varphi}^t_{mS} P^t_{S,i} - \hat{\varphi}^t_{mb} P^t_{b,i} - C^t_{DG,i}, \tag{2.36}$$

where $\ln(1 + P^t_{L,i})^{k_i}$ represents the benefits from the internal load within MG i, where k_i denotes the income coefficients. Additionally, $\hat{\varphi}^t_{mS}$ indicates the forecasted selling price of electricity in the i-th MG at time t, and $\hat{\varphi}^t_{mb}$ represents the anticipated power purchase for the MG within the dispatch period t.

In the MG optimization phase, utilizing day-ahead forecast data, the aim is to maximize operational benefits over the scheduling period T. The objective function is formulated as follows:

$$\max_{P^t_{DG,i}, P^t_{bat,i}, D^t_{S,i}, D^t_{b,i}} f_m = \sum_{t=0}^{t+k\Delta t} f_{m,t}, \tag{2.37}$$
$$s.t = (2.30) - (2.36),$$

where in Eq. 2.37, the optimization goal is for the MG to maximize its self-benefit during the time period $K\Delta t$. The allocation of output for each unit within the MG is framed as a mixed-integer quadratic programming problem. This optimization objective function is solved using the Gurobi optimizer solver within MATLAB software. Through MG optimization, the energy transaction is preliminarily optimized, and the decision variable $D^t_{S,i}$, $D^t_{b,i}$ and $\Delta P^t_{S,i}$ are output to DSO, to determine the role of MG in the DSO optimization stage and energy storage scheduling.

2.3.2 Distribution system optimization model

The DSO collects information on transaction statuses, energy storage optimization results, photovoltaic generation, and load consumption for each MG across different scheduling periods to create an intra-MG power market. Within this established market for a group of MGs, the DSO facilitates energy transmission among the MGs and reduces energy exchanges with the main grid by setting purchase and sale prices. The operating income is generated from the difference between electricity buying and selling prices in the market.

1. **DSO objective function:** By gathering data from all MGs, the DSO designates roles for power buyers and sellers within the power market, then calculates the energy demand E^t_S and energy surplus E^t_b for the market during a scheduling period t. The

expression is as follows:

$$E_S^t = \sum_{i \in I, D_{b,i}^t} P_{b,i}^t; \tag{2.38a}$$

$$E_b^t = \sum_{i \in I, D_{S,i}^t} P_{S,i}^t, \tag{2.38b}$$

where I represents the set of MGs. To maintain the power balance constraints for the entire MG group, the DSO must also conduct energy transactions with the main power grid. During any given scheduling period t, the DSO's internal energy can only be in one state: either an energy demand or an energy surplus. To model this, an auxiliary state variable, ω is introduced, as follows:

$$\omega = 0, \;\; E_S^t \geq E_b^t; \tag{2.39a}$$

$$\omega = 1, \;\; E_S^t \leq E_b^t, \tag{2.39b}$$

From Eqs. (2.39a), and (2.39b) when ω is 0, the energy sold by the DSO exceeds the energy purchased, indicating that the distribution network draws energy from the grid to meet the MG group's demand. On the other hand, when ω is 1, the DSO purchases more energy than it sells, causing the distribution network to supply surplus energy to the grid. To ensure rational transactions, the market price must comply with the following constraints:

$$\varphi_{DS}^t \leq \varphi_{mS}^t \leq \varphi_{mb}^t \leq \varphi_{Db}^t. \tag{2.40}$$

The objective function representing the DSO's operational benefit can be written as:

$$\max_{\varphi_{mS}^t, \varphi_{mb}^t} f_{D,t} = \varphi_{mS}^t E_b^t - \varphi_{mb}^t E_S^t + \varphi_{Db}^t (E_b^t - E_S^t)(1-\omega) + \varphi_{DS}^t (E_b^t - E_S^t)(\omega), \tag{2.41}$$

$$s.t = (2.39a) - (2.40).$$

2. **Master-slave game model:** In the master-slave game outlined in this subsection, the DSO functions as the leader, and the MG acts as the follower. The leader makes decisions driven by its own objectives, while the follower's decisions are shaped by the leader's actions [7].

   The MG and DSO optimize their respective benefits through strategic decision-

making. Therefore, a feasible solution to this game is the Nash equilibrium, where the leader sets the optimal purchase price, accounting for the follower's best response, and the follower determines the optimal operational benefit. In this strategy, neither the leader nor the follower can unilaterally alter their approach to gain a higher benefit. If there is a Nash equilibrium solution in game L, then there is a unique set of strategies $\{P^t_{DG,i},^*, \varphi^t_{mS}{}^*, \varphi^t_{mb}{}^*\}$ that satisfy the following inequalities:

$$f^t_m(P^t_{DG,i},^*, \varphi^t_{mS}{}^*, \varphi^t_{mb}{}^*) \geq f^t_m(P^t_{DG,i},^*, P^t_{DG,-i},^*, \varphi^t_{mS}{}^*, \varphi^t_{mb}{}^*), \tag{2.42}$$

$$\forall i \in I \ \ \forall P^t_{DG,i} \in P^t_{DG,i}.$$

$$f^t_D(P^t_{DG,i},^*, \pi_{mS,t}{}^*, \pi_{mb,t}{}^*) \geq f^t_D(P^t_{DG,i},^*, \Pi_{mS,t}, \Pi_{mb,t}), \tag{2.43}$$

$$\forall \Pi_{mS,t} \in \pi_{mS,t} \ \ \forall \Pi_{mb,t} \in \pi_{mb,t}.$$

where $P^t_{DG,i}$ denotes the set of optimal policies for all followers, while $P^t_{DG/i}$ represents the optimal policy set for all followers except follower i.

3. **Master-slave game solving:** Based on the above content, the optimization decision variables for the MG during the game stage are the generator power $P^t_{DG,i}$, while the optimization variables for the DSO are the market selling price φ^t_{mS} and the market purchasing price φ^t_{mb}. Given that there are various transaction states in the game stage, the MG is categorized and discussed accordingly.

$$P^t_{net,i} = P^t_{DG,i} + P^t_{PV,i} - P^t_{bat,i} - P^t_{PL,i} \leq 0, \ D^t_{b,i} = 1; \tag{2.44a}$$
$$P^t_{net,i} = P^t_{DG,i} + P^t_{PV,i} - P^t_{bat,i} - P^t_{PL,i} \geq 0, \ D^t_{S,i} = 1, \tag{2.44b}$$

Thus, the benefit function of the MG can be expressed as follows:

$$f^t_m = k_i \ln(1 + P^t_{L,i})^{k_i} + \hat{\varphi}^t_{mb}(P^t_{DG,i} + P^t_{PV,i} - P^t_{bat,i} - P^t_{PL,i}) - C^t_{DG,i}, \ D^t_{b,i} = 1; \tag{2.45a}$$

$$f^t_m = k_i \ln(1 + P^t_{L,i})^{k_i} + \hat{\varphi}^t_{mS}(P^t_{DG,i} + P^t_{PV,i} - P^t_{bat,i} - P^t_{PL,i}) - C^t_{DG,i}, \ D^t_{S,i} = 1 \tag{2.45b}$$

By taking the first partial derivative with respect to $P^t_{DG,i}$, we have

$$P^t_{DG,i} = \frac{\varphi^t_{mb} - \alpha_2}{2\alpha_1},\ D^t_{b,i} = 1; \tag{2.46a}$$

$$P^t_{DG,i} = \frac{\varphi^t_{mS} - \alpha_2}{2\alpha_1},\ D^t_{S,i} = 1. \tag{2.46b}$$

Now by considering the working range of the generator set under different working conditions:

$$0 \leq P^t_{DG,i} \leq min(P^t_{bat,i} + P^t_{PL,i} - P^t_{PV,i} + \overline{P^t_{DG,i}}),\ D^t_{b,i} = 1; \tag{2.47a}$$

$$max(P^t_{bat,i} + P^t_{PL,i} - P^t_{PV,i}, 0) \leq P^t_{DG,i} \leq \overline{P^t_{DG,i}}. \tag{2.47b}$$

By following the steps mentioned above, we can determine the values of ${E^t_S}^*$, and ${E^t_b}^*$, as well as the optimal generator power values corresponding to different purchase prices.

Table 2.3: TOU electricity price

Operational Mode	**Time/h**	**Cost of Electricity (RMB/kWh)**
Purchasing price	7-8, 11-13, 16-18	Flat: 0.65
	8-11, 13-16, 18-22	Peak: 1.25
	0-7, 22-24	Valley: 0.35
Feed-in tariff	0-24	0.30

Table 2.4: Analysis of the benefit of MGs

Operational Mode/ cost analysis	**MG_1**	**MG_2**	**MG_3**	**DSO benefit**
First operation/ RMB	5150.6.17	4637.4	5872.1	-
Second operation/ RMB	5197.5	4622.5	5897.7	242.4

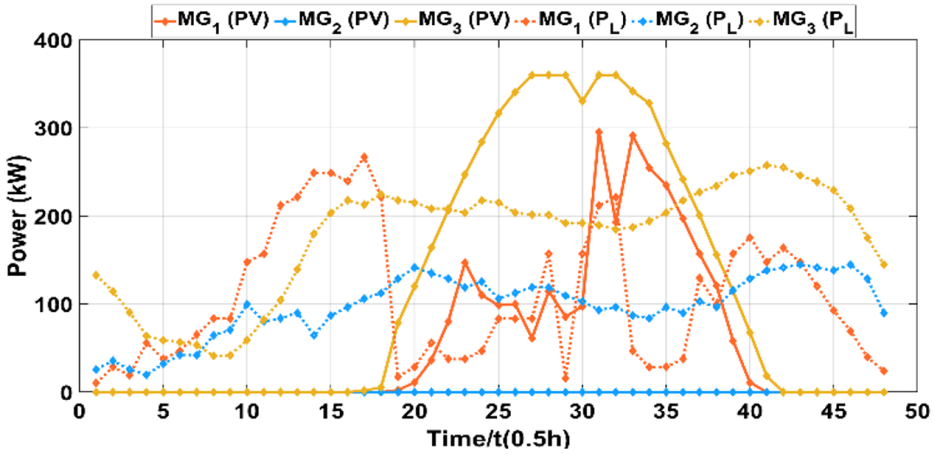

Figure 2.11: The power generation data for all the PV systems and the load profiles

2.3.3 Analysis of Simulation results and discussion

To explain the simulation results for the MG group power market developed in this study, a distribution network with three MGs is considered, where energy trading occurs through the power market established by the DSO. For the parameter settings, the MMGs energy trading system proposed in this paper is simulated and analyzed using a typical region in China as an example. Fig. 2.11 shows the photovoltaic power generation data and the load profile for a selected typical day in the MG. The MG transmission line has a maximum power capacity of 550 kW, with a generator output limit of 110 kW. The energy storage system is rated at 100 kWh, with a maximum charge and discharge power of 50 kW, and a load benefit factor of 60. The cost coefficients for the distributed generator, α_1, α_2, and α_3, are set to 0.015, 0.35, and 0.75, respectively. The optimization step is set at 0.5 hours, with an optimization period of one day and a rolling horizon of 8 hours for the MG optimization. Based on the actual electricity prices in the typical region, the power grid selling price is categorized into three levels: peak, shoulder, and valley times. The on-grid electricity price is a constant value, while the TOU tariff is provided in Table.2.3.

The comparison between the electricity purchase and sale prices in the MG group electricity market and the grid electricity price set by the DSO, under the internal electricity price optimization strategy, is shown in Fig. 2.12. This figure indicates that during the periods from 0:00 to 9:00 and 20:00 to 24:00, when photovoltaic power generation is limited and load demand is relatively high, the MG is mostly in a power-purchasing state. As a result, the internal electricity price closely aligns with the grid electricity price, preventing the DSO from adjusting the internal price or incentivizing MGs to engage in power market transactions. However, from 9:00 to 20:00, when MGs generate surplus

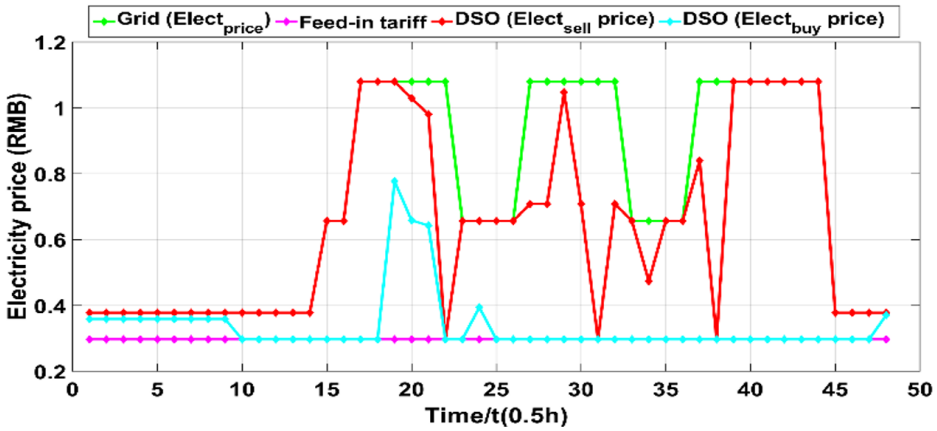

Figure 2.12: Outcomes of optimizing the internal electricity price

energy due to high photovoltaic output, they participate in power market transactions. During this period, the DSO encourages such transactions by raising the electricity purchase price and lowering the sale price. This strategy not only reduces the operating costs for MGs but also allows the DSO to earn operational profits from the price differentials.

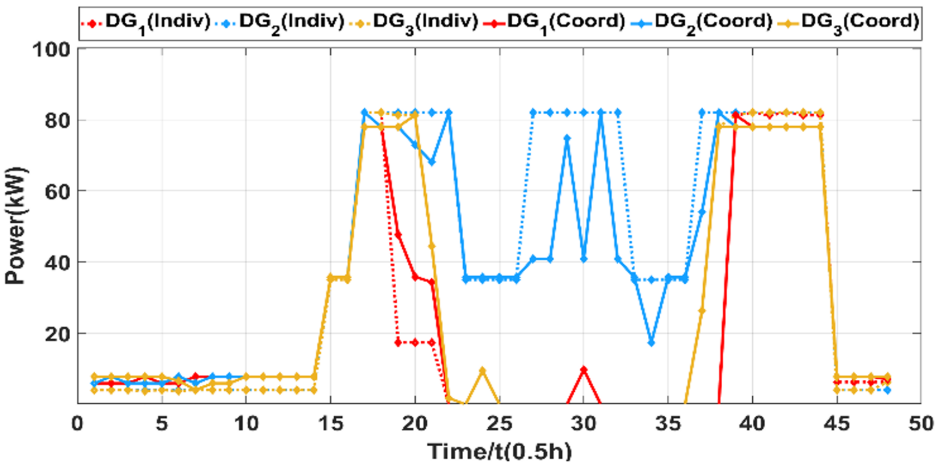

Figure 2.13: Optimization of the distributed generator

Table.2.4 presents the operating benefits of the MG under different strategies. By combining Table.2.4 with Fig. 2.13, it is evident that under strategy 2, the output of the distributed generators within the MG is optimized. Additionally, as the MG participates in internal power market transactions, the benefits are significantly improved, and the operating costs are reduced compared to direct interaction with the grid during certain periods.

2.4 Robust optimization-based energy management for the optimal economic dispatch

In prior sections, an optimal control methodology was proposed and examined for residential building-based nanogrids, MMGs, and DSO-based transactional energy frameworks, enabling end-users to enhance demand response management and reduce overall costs, while sharing equal benefits among them.

The economic dispatch (ED) problem in larger power systems remains a key focus as it aims to minimize generation costs while satisfying demand and adhering to generation unit constraints. However, the increasing integration of RESs, like photovoltaic (PV) systems, introduces unprecedented challenges due to their inherent variability and uncertainty, especially when combined with fluctuations in loads [103, 104]. These challenges can reduce the effectiveness of economic dispatch solutions and compromise the power system's reliability. This section illustrates a two stage robust optimization (TSRO) based energy management methodology designed to achieve optimal economical dispatch. The objective function aims to minimize the overall generation cost and mitigate the BESS aging cost through economically optimized battery scheduling while addressing the uncertainties of the system. An iterative column and constraint generation (C&CG) algorithm has been used to solve the TSRO. A customized IEEE-9 bus system is utilized as a case study to analyze the effectiveness of the proposed robust optimal methodology. Additionally, a comparison has been made by considering the cases with and without BESS, to demonstrate the superiority of the proposed methodology in reducing the generation costs.

A column and constraint generation (C&CG) algorithm, an iterative algorithm the problem into the dual-stage, namely as master and subproblem for each scenario [105, 106] has been chosen, to solve the proposed TSRO approach to deploy the economic dispatch operation. Additionally, a comparison of scenarios with and without BESS installation is conducted to evaluate the superiority of the proposed robust optimal control methodology and to analyze the economic benefits and their impacts on the power system.

2.4.1 Two-stage robust optimization problem

This section outlines the TSRO methodology. In this TSRO framework, the second stage problem addresses the decision-making based on the decision variables determined by the master problem. Set points for all the resources within the customized IEEE-9 bus

system are obtained through the quadratic constraint linear programming (QCLP). A 15-minute real-time extended framework is used for the optimization problem. The primary objectives of the TSRO approach are to minimize overall generation costs and reduce the daily charging and discharging cycling of BESS, thereby lowering battery aging costs, while accounting for the economic scheduling of BESS amidst system uncertainties.

Then the general formulation of the proposed TSRO can be described in the form of:

$$\begin{aligned} \min_{v} c^T v + \max_{u \in \mu} \min_{\gamma \in F(\gamma, u)} q^T \gamma; \\ s.t. Bv \leq n; \\ F(v,u) = \{A\gamma \leq h - Ev - Wu\}, \end{aligned} \tag{2.48}$$

where v and γ denote the first- and second-stage decision variables, respectively, with constraints relevant to v specified by the above formulations (specified by eq. (1)). Additionally, the constraints associated with the γ and u are linked, where A, B, n h, E and W are the corresponding constants matrices. The first stage seeks to minimize (min) the first-stage costs by optimizing the decision variables set as v. The sub-problem (second-stage) is based on "max-min" to address the uncertain variables u within the polyhedral uncertainty set μ to balance the uncertainty level and to minimize the auxiliary storage costs ensuring robustness in the second stage. The three different types of variables in Eq. 2.48 are classified as follows: v denotes the decisiveness variables in the first stage problem, γ denotes the decisiveness variables in the second stage, and μ is polyhedral uncertainty set based on uncertainty variables u.

2.4.1.1 Column and Constraint generation algorithm

The proposed two-stage robust C&CG algorithm is illustrated as follows:

- set the lower limit as lower bound (LB)=$-\infty$ and upper limit as upper bound (UB)=$+\infty$

- first stage problem (master-problem) perchance solved by successive steps;

$$\begin{gathered} \min_{v} c^T v + \sigma \\ s.t.\ Bv \leq n \\ \sigma \leq q^T \gamma^l \ \ where\ \ l = 1,2... \\ Ev + A\gamma^l \leq h - Mu_l \ \ where\ \ l = 1,2... \\ and\ \forall \leq d\ \ \sigma \in R \end{gathered} \tag{2.49}$$

- derive the best possible solution by accounting for the above Eq. 2.49 constraints and updating the LB.

- solve the second stage problem (max-min problem) according to the successive Eq. 2.50 and update the UB.

$$Q(k) = \max_{u \in \mu} \min_{\gamma} q^T \gamma :\ A\gamma \leq h - Ev - Wu \tag{2.50}$$

- if UB-LB $\leq \varepsilon$, return to v^*_{d+1} and terminate. if not then continue,
  (a) if $Q(v^*_{d+1}) < +\infty$, evaluate the variables γ^{d+1} and updates the constraint as follows;

$$\begin{gathered} \sigma \leq q^T v^{d+1} \\ Ev + A\gamma^{d+1} \leq h - Mu^*_{d+1} \end{gathered} \tag{2.51}$$

  the above constraints should be fulfilled to update the master problem.
  (b) if $Q(v^*_{d+1}) = +\infty$ evaluate the variables γ^{d+1} and update the following constraints only;

$$Ev + A\gamma^{d+1} \leq h - Mu^*_{d+1} \tag{2.52}$$

$$\min_{v}(C_{gi}(t)\Delta t + C_b * n_b) + \max_{P_{pv},\, P_{load}} \min_{\gamma \in F(\gamma, u)} q^T \gamma \tag{2.53}$$

Eq. 2.53, represents the two-stage optimization problem formulation according to our proposed objectives. It can be observed that overall generation cost and battery aging cost are minimized by considering the TSRO-based EMS approach through the first-stage decision variables set v and second-stage decision variables set γ while the P_{PV} and P_{load} are the uncertainties variables of the system. Fig. 2.14 depicts the flow chart of the proposed TSRO approach, based on the C&CG algorithm.

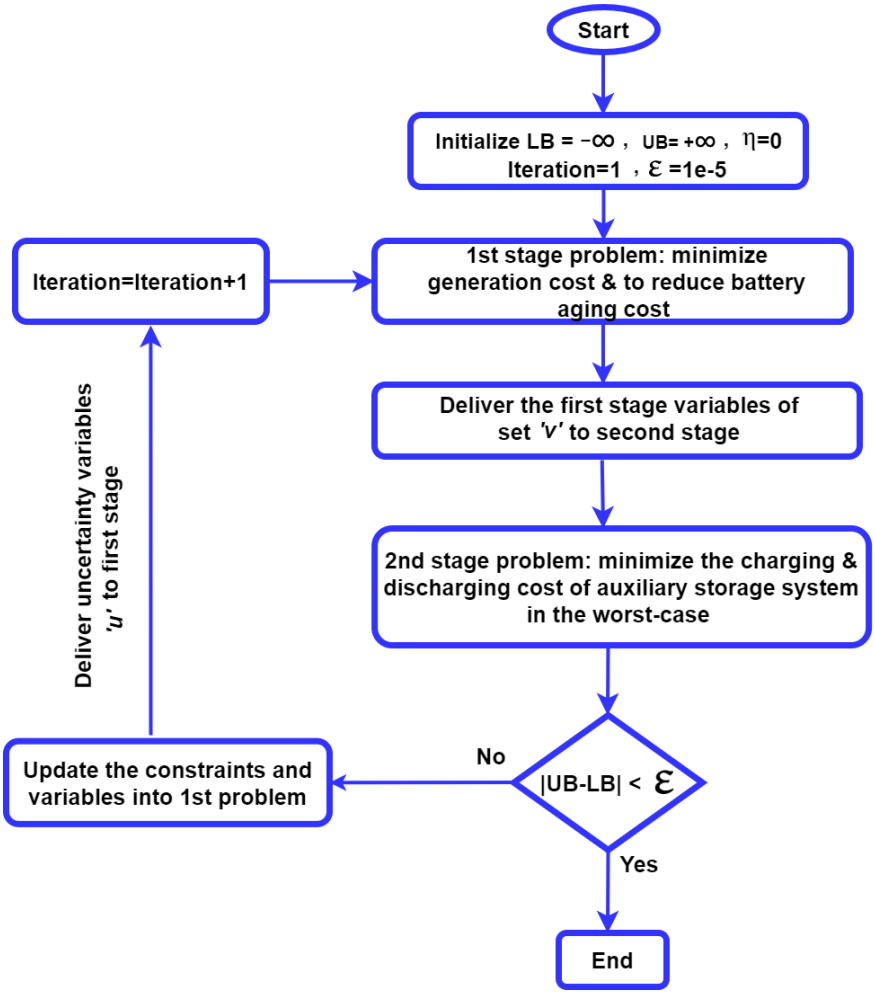

Figure 2.14: Flow chart of TSRO approach, based on the C&CG algorithm

2.4.1.2 First stage/Master problem formulation

$$\min\Big(\sum_{t=1,i=1}^{T,N}(C_{gi}(t)\Delta t)+C_b*n_b\Big)+\sigma, \tag{2.54}$$

where $C_{gi}(t)$ represents the generation cost, Δt denotes the time step length in hours (Δt= 0.25h), $T=96$ indicates the number of sampling points in a day, and N is the number of generators. The parameter C_b is the battery aging cost, based on the battery's rated capacity, while n_b denotes the daily number of battery cycles, and σ is an auxiliary decision variable determined in the second stage. Accordingly, $C_{gi}(t)$ can be expressed as follows:

$$C_{gi}(t)=a_i+b_i(P_{gi})(t)+c_i(P_{gi})^2(t);\ \text{where}\ (i=1,2,3...N) \tag{2.55}$$

where $a_i>0$, $b_i>0$, and $c_i>0$ are the coefficients of the thermal generation (based on

natural gas) cost function.

The expression for calculating n_b can be formulated as follows:

$$n_b = \frac{\sum_{t=1}^{T} (P_b^{disch}(t)\Delta t)}{0.8DOD}, \tag{2.56}$$

where P_b^{disch} denotes the discharging power of BESS, and DOD refers to the Depth Of Discharge.

2.4.1.3 Generation constraints

The constraints presented in Eqs. (2.57a) to (2.57c) illustrate the ramping up/down constraints of the thermal generating units powered by natural gas, as follows:

$$P_{gi,max} \geq P_{gi} \geq P_{gi,min}\,; \tag{2.57a}$$

$$P_{gi}(t+1) - P_{gi}(t) \leq P_{gi,up} \text{ where } (i = 1,2,3...N); \tag{2.57b}$$

$$P_{gi}(t+1) - P_{gi}(t) \geq P_{gi,down} \text{ where } (i = 1,2,3...N). \tag{2.57c}$$

2.4.1.4 Battery power and SOC constraints

The appropriate constraints for battery power output, including its maximum supplying and discharging capacity, as well as the SOC constraints, are outlined as follows:

$$E_b(t) = E_b(t-1) - P_b^{+}(t-1)\Delta t.\eta\,; \tag{2.58a}$$

$$E_b(t) = E_b(t-1) - P_b^{-}(t-1)\Delta t/\eta\,; \tag{2.58b}$$

$$P_b = \zeta P_b^{+} + (1-\zeta)P_b^{-}. \tag{2.58c}$$

where E_b denotes the battery SOC, P_b^{+} and P_b^{-} represent the discharging and charging power values of the battery, respectively. Additionally, η indicates the efficiency of the

battery, while ζ is the state variable of the battery, with $\zeta \in [0,1]$.

$$E_{b,max} \geq E_b(t) \geq E_{b,min}; \tag{2.59a}$$

$$P_{b,max} \geq P_b(t) \geq P_{b,min}; \tag{2.59b}$$

$$E_{max} = 0.9E_{rated}; \tag{2.59c}$$

$$E_{min} = 0.1E_{rated}. \tag{2.59d}$$

where E_{rated} denotes the battery rated capacity, $E_{b,max}$ and $E_{b,min}$ are the uppermost (maximum) and lowermost (minimum) SOC conditions. If P_b is positive, it means the battery is supplying the power (discharging mode) and if P_b has a negative value, the battery is storing the power (charging mode). To consider the balance between the charging and discharging operations of the battery, another constraint is considered in the following manner:

$$E_b(0) = E_b(T), \tag{2.60}$$

where T represents a time interval typically for one day.

Now in order to get the value of σ, the following relationship is used:

$$\sigma \geq q^T.\gamma \ \ where\ \sigma \geq 0. \tag{2.61}$$

2.4.1.5 Nodal power balance constraints

The nodal power balance equality constraints are represented as follows:

$$P_{gi} - P_{di} = V_i \sum_{k=1}^{n} V_k(G_{ik}Cos\theta_{ik} + B_{ik}Sin\theta_{ik}); \tag{2.62}$$

$$Q_{gi} - Q_{di} = V_i \sum_{k=1}^{n} V_k(G_{ik}Sin\theta_{ik} - B_{ik}Cos\theta_{ik}), \tag{2.63}$$

where $i = 1,2,3....n$, Y_{ik}=$G_{ik} + jB_{ik}$ is the (i,k) entry of the bus admittance matrix (Y), while G represents the conductance and B indicates the susceptance of the bus admittance matrix and $\theta_{ik} = \theta_i - \theta_k$.

2.4.1.6 Security constraints

To ensure security, the following constraints regarding the voltage level at load buses and the line flow constraints are taken into account, as follows:

$$V_{i,min} \leq V_i \leq V_{i,max}; \tag{2.64}$$

and,

$$|P_{ik}| \leq P_{ik,max}; \tag{2.65a}$$
$$|Q_{ik}| \leq Q_{ik,max}. \tag{2.65b}$$

To address the master problem, a Gurobi optimizer solver was utilized. For this purpose, a Jabr relaxation approach was employed [4], to achieve the second-order cone relaxation by introducing auxiliary variables defined as, $C_{ik} = |V_i||V_k|Cos(\theta_{ik})$, $S_{ik} = |V_i||V_k|Sin(\theta_{ik})$, $V_i^{(2)} = |V_i|^2$ and $V_k{}^{(2)}$=$|V_k|^2$. The Jabr relaxation approach helps to remove the non-convex problems of sine and cosine and assists in adding the rotating cone constraints for the optimal power flow (OPF) solution. Thus Eqs. 2.62 and . 2.63 becomes:

$$P_{ik} = G_{ii}||V_i|^2 + G_{ik}C_{ik} + B_{ik}S_{ik}; \tag{2.66a}$$
$$Q_{ik} = B_{ii}||V_i|^2 - B_{ik}C_{ik} + G_{ik}S_{ik}; \tag{2.66b}$$
$$C_{ik}^2 + S_{ik}^2 \leq V_i{}^{(2)}.V_k{}^{(2)} \text{ (for every branch } ik). \tag{2.66c}$$

where C_{ik} and S_{ik} are the auxiliary variables, utilized in the Jabr relaxation approach to address the non-convex issues associated with sine and cosine in Eq. (2.66c).

2.4.1.7 Second stage/Sub-problem

After solving the first-stage problem, the decision variable values obtained are utilized in the second-stage (sub-problem). The objective of the second-stage problem is to manage the uncertainties in the system based on the results from the first-stage problem ensuring the system's robustness. The sub-problem can be expressed, as follows:

$$\max_{u \in \mu} \min_{\phi} q^T |\phi|. \tag{2.67}$$

The polyhedral uncertainty set considered is based on the uncertainties associated with PV generation and load variations, and it can be expressed as follows:

$$\mu = \{u_i | \bar{u_i} \geq u_i \geq u_i, ||u||_1 \leq \Gamma\} \text{ where } (i = 1,2,3...); \tag{2.68}$$

$$s.t.\ \phi_{\boldsymbol{u}} \in \mu = u - P^*_{gi\in\Gamma} - P^*_b,$$

where $||u||_1$ denotes the first norm of the uncertainty set, while 'Γ' represents the robustness factor in Eq. (2.68).

2.4.1.8 Linearization

The absolute value in Eq. 2.67 is nonlinear, making it essential to linearize the absolute value of ϕ using linear programming through decomposition to solve the second-stage optimization problem, as follows:

$$\max_{u\in\mu} \min_{\gamma} q^T \gamma; \tag{2.69a}$$

$$\gamma \geq \phi \ and \ \gamma \geq -\phi. \tag{2.69b}$$

2.4.1.9 KKT duality problem

To address the duality problem, the KKT duality theory is employed to solve the max-min problem as follows:

$$\min(-q^T \gamma); \tag{2.70a}$$

$$\gamma \geq \phi \ and \ \gamma \geq -\phi. \tag{2.70b}$$

The matrix A, which is the parametric matrix of decision variables γ, is involved in solving the problem, as follows:

$$A^T \alpha \leq q, \tag{2.71}$$

where α is a duality transformation parameter.

$$(\gamma_i - \phi).\alpha_i = 0 \text{ where } (i = 1,2,3...); \tag{2.72a}$$

$$(q - A^T\alpha).\gamma_i = 0 \text{ where } (i = 1,2,3...); \tag{2.72b}$$

$$(\gamma_i) \geq 0 \textit{ and } (\alpha_i) \geq 0 \text{ where } (i = 1,2,3...). \tag{2.72c}$$

Table 2.5: Parametric data about generators and battery

Sources	Parameters	Values
G_1	$P_{g1,max}$	247.5 MW
	$P_{g1,min}$	100 MW
	$P_{g1,up}(ramp)$	49.5 MW/min
	$P_{g1,down}(ramp)$	-49.5 MW/min
G_2	$P_{g2,max}$	192 MW
	$P_{g2,min}$	80 MW
	$P_{g2,up}(ramp)$	38.4 MW/min
	$P_{g2,down}(ramp)$	-38.4 MW/min
Battery	$P_{b,max}$	150 MW
	$P_{b,min}$	-150 MW

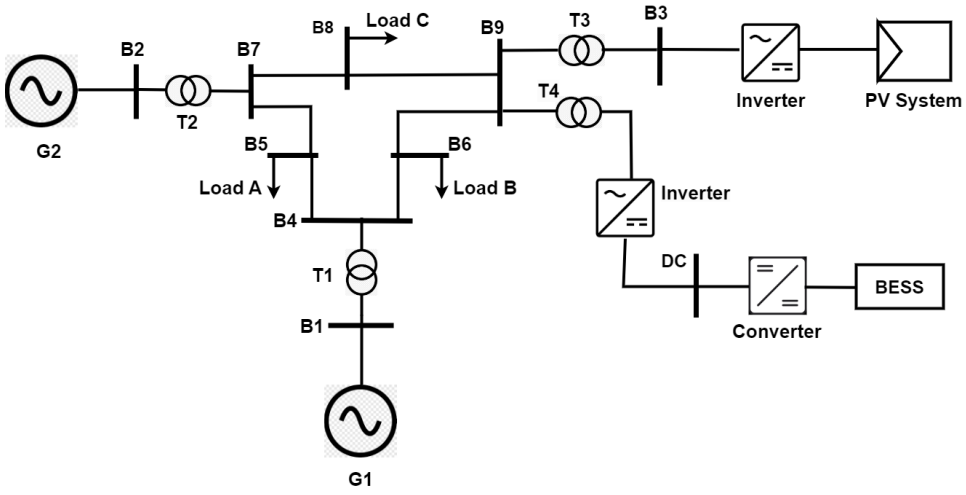

Figure 2.15: Customized IEEE-9 bus power system with PV and BESS

2.4.2 Analysis of simulation results and discussion

The effectiveness of the proposed TSRO approach is evaluated on the customized IEEE-9 bus system to assess its broader performance, however, this methodology is also applicable to islanded MG models. The customized model under study includes two synchronous generators, G1 and G2, connected to buses B1 and B2, respectively, as well as a PV system connected to B3. The system comprises nine AC buses (B1 to B9), three loads (Load A, Load B, and Load C), four transformers, and a DC bus that links the BESS module to B9 through an inverter, positioned close to the PV system, as shown in Fig. 2.15. The PV system's rated capacity is set at 85 MW. The proposed TSRO approach is solved using the MATPOWER toolbox, and Gurobi optimization solver, implemented through the YALMIP platform to achieve optimal economic dispatch results. In this study, we assume that natural gas is utilized for power generation in the thermal generating units (G1 and G2). Table 2.5 shows the parametric data about the thermal generating units and the BESS.

The performance of the proposed methodology is analyzed starting from the first stage problem of the TSRO, focusing on the EMS operation within the customized IEEE-9 bus system. A real-time 15-minute time interval is applied to determine the optimal solution. The first-stage problem involves a mathematical model that considers the system's generation, BESS, and the battery's cycle count in relation to the depth of discharge constraints. A polyhedral uncertainty set denoted by μ is used, to account for the uncertainty in the variables P_{pv} and P_{load}. The first-stage problem sends dispatch results for the thermal generating units and battery, represented by the decision variables (P_g^* and P_b^* within set v), to the second stage. The second-stage problem is constructed based on the outcomes of the first stage, integrating the polyhedral uncertainty set, and an additional auxiliary variable (ϕ) to address the level of uncertainties, thereby ensuring the systems's robustness.

Fig. 2.16 presents the bar graphs illustrating each of the three individual loads, the net load, and the active power output of the PV generation in MW. Fig. 2.17 shows the total active power generated by thermal generating units (G1 and G2), alongside the battery output power, as well as the total load and PV generation, all measured in megawatts (MW). From Fig. 2.17, it is evident that between 5:25 AM to 6:45 PM, during periods of high PV power generation, the TSRO approach provides an optimal energy management solution to meet load demands. This approach prioritizes power supply more from PV and partially from the BESS, reducing the dependency on thermal generators (G1 and G2) within this timeframe (5:25 AM to 6:45 PM). From 6:45 PM to 4:45 AM, when PV power production ceases, the TSRO-based EMS methodology efficiently schedules BESS

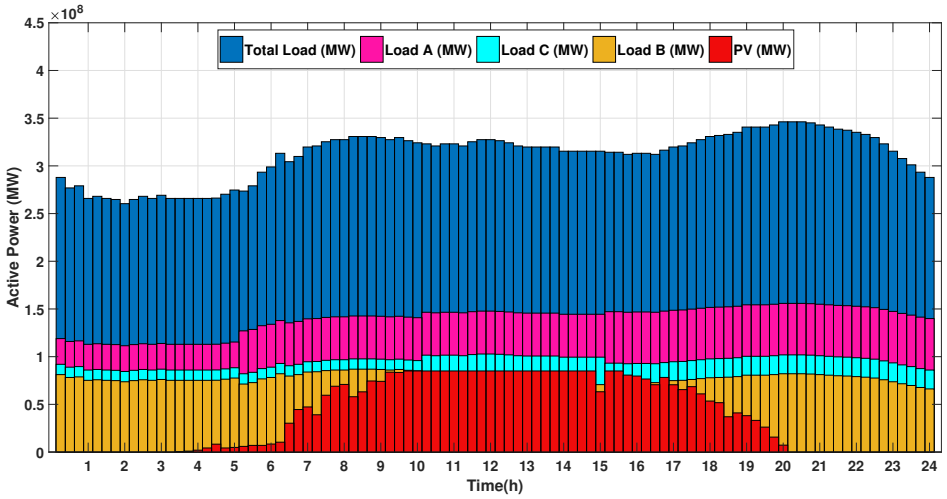

Figure 2.16: Active power of all the three connected loads, net load and PV in (MW)

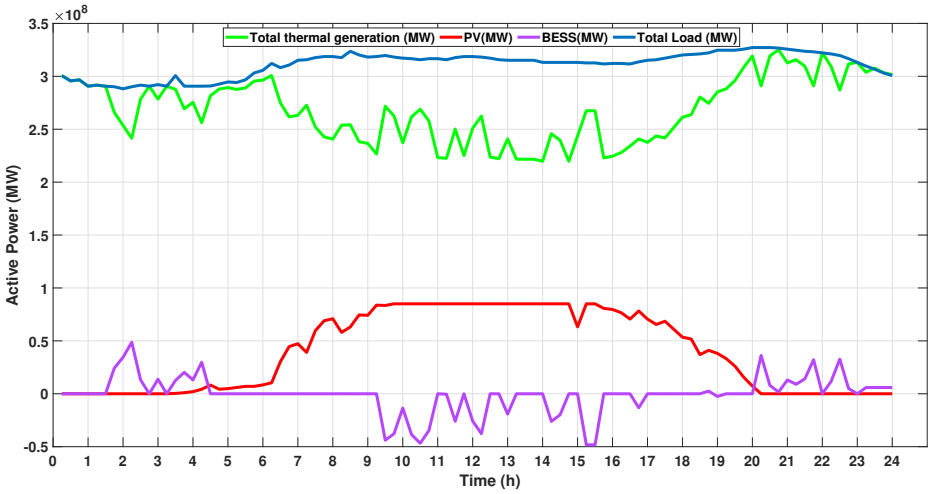

Figure 2.17: Total generation, battery power, PV and the total load demand in (MW)

discharge in coordination with thermal generating units (G1 and G2) to meet load demands, and to minimize generation costs. It also manages the storage capacity with regular charge and discharge cycles, adjusting for load demand variations.

Fig. 2.18 illustrates the OPF results as three voltage magnitudes (V2, V4, V6) across the three connected loads of the IEEE-9 bus system, revealing that these voltages remain within permissible limits, ensuring system security.

Fig. 2.19 shows the optimized result of SOC of the BESS. This figure, reveals that by the end of the day (after 24 hours), the battery's SOC remained charged (as specified in eq. 16). Additionally, Fig. 2.19, illustrates that the EMS methodology has enabled more efficient

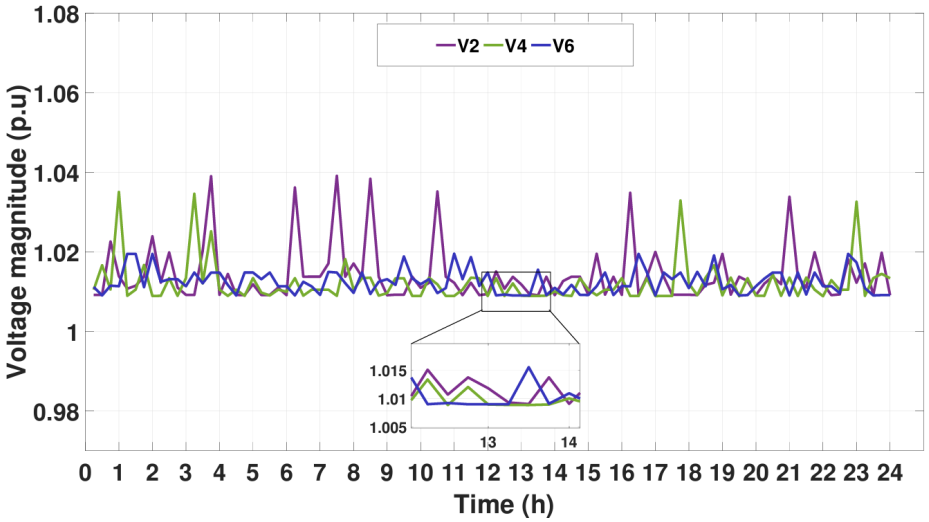

Figure 2.18: OPF-based voltage magnitudes in p.u. at three different nodes

Table 2.6: Parametric data about costs

Sources	Parameters	Values
G_1	a_1	2000
	b_1	30
	c_1	0.15
G_2	a_2	2600
	b_2	20
	c_2	0.11
BESS	Rated capacity (E_{rated})	150 MWh
	Total number of cycles (n_t)	5000
	Depth of discharge (DOD)	80%
	Efficiency (η)	95%

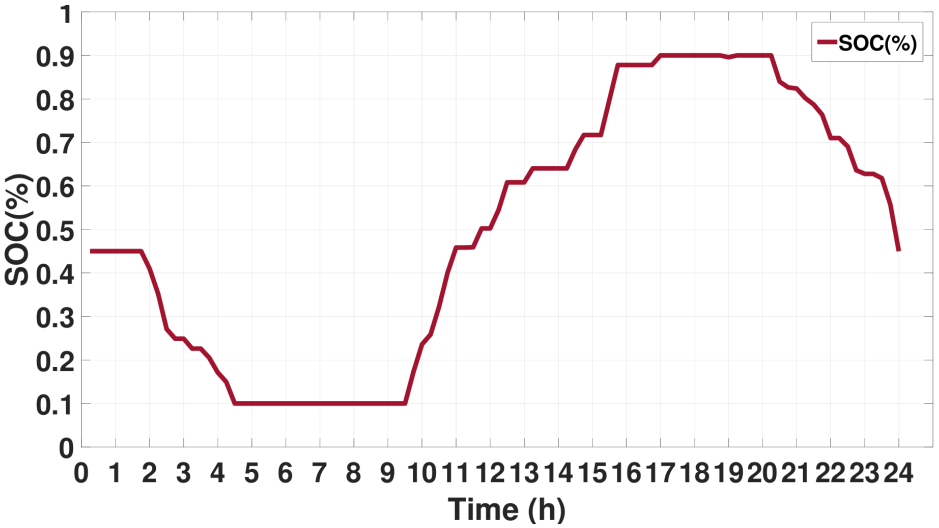

Figure 2.19: BESS SOC (%)

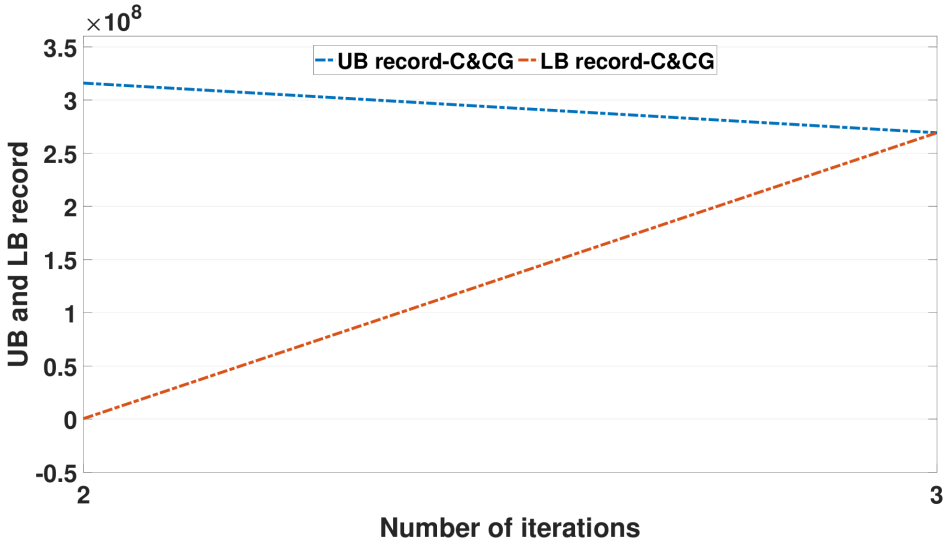

Figure 2.20: C&CG Convergence

management of supplying and draining cycles of the BESS. This is important, because if there are more frequent charging and discharging cycles, then it leads to increased aging costs. These results are attributed to the economic scheduling of the BESS (charging and discharging events) achieved by applying the TSRO within the EMS approach. Fig. 2.20 displays the convergence results of the C&CG algorithm, showing that it achieves smooth and rapid convergence. Table. 2.6 provides parametric data for the thermal generation cost coefficients and BESS aging cost parameters.

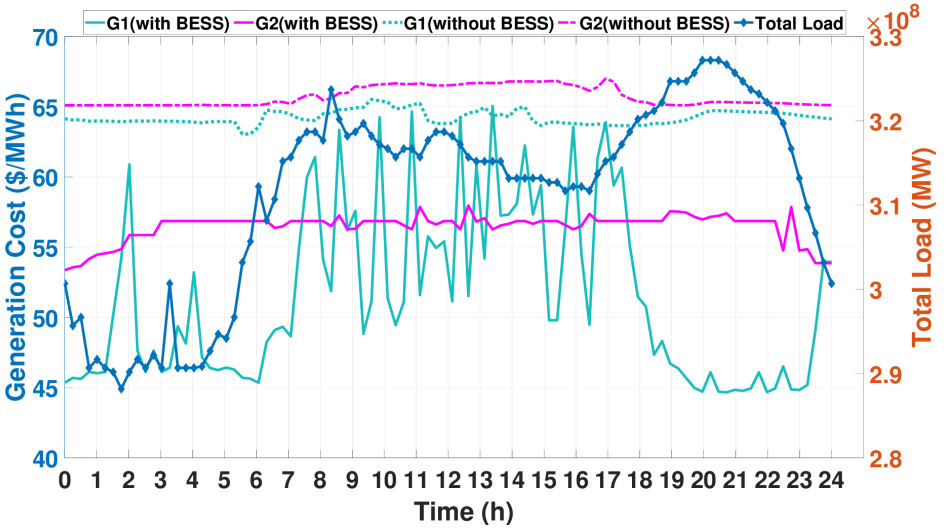

Figure 2.21: Generation costs ($/MWh) with and without BESS, along with total load demand (MW)

Fig. 2.21 demonstrates that generation cost is lower when BESS is installed, compared

to a scenario without BESS installation. The inclusion of BESS along with its economically optimized scheduling, has significantly helped to reduce the overall thermal generation cost. From the results, it can be analyzed that with BESS, the average generation cost across both thermal units is 55.0520 ($/MWh). In contrast without BESS consideration, the average generation cost increases to 64.9943 ($/MWh) over the course of a day. Finally, the simulation results show that the inclusion of BESS and its economically optimized scheduling has contributed significantly to reducing the overall thermal generation cost compared to not considering the BESS. In future works, the multi-time scale-based dynamical robust optimization approach can be utilized for the DERs to enhance the power system flexibility and reliability.

Chapter 3

Frequency Regulation and Inertia Control

The variability of renewable energy sources (RESs) like photovoltaic (PV) systems, combined with fluctuating load demands, can cause passive power fluctuations due to power converter control actions, which compromise system reliability, stability, and security. Additionally, small, non-synchronous islands with inherently low inertia will face increasing challenges in the coming years as they integrate larger amounts of renewable energy, further reducing system inertia. To address these challenges, implementing frequency regulation and inertia control services in power distribution networks is essential, as these services are crucial for maintaining stability and reliability. Moreover, integrating a hybrid energy storage systems (HESS) that includes a Unitized regenerative fuel cell (URFC) with real-time operational constraints can facilitate long-term, economical, and secure energy dispatching.

This chapter presents a study on frequency regulation and inertia control in Microgrid (MG), aimed at enhancing network reliability and stability by ensuring consistent voltage and frequency supply, even amidst varying load demands.

3.1 Frequency regulation in islanded microgrids incorporating RESs and HESS using a disturbance observer

This section discusses a robust Integral terminal sliding mode control (ITSMC) control methodology combined with a disturbance observer (DO) to enhance power balance and

frequency regulation in islanded MGs, accounting for uncertainties and incorporating the participation of HESS. Additionally, using the ITSMC enhances the performance of the secondary controller in MG operations, further enhancing the system's flexibility and stability under sudden load variations and changing weather conditions. A genetic algorithm has been employed to optimally tune the gains of the proposed control approach and the performance of the proposed controller has been analyzed using MATLAB/Simulink.

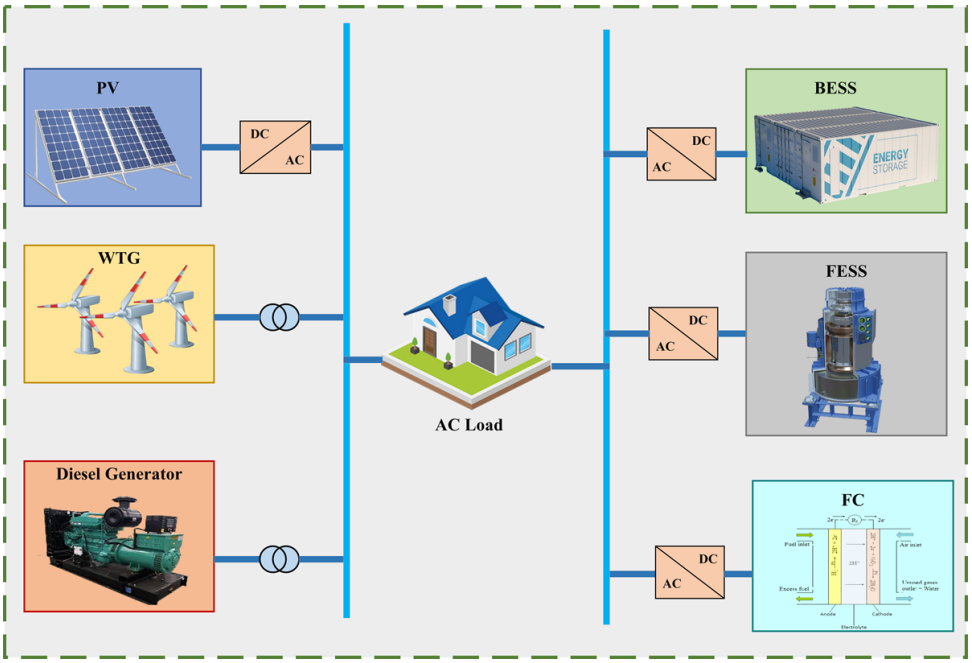

Figure 3.1: Schematic diagram of the islanded MG model under study

3.1.1 Mathematical Modeling of Islanded Microgrid

The islanded MG configuration considered in this study is illustrated in Fig. 3.1. It includes two different RESs, namely a PV and a wind turbine generator (WTG), along with DGs and HESS comprising a flywheel energy storage system (FESS) and a battery energy storage systems (BESS), as well as fuel cell (FC), all incorporated to meet the load demands. Fig. 3.2 depicts the control architecture of the proposed model, while Fig. 3.3 shows the frequency response of the MG model under study. The entire islanded MG model is represented by the following differential equations, which are designed based on the study discussed in [107].

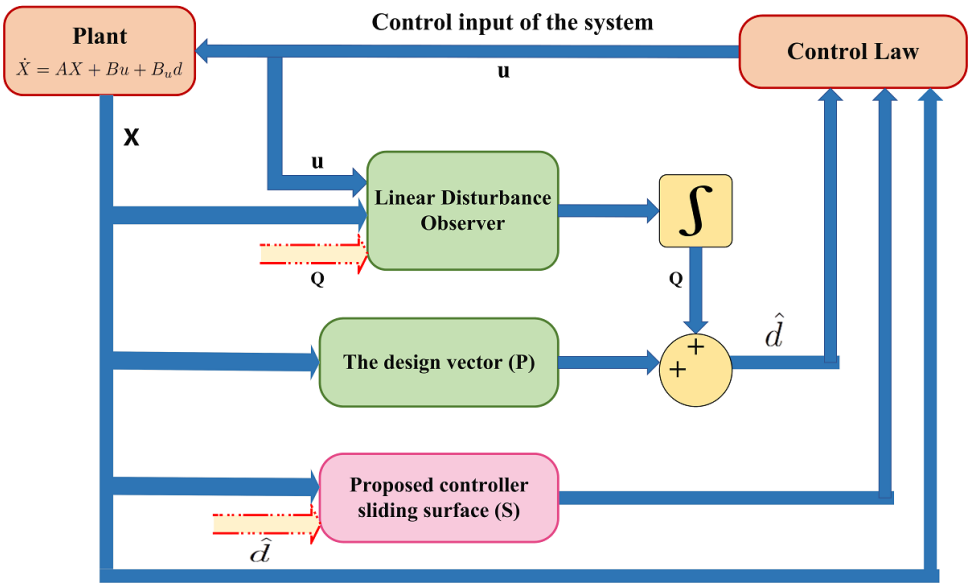

Figure 3.2: Control architecture of the proposed control methodology

$$\Delta\dot{F} = -\frac{D}{2H} - \frac{1}{2H}\Delta P_g - \frac{1}{2H}\Delta P_{FC} - \frac{1}{2H}\Delta P_{BESS} - \frac{1}{2H}\Delta P_{FESS} - \frac{1}{2H}\Delta P_{Dist}; \tag{3.1a}$$

$$\Delta\dot{P}_{FESS} = -\frac{1}{T_{FESS}}\Delta P_{FESS} + \frac{1}{T_{FESS}}\Delta F; \tag{3.1b}$$

$$\Delta\dot{P}_{BESS} = -\frac{1}{T_{BESS}}\Delta P_{BESS} + \frac{1}{T_{BESS}}\Delta F; \tag{3.1c}$$

$$\Delta\dot{P}_g = -\frac{1}{T_t}\Delta P_{BESS} + \frac{1}{T_t}\Delta X_g; \tag{3.1d}$$

$$\Delta\dot{X}_g = -\frac{1}{T_g}\Delta X_g - \frac{1}{R.T_g}\Delta F + \frac{1}{T_g}u; \tag{3.1e}$$

$$\Delta\dot{P}_{FC} = -\frac{1}{T_c}\Delta P_{FC} + \frac{1}{T_c}\Delta X_{FC}; \tag{3.1f}$$

$$\Delta\dot{X}_{FC} = -\frac{1}{T_{inv}}\Delta X_{FC} + \frac{1}{T_{inv}}\Delta T_{inv}; \tag{3.1g}$$

$$\Delta\dot{T}_{inv} = -\frac{1}{T_{FC}}\Delta T_{inv} + \frac{1}{T_{FC}}u, \tag{3.1h}$$

where ΔF to ΔT_{inv} represent the system states which include frequency deviation, output active power variations of FESS, BESS, generator, FC, and the variations in their corresponding reactances and inverter function.

Eqs. (3.1a) to (3.1h) can be reformulated by the state space model as mentioned in Eqs.

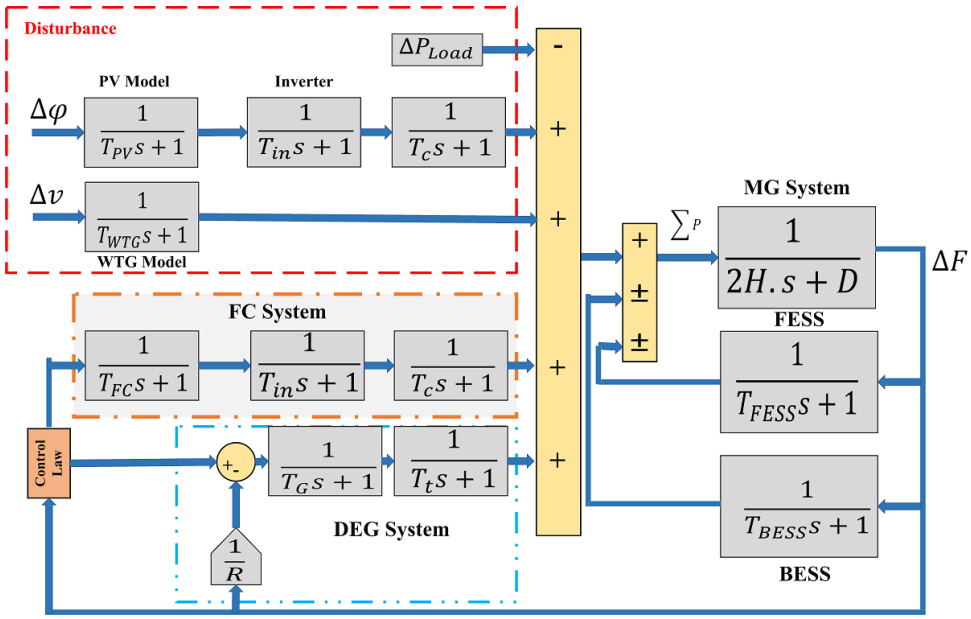

Figure 3.3: Frequency response of MG model, under study

(3.4a) (3.4b) to rewrite the system equations in the matrix form as follows:

$$\dot{X} = AX + Bu + B_u d, \tag{3.2}$$

where $X = [\Delta F, \Delta P_{FESS}, \Delta P_{BESS}, \Delta P_g, \Delta X_g, \Delta P_{FC}, \Delta X_{FC}, \Delta T_{inv}]$ are the system states, u denotes the control input of the system and the d represents the disturbance of the system and can be defined as variation in solar irradiance or wind speed or load variation. The system output is denoted by Y. Assume that disturbance meets the following condition as, $||d|| < h$, where h is the upper bound of the disturbance. The Eq. (3.2) can be rewritten in the matrix form as follows:

$$A = \begin{bmatrix} -\frac{D}{2H} & -\frac{1}{2H} & -\frac{1}{2H} & -\frac{1}{2H} & 0 & -\frac{1}{2H} & 0 & 0 \\ \frac{1}{T_{FESS}} & -\frac{1}{T_{FESS}} & 0 & 0 & 0 & 0 & 0 & 0 \\ \frac{1}{T_{BESS}} & 0 & -\frac{1}{T_{BESS}} & 0 & 0 & 0 & 0 & 0 \\ 0 & 0 & 0 & -\frac{1}{T_t} & \frac{1}{T_t} & 0 & 0 & 0 \\ -\frac{1}{R.T_g} & 0 & 0 & 0 & -\frac{1}{T_g} & 0 & 0 & 0 \\ 0 & 0 & 0 & 0 & 0 & -\frac{1}{T_c} & \frac{1}{T_g} & 0 \\ 0 & 0 & 0 & 0 & 0 & 0 & -\frac{1}{T_{inv}} & \frac{1}{T_{inv}} \\ 0 & 0 & 0 & 0 & 0 & 0 & 0 & -\frac{1}{T_{FC}} \end{bmatrix}, B = \begin{bmatrix} 0 \\ 0 \\ 0 \\ 0 \\ \frac{1}{T_g} \\ 0 \\ 0 \\ \frac{1}{T_{FC}} \end{bmatrix}, B_u = \begin{bmatrix} -\frac{1}{2H} \\ 0 \\ 0 \\ 0 \\ 0 \\ 0 \\ 0 \\ 0 \end{bmatrix} \tag{3.3}$$

By considering Eqs. 3.2 and 3.3, we can reformulate the state space equation as follows:

$$\dot{x_1} = \alpha_{11}x_1 + \alpha_{12}x_2 + \zeta d; \tag{3.4a}$$

$$\dot{x_2} = \alpha_{21}x_1 + \alpha_{22}x_2 + Bu, \tag{3.4b}$$

where $(\alpha_{11})^{(1\times1)}$, $(\alpha_{12})^{(1\times7)}$, $(\alpha_{21})^{(7\times1)}$ and $(\alpha_{22})^{(7\times7)}$ are the system matrices and their corresponding elements values are defined in Table 3.1, respectively. The power balance equation can be written as follows:

$$\begin{aligned}\sum P = \Delta P_{PV} + \Delta P_{WTG} + \Delta P_g + \Delta P_{FC} \pm \Delta P_{FESS} \\ \pm \Delta P_{BESS} - \Delta P_{Load} = 0.\end{aligned} \tag{3.5}$$

3.1.2 Proposed robust control methodology design

This section illustrates the design formulation of the proposed controller by considering the integrated effect of the proposed DO and the ITSMC on achieving the defined control objectives.

3.1.2.1 Design of disturbance observer

This subsection demonstrates the design formulation of the DO that is utilized to estimate the disturbance effect on the MG model, under study. The time domain equations of the DO can be written as follows:

$$\dot{Q} = -PB_d(Q + Px) - P(\alpha x + Bu); \tag{3.6a}$$

$$\hat{d} = Q + Px, \tag{3.6b}$$

where Q is the inertial variable vector of the observer, while P is the vector used to drive estimation error, which is defined as

$$e_d = \hat{d} - d, \tag{3.7}$$

where $\hat{d}$ is the estimated disturbance. The derivative of Eq. (3.7) is taken and compensated by considering Eq. (3.2), we can write the derivative of estimation error e_d as follows:

$$\dot{e}_d = -PB_d e_d - \dot{d}. \tag{3.8}$$

Remark 1: In the study, we assumed that $||d|| \leq h$, and $||\hat{d}|| \leq \hat{h}$ are the upper bounds for the disturbance and estimated disturbance, respectively.

Remark 2: We considered that the derivative of disturbance in the MG model, under study, is bounded and satisfies the condition $||\dot{d}|| \leq \dot{h}$, with $\lim_{t\to\infty}||\dot{d}|| = 0$. Under this condition, the estimated disturbance appears asymptotically stable, and the error satisfies the $\lim_{t\to t_1}||e_d|| = 0$. By considering this assumption, the vector P is effectively chosen, such that $-PB_d$ is Hurwitz. This ensures the finite-time convergence of the disturbance estimation error.

3.1.2.2 Design of robust ITSMC Integrated with disturbance observer

For the sake of designing an ITSMC-DO, the initial step is to introduce the tracking error e_1 as follows:

$$e_1 = y_{dist} - y, \tag{3.9}$$

where e_1 is the error between the actual frequency and frequency deviation and y represents the output. Taking the time derivative of Eq. 3.9, we get

$$\dot{e}_1 = \dot{y}_{dist} - \dot{y}. \tag{3.10}$$

Now consider the terminal sliding surface as follows:

$$S = \xi x_1 + \gamma x_2 + e_1 + h_1 \left(\int_0^t e_1 dt \right)^{\frac{p_1}{q_1}} + \tilde{d}, \tag{3.11}$$

where ξ, h_1 are the constant numbers and $\gamma^{(1\times 7)}$ is the constant vector that is designed for the system stability. p_1, q_1 are the odd numbers and their values are chosen as $1<p_1/q_1<2$, while $\tilde{d}$ shows the estimated disturbance.

We obtain the values of x_1 from Eq. 3.11 by considering $S = 0$ as follows:

$$x_1 = -\frac{\gamma}{\xi} x_2 - \frac{e_1}{\xi} - \frac{h_1}{\xi} \left(\int_0^t e_1 dt \right)^{\frac{p_1}{q_1}} - \frac{1}{\xi} \tilde{d}. \tag{3.12}$$

Now by putting the value of x_1 into Eq. (3.4), we have

$$\dot{x_1} = \alpha_{11}\left(-\frac{\gamma}{\xi}x_2 - \frac{e_1}{\xi} - \frac{h_1}{\xi}\left(\int_0^t e_1 dt\right)^{\frac{p_1}{q_1}} - \frac{1}{\xi}\tilde{d}\right) + \alpha_{12}x_2 + \zeta d; \tag{3.13a}$$

$$\dot{x_2} = \alpha_{21}\left(-\frac{\gamma}{\xi}x_2 - \frac{e_1}{\xi} - \frac{h_1}{\xi}\left(\int_0^t e_1 dt\right)^{\frac{p_1}{q_1}} - \frac{1}{\xi}\tilde{d}\right) + \alpha_{22}x_2 + Bu. \tag{3.13b}$$

Taking the time derivative of Eq. 3.11, we get

$$\dot{S} = \xi\dot{x}_1 + \gamma\dot{x}_2 + \dot{e}_1 + h_1 e_1\left(\frac{p_1}{q_1}\right)\left(\int_0^t e_1 dt\right)^{\frac{p_1-q_1}{q_1}} + \dot{\tilde{d}}. \tag{3.14}$$

Now by considering the Lyapunov candidate function to ensure the asymptotic stability of the entire system as

$$V_1 = \frac{1}{2}S^T S. \tag{3.15}$$

Taking the time derivative of Eq. 3.15 , we have

$$\dot{V}_1 = S^T \dot{S}. \tag{3.16}$$

Putting the value of $\dot{S}$ from Eq. 3.14 into Eq. 3.16, we have

$$\dot{V}_1 = S^T\left[\xi\dot{x}_1 + \gamma\dot{x}_2 + \dot{e}_1 + h_1 e_1\left(\frac{p_1}{q_1}\right)\left(\int_0^t e_1 dt\right)^{\frac{p_1-q_1}{q_1}} + \dot{\tilde{d}}\right]. \tag{3.17}$$

After putting the values of $\dot{x}_1$, $\dot{x}_2$ into Eq. 3.17 , we have

$$\dot{V}_1 = S^T\left[\xi\left(\alpha_{11}\left(-\frac{\gamma}{\xi}x_2 - \frac{e_1}{\xi} - \frac{h_1}{\xi}\left(\int_0^t e_1 dt\right)^{\frac{p_1}{q_1}} - \frac{1}{\xi}\tilde{d}\right) + \alpha_{12}x_2 + \zeta d\right) + \gamma\left(\alpha_{21}\left(-\frac{\gamma}{\xi}x_2 - \frac{e_1}{\xi} - \frac{h_1}{\xi}\left(\int_0^t e_1 dt\right)^{\frac{p_1}{q_1}} - \frac{1}{\xi}\tilde{d}\right) + \alpha_{22}x_2 + Bu\right) + \dot{e}_1 + h_1 e_1\left(\frac{p_1}{q_1}\right)\left(\int_0^t e_1 dt\right)^{\frac{p_1-q_1}{q_1}} + \dot{\tilde{d}}\right]. \tag{3.18}$$

To ensure the asymptotic stability of the system, it is considered that the conditions described in remarks 1 and 2 are satisfied. From Eq. (3.18), we obtained the control law as follows:

$$u = \frac{1}{\gamma B}\Bigg\{\Bigg(-\xi A_{12} + \alpha_{11}\gamma - \alpha_{22}\gamma + \frac{\gamma\alpha_{21}\gamma}{\xi}\Bigg)x_2 + \Bigg(h_1\alpha_{11} + \frac{\gamma\alpha_{21}h_1}{\xi}\Bigg)\Bigg(\int_0^t e_1 dt\Bigg)^{\frac{p_1}{q_1}} + \Bigg(\alpha_{11} + \frac{\gamma\alpha_{21}}{\xi} - h_1\Bigg(\frac{p_1}{q_1}\Bigg)\Bigg(\int_0^t e_1 dt\Bigg)^{\frac{p_1-q_1}{q_1}}\Bigg)e_1 - \dot{e_1} + \frac{\gamma\alpha_{21}}{\xi}\tilde{d} - \dot{\tilde{d}} - K\text{sgn}(S) - \lambda S\Bigg\}, \tag{3.19}$$

where K and λ are the switching gains and u is the required control law obtained from the proposed ITSMC-DO controller. To ensure the stability of the system, by putting the value of Eq. 3.19 into Eq. (3.18) and by some simplifications, we have

$$\dot{V}_1 = S^T(-K\text{sgn}(S) - \lambda(S) + \xi\zeta d - \alpha_{11}\tilde{d}), \tag{3.20}$$

where $\alpha_{11} = -\frac{D}{2H}$, $\zeta = -\frac{1}{2H}$, and $\xi = D$. By putting these aforementioned values into Eq. (3.20) and after some simplifications, we get

$$\dot{V}_1 = -S^T K\text{sgn}(S) - S^T\lambda(S) - S^T\frac{D}{2H}e_d; \tag{3.21a}$$

$$\dot{V}_1 \leq -K|S| - \lambda||S||^2 - S^T\frac{D}{2H}e_d. \tag{3.21b}$$

By taking into account the $K \geq \frac{D}{2H}$, the derivative of the Lyapunov function at the finite time will become as follows:

$$\dot{V}_1 \leq -\lambda||S||^2 - KS\text{sgn}(S). \tag{3.22}$$

Eq. (3.22) ensures the asymptotic stability of the system.

Table 3.1: Parametric data about MG model and controller

Specifications	**Values**					
System Parameters	$T_{PV}(s)$	$T_{WTG}(s)$	$T_{FESS}(s)$	$T_{BESS}(s)$	T_g (s)	$T_{FC}(s)$
	1.8	1.5	0.01	0.1	0.08	0.26
-	$H(pu)(s)$	$T_{inv}(s)$	$T_c(s)$	$D(pu/Hz)$	$T_t(s)$	$R(Hz/pu)$
	0.0833	0.04	0.004	0.015	0.4	3
Controller Parameters	K	λ	$p1/q1$	h_1	-	-
	$1e^{-3}$	$1e^{-4}$	1.001	$1e^{-4}$	-	-

The efficiency of the proposed robust ITSMC-DO is evaluated in MATLAB/Simulink.

This software is compatible with Power hardware-in-the loop (PHIL) real-time setup too, installed at LabZERO, Politecnico di Bari, Italy. Table 3.1 presents the design parameter values of the proposed controller.

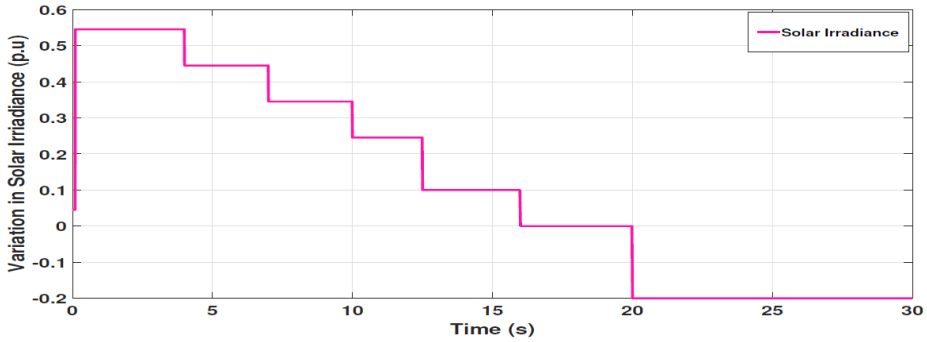

Figure 3.4: Solar irradiance changing pattern

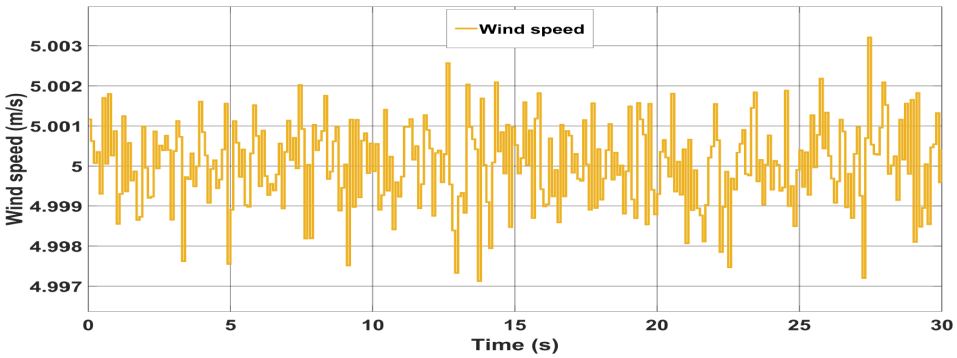

Figure 3.5: Wind speed changing pattern

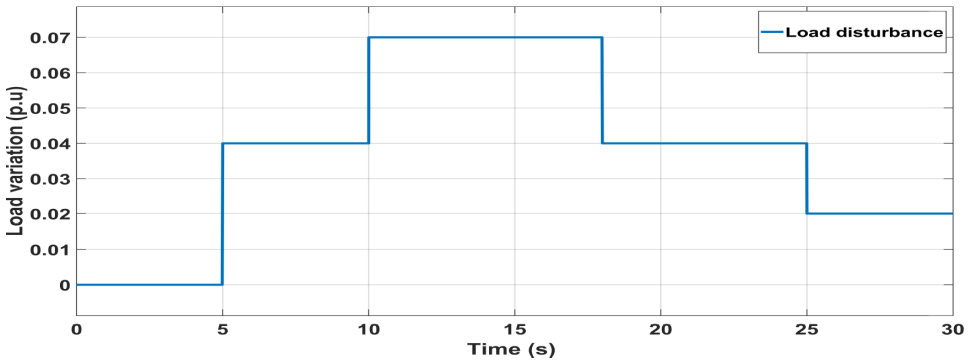

Figure 3.6: Load Variation

3.1.2.3 Robust ITSMC-DO performance analysis and results discussion

This section illustrates the results obtained from the ITSMC-DO and Integral sliding mode control (ISMC)-DO. The ISMC-DO is introduced solely for comparison purposes with the ITSMC-DO. Fig. 3.4 represents the solar irradiance variation pattern, while Fig. 3.5 shows the wind speed changing pattern, and Fig. 3.6 depicts the load variation pattern of the system. These variations are adopted as disturbances to test the validity and robustness of the proposed controller.

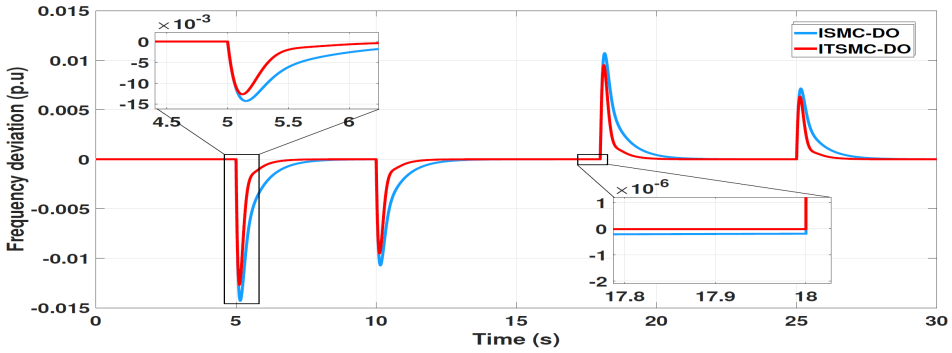

Figure 3.7: Frequency deviation (p.u) under load variations

From Fig.3.7 and Fig.3.8, it can be seen that under the effects of aforementioned disturbances, the ITSMC-DO provides robust frequency regulation with a better and faster response as compared to the ISMC-DO. This subsection compares the performance of the proposed ITSMC-DO controller with ISMC-DO and literature-suggested controllers, namely PID and fuzzy logic-based PID. From Fig. 3.7, the simulation behavior of frequency regulation of islanded MGs under external disturbances can be analyzed for both ITSMC-DO and ISMC-DO. The figure shows some overshoots/undershoots in the frequency signal at various time intervals due to sudden load variations. These fluctuations occur in both ITSMC-DO and ISMC-DO, but their magnitudes are lower in the case of the proposed ITSMC-DO controller, which also provides fast and finite time convergence.

From Fig. 3.8, it can be observed how the frequency of the islanded MG varies under the effects of RESs uncertainties such as wind speed and solar irradiance at different time intervals, which are also linked with the changing patterns of power generation from the PV and WTG. Overall, the frequency is robustly regulated with ITSMC-DO compared to ISMC-DO and the other literature-suggested controllers.

A numerical comparison between the proposed controllers and literature-suggested controllers is provided based on the performance index as mentioned in Table. 3.2, considering disturbance effects. The performance index $\int_0^t |\Delta F|^2 dt$, where ΔF represents frequency

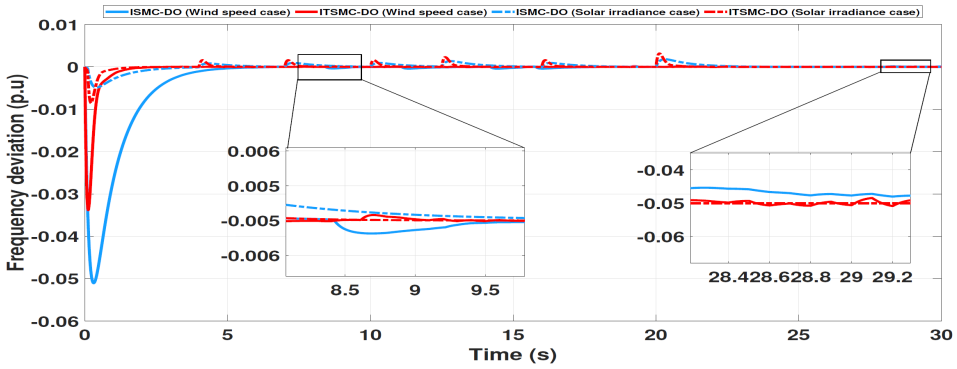

Figure 3.8: Frequency deviation (p.u) in the case of wind speed and solar irradiance variation

Table 3.2: Comparison analysis on the basis of performance index

Control techniques	**Performance index**
[108] Conventional PI	0.00024
[108] Fuzzy-based PI	0.00020
[109] Fractional-order type-2 fuzzy	0.00011
ISMC-DO	$3.1587e^{-6}$
ITSMC-DO	$2.0893e^{-8}$

deviation is considered, and calculated based on load variations. From Table. 3.2, it can be seen that the performance index value for frequency deviation is $2.0893e^{-8}$ for the ITSMC-DO controller, while it is $3.5187e^{-6}$ for the ISMC-DO controller. The performance index values are higher for the conventional proportional integrator (PI), fuzzy-based PI, and Fractional-order type-2 fuzzy at 0.00024, 0.00020, and 0.00011, respectively. This comparison allows us to conclude that compared to ISMC-DO, conventional PI, fuzzy-based PI, and Fractional-order type-2 fuzzy, the ITSMC-DO controller provides better control performance by attenuating the effects of parametric uncertainties and external disturbances.

In conclusion, this study presents a robust ITSMC controller integrated with a DO to accurately estimate the impacts of mismatch uncertainties and external disturbances, ensuring effective frequency regulation in the islanded MG. The proposed ITSMC-DO approach achieves fast and finite convergence while addressing system disturbances and uncertainties, all without inducing the chattering phenomenon.

3.2 A novel hierarchical control framework for frequency regulation of islanded microgrids

The variability of RESs, such as PV, along with fluctuating load demands, can result in passive power fluctuations due to power converter controllers, which may compromise the EMS and pose security risks. Therefore, following the development and analysis of a robust nonlinear controller with a DO for frequency regulation in islanded MGs in Section 3.1, this study expands to address these challenges across all three control layers. Recent trends in designing microgrid secondary controllers focus on distributed controllers that rely on information sharing among entities. While this approach enhances scalability, it necessitates robust communication networks, advanced algorithms, and careful consideration of trade-offs between local and global system objectives.

This section introduces a novel multi-time scale, centralized hierarchical control approach to improve stability, security, and reliability in power dispatch tracking within islanded microgrids. The proposed framework incorporates grid-forming control behavior across primary, secondary, and tertiary control layers, each with distinct optimization goals and constraints in a convex model, to achieve stable and reliable power tracking alongside frequency and voltage regulation. Additionally, it ensures secure and economical long-term energy dispatching through a HESS that includes a URFC with real-time operational constraints. In this framework, the secondary layer utilizes MPC to correct power tracking deviations from grid-forming control actions and handles voltage and frequency regulation, while the tertiary layer employs mixed integer linear programming (MILP) to adjust power references according to economic and security constraints. The effectiveness of this framework is validated through MATLAB/Simulink simulations.

The main contributions of this research study are;

- In this research, an MPC approach with a novel cost function—incorporating the weighted difference between output power and the tertiary control reference value—has been implemented in the secondary control layer to effectively manage power tracking deviations while stabilizing frequency and voltage. This approach enhances the security of power dispatch operations within the proposed methodology.

- The tertiary control layer, guided by the EMS, introduces a new modeling strategy that accounts for various primary control layer behaviors. For grid-forming units, the proposed EMS integrates power and capacity margin constraints with penalty

factors, along with the N-1 principle, to ensure the reliability and security of the entire power system.

- Additionally, precise power tracking in grid-following units enhances economic dispatch value. Economic considerations are addressed innovatively, factoring in variable operating efficiency based on working conditions, real operational constraints like turn-off latency during URFC mode conversion, and other economic elements to ensure cost-effective scheduling that minimizes the system's overall operational costs.

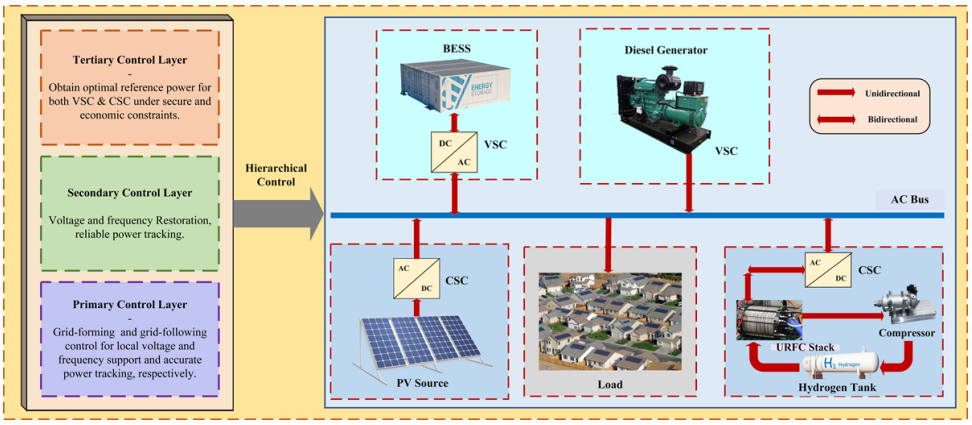

Figure 3.9: Architecture of islanded microgrid under study

3.2.1 Problem formulation and physical Dynamics of AC islanded microgrids

In this section, as illustrated in Fig.3.9, the islanded microgrid model includes a diesel generator and battery controlled as voltage source converter (VSC), while PV and URFC are controlled as current source converter (CSC). Fig.3.10 presents the proposed hierarchical control framework for the islanded microgrid. Although URFC has some limitations, such as low power output and round-trip efficiency, it holds significant value for islanded microgrids due to its compact size and bidirectional power flow capability [110]. This paper focuses on addressing security, stability, and power-tracking challenges. Traditional EMS models mainly consider DERs characteristics but often overlook the associated control strategies. Here, additional security constraints for VSC are introduced to enhance microgrid security. Furthermore, this paper examines the URFC model, which is underexplored in the literature, as a current source, acknowledging its power fluctuations

that significantly impact efficiency across different operating points. Unlike conventional secondary control, which typically aims only to restore frequency and voltage, this study tackles power tracking deviations resulting from passive power fluctuations.

3.2.1.1 Primary control layer utilizing a grid-forming controller

In this study, DERs with rapid response capabilities and physical inertia characteristics, such as BESS and diesel generators, are chosen for grid-forming control to maintain transient power quality in the islanded microgrid. Conversely, units more sensitive to output fluctuations and aimed at maximizing utilization, such as PV and URFC, are selected for grid-following control to optimize economic performance. In the primary layer of the proposed framework, droop control is implemented in the VSC to enable grid-forming control, while the grid-following unit uses a current-voltage dual-loop control to respond directly to power dispatch commands from the upper EMS layer. The primary control loop dynamics for all $vs \in \mathcal{V}$ are expressed as follows:

$$\Omega_{vs}(t) = \Omega_0 - k_{\mathrm{d}P,vs}\left(P_{vs}(t) - P_{vs}^{ref}(t)\right) + \Omega_{s,vs}(t), \tag{3.23a}$$

$$\mathcal{V}_{vs}(t) = \mathcal{V}_0 - k_{\mathrm{d}Q,vs}\left(Q_{vs}(t) - Q_{vs}^{ref}(t)\right) + \mathcal{V}_{s,vs}(t), \tag{3.23b}$$

where P_{vs}^{ref} and Q_{vs}^{ref} represent the reference values of active and reactive power, which are time-varying because the EMS constantly updates them. Additionally, $\mathcal{V}_{s,vs}$ and $\omega_{s,vs}$ represent the secondary control layer signals for the voltage and frequency restoration, facilitating the tracking of active and reactive power.

3.2.1.2 AC power flow dynamics with a unitary power angle

To obtain the relationship between the power generation among the DERs with their power angle derivation, the formulation for calculating active and reactive power based on the power transferred, the coupling induction across the voltage source is employed $\mathcal{B}_{vs} = 1/(\mathcal{L}_{vs}\Omega_o)$ as mentioned in [111], as follows:

$$P_{vs}(t) = \mathcal{B}_{vs}\mathcal{V}_{vs}(t)\hat{\mathcal{V}}_{vs}^{\alpha}(t)\sin(\Delta\zeta_{vs}(t)), \tag{3.24a}$$

$$Q_{vs}(t) = \mathcal{B}_{vs}[{\mathcal{V}_{vs}}^2(t) - \mathcal{V}_{vs}(t)\hat{B}_{vs}^{\alpha}(t)\cos(\Delta\zeta_{vs}(t))], \tag{3.24b}$$

$$\Delta\zeta_{vs}(t) = \zeta_{vs}(t) - \hat{\zeta}_{vs}^{\alpha}(t) = \int_0^t \left(\Omega_{vs}(\tau) - \hat{\Omega}_{vs}^{\alpha}(\tau)d\tau\right)dt. \tag{3.24c}$$

From Fig. 3.10, it can be observed that the LCL filter is connected to the DGs and is composed of the components $\mathcal{L}_{vs}$, C_{vs}, and other $\mathcal{L}_{vs}$. The values of the frequency Ω_{vs}, voltage V_{vs}, current i_{vs}, and phase angle ζ_{vs} are measurable across the filter capacitor. Furthermore, a reduced-order observer as mentioned in [112], is considered to estimate the value of voltage $\hat{\mathcal{V}}_{vs}^{\beta}$, where $\mathcal{L}_{vs} = \alpha$ at the adjustment measurement node across $\mathcal{L}_{vs}$, whereas $\hat{\Omega}_{vs}^{\alpha}$ and $\hat{\zeta}_{vs}^{\alpha}$ are calculated through the phase locked loop (PLL) as mentioned in [113].

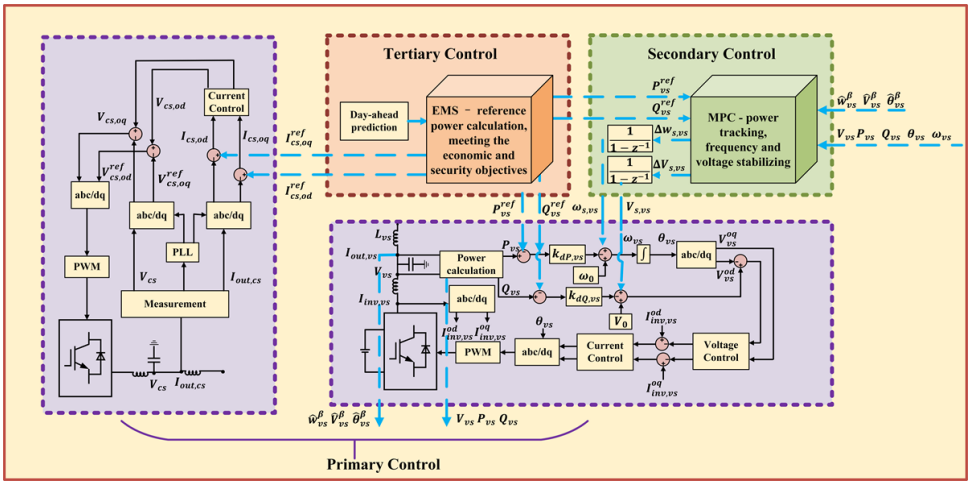

Figure 3.10: Centralized hierarchical control framework of islanded microgrid

3.2.2 Mathematical framework for the proposed control approach

This section illustrates the secondary control layer and tertiary control layer discrete modeling of the chosen objective function, in which the secondary control layer introduces power tracking on the basis of compensating frequency and voltage, and the tertiary control layer considers the secure and economic constraints to enhance the overall reliability of the system.

3.2.2.1 Secondary layer with MPC

This subsection details the design formulation of the MPC, introducing the objective function and constraints necessary for integrating the secondary control layer into the hierarchical control framework. Fig. 3.11 illustrates how MPC functions within the unified control architecture, embedded in the secondary control layer. The EMS-based tertiary control layer operates with a 24-hour prediction horizon and sends updated reference power values to the MPC every 15 minutes as the droop control target. The MPC optimizes

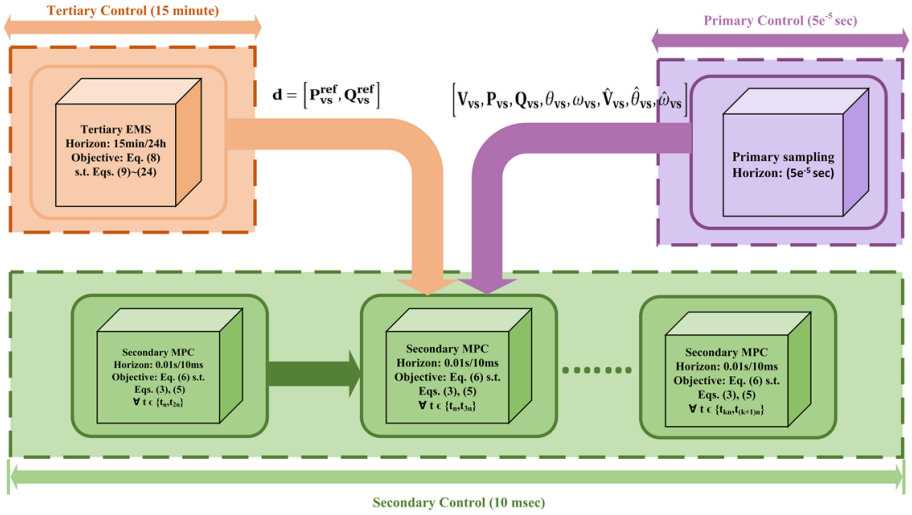

Figure 3.11: A unified control architecture for MPC design

the secondary control layer signal with a step size of 0.01 seconds and a prediction horizon of 0.1 seconds. Meanwhile, the primary control layer adopts a 50 ms sampling interval, typical in real-world applications, and updates the secondary control layer at the start of each MPC optimization period. As outlined, this integration is designed to effectively address discrepancies in power tracking along with voltage and frequency regulation. The predictive model, formulated as a quadratic program using the finite difference method, estimates future states within each sampling time T_s to meet the

objective function requirements, expressed as follows:

$$\begin{aligned}\Omega_{vs}(t_{n+l}) = \Omega_{vs}(t_{n+l-1}) + k_{\mathrm{d}P,vs}\Big[\big(P_{vs}(t_{n+l}) - P_{vs}(t_{n+l-1})\big) \\ - \big(P_{vs}^{ref}(t_{n+l}) - P_{vs}^{ref}(t_{n+l-1})\big)\Big] \\ + \Omega_{s,vs}(t_{n+l-1});\end{aligned} \tag{3.25a}$$

$$\begin{aligned}\mathcal{V}_{vs}(t_{n+l}) = \mathcal{V}_{vs}(t_{n+l-1}) + k_{\mathrm{d}Q,vs}\Big[\big(Q_{vs}(t_{n+l}) - Q_{vs}(t_{n+l-1})\big) \\ - \big(Q_{vs}^{ref}(t_{n+l}) - Q_{vs}^{ref}(t_{n+l-1})\big)\Big] \\ + \mathcal{V}_{s,vs}(t_{n+l-1});\end{aligned} \tag{3.25b}$$

$$\Delta\zeta_{vs}(t_{n+l}) = \Delta\zeta_{vs}(t_{n+l-1}) + T_s\Big[\Omega_{vs}(t_{n+l}) - \hat{\Omega}_{vs}^{\alpha}(t_n)\Big]; \tag{3.25c}$$

$$\begin{aligned}P_{vs}(t_{n+l}) = P_{vs}(t_n) + \Big[\Delta\zeta_{vs}(t_{n+l}) - \Delta\zeta_{vs}(t_n)\Big] \\ \times \mathcal{B}_{vs}\mathcal{V}_{vs}(t_n)\hat{\mathcal{V}}_{vs}^{\alpha}(t_n)\cos(\Delta\zeta_{vs}(t_n)) \\ + \Big[\mathcal{V}_{vs}(t_{n+l}) - \mathcal{V}_{vs}(t_n)\Big]\mathcal{B}_{vs}\hat{\mathcal{V}}_{vs}^{\alpha}(t_n)\sin(\Delta\zeta_{vs}(t_n));\end{aligned} \tag{3.25d}$$

$$\begin{aligned}Q_{vs}(t_{n+l}) = Q_{vs}(t_n) + \Big[\Delta\zeta_{vs}(t_{n+l}) - \Delta\zeta_{vs}(t_n)\Big] \\ \times \mathcal{B}_{vs}\mathcal{V}_{vs}(t_n)\hat{\mathcal{V}}_{vs}^{\alpha}(t_n)\sin(\Delta\zeta_{vs}(t_n)) \\ + \Big[V_{vs}(t_{n+l}) - \mathcal{V}_{vs}(t_n)\Big] \\ \times \mathcal{B}_{vs}\Big[2\mathcal{V}_{vs}(t_n) - \hat{\mathcal{V}}_{vs}^{\beta}(t_n)\Big]\cos(\Delta\zeta_{vs}(t_n));\end{aligned} \tag{3.25e}$$

$$\Omega_{vs}(t_{n+N_e}) = w_0,\ \mathcal{V}_{vs}(t_{n+N_e}) = \mathcal{V}_0, \tag{3.25f}$$

where $t_n = nT_s$, $n \in \mathcal{Z}^+$ and N_e denotes the prediction horizon. It is composed as: equality constraints in the form of Eqs. (3.25a) to (3.25e) are given based on Eqs. (3.23a), (3.23b), (3.24a), (3.24b), and (3.24c) respectively. It is worth noting that the system at each end of the optimization horizon t_{n+N_e} should be required to achieve convergence, as constrained by Eq. (3.25f).

The output of the MPC model is the incremental values of frequency and voltage at each sampling time, corresponding to $\Delta\Omega_{s,vs}$ and $\Delta\mathcal{V}_{s,vs}$, respectively. In order to eliminate steady-state errors, they are added as compensation signals to the new frequency and voltage reference values onto the primary control layer after an integration process, as

follows:

$$\Omega_{s,vs} = \int_0^t \Delta\Omega_{s,vs}(\tau)d\tau, \mathcal{V}_{s,vs} = \int_0^t \Delta\mathcal{V}_{s,vs}(\tau)d\tau. \tag{3.26}$$

The optimal cost function is chosen as illustrated in Eq. (3.27) and is composed of five terms with weight parameters $\gamma_1, \ldots, \gamma_5 \in \mathcal{R}^+$. Among these terms, the difference in frequency, voltage, and power differences with their reference values underweight, are minimized, while also minimizing the incremental control action. Minimizing the frequency and voltage deviations, as well as the control increment, ensures the stability of the system. On the other hand, minimizing the power tracking difference ensures the security and economic efficiency of the system. This is because the power reference values in the tertiary control layer are determined according to the economic and safety constraints and objectives, thus representing optimal economic and secure indicators as follows:

$$\begin{aligned} J(t_n) = & \sum_{vs\in\mathcal{V}} \sum_{l=1}^{Ne} \gamma_{1,vs}(\Omega_{vs}(t_{n+l}) - \Omega_0)^2 \\ & + \gamma_{2,vs}(P_{vs}(t_{n+l}) - P_0(t_{n+l}))^2 + \gamma_{3,vs}(\Delta\Omega_{s,vs}(t_{n+l-1}))^2 \\ & + \gamma_{4,vs}(\mathcal{V}_{vs}(t_{n+l}) - \mathcal{V}_0)^2 + \gamma_{5,vs}(\Delta\mathcal{V}_{s,vs}(t_{n+l-1}))^2, \end{aligned} \tag{3.27}$$

where $\gamma_{k,vs}(k = 1, ..., 5) \in \mathcal{R}^+$ are the optimizations weight factors.

Simultaneously altering the power angle of all VSCs to achieve power tracking through the secondary control layer is undesirable, as it would change the steady-state operating frequency of the islanded microgrid. Therefore, in the proposed study, the secondary control layer optimizes the VSC performance by assigning different $\alpha_{k,vs}$ values to ensure the security, stability, and economic operation of the islanded microgrid. Additionally, this work places a stronger emphasis on the power tracking of the battery rather than the diesel generator, especially when accounting for prediction errors in islanded microgrids. Accurate power tracking of the BESS ensures that the actual SOC consistently aligns with the predicted curve, staying within the upper and lower limits, which mitigates security risks, extends lifespan, and improves the reliability of future optimization outcomes. In contrast, although adjusting the steady-state power set point of a diesel generator impacts economic factors like fuel costs, it does not violate any EMS model constraints, as detailed in the following subsection 3.2.3.

3.2.3 Tertiary layer with EMS

This subsection presents the mathematical model of the EMS and introduces a strategy to differentiate the models of VSC and CSC, ensuring both economic and secure scheduling outcomes. It outlines the power margin, capacity margin, and N-1 emergency constraints for the islanded microgrid. Furthermore, to achieve optimal economic scheduling while maintaining security, the EMS fully leverages the HESS for the efficient operation of the islanded microgrid. The subsection also provides a comprehensive analysis of the URFC, examining how the operating point affects electric-hydrogen conversion efficiency and addressing the real-world physical constraints of URFC mode switching in practical applications.

3.2.3.1 Design of EMS objective function

The purpose of the tertiary layer is to achieve accurate power scheduling based on the objective of EMS, written as follows:

$$\min \mathcal{F}(t) = \sum_{t=1}^{T} \left(\sum_{vs \in \mathcal{V}} \left(\mathcal{C}_{vs}(t) + \xi_{vs}^{m} \mathcal{S}_{vs}(t) \right) + \sum_{cs \in C} \mathcal{C}_{cs}(t) \right). \tag{3.28}$$

This objective considers both the economy and security of the grid-forming VSC and the economy of the grid-following CSC, where C_{vs} and C_{cs} represent the economic cost of the VSC and CSC, respectively. ξ_{vs}^{m} and S_{vs} denote the weight parameters and security penalty factor, while the superscript m distinguishes between different margins, specifically referring to power margin and capacity margin in this proposed study.

3.2.3.2 Design of diesel generator

The quadratic cost function for the diesel generator is written as follows:

$$\mathcal{C}_{Dies}(t) = b_o P_{Dies}^{2}(t) + b_1 P_{Dies}(t) + b_2 \delta_{Dies}(t), \tag{3.29}$$

where $\mathcal{C}_{Dies}(t)$ is the generation cost of the diesel generator with cost coefficients $b_0, b_1, b_2 \in \mathcal{R}^{+}$. Since the diesel generator operates as a voltage source in the proposed study, the security margin has been constrained by ensuring that the output power of the generator

has sufficient margin to ramp up or ramp down as follows:

$$\mathcal{S}_{Dies}(t) = \xi_{Dies}^{pow}\left(P_{Dies}(t) - \frac{1}{2}\left(P_{Dies}^{max}(t) - P_{Dies}^{min}(t)\right)\right)^2, \tag{3.30}$$

where ξ_{Dies}^{pow} denotes the penalty weight coefficient.

A piecewise affine function as mentioned in [**?**], is utilized to linearize the nonlinear terms in Eqs. (3.29) and (3.30) and to construct the formulation, thereby improving the solving speed by considering the function as follows:

$$P_{Dies}^{aux}(t) = \begin{cases} P_{Dies}^2(t) \text{ and} \\ P_{Dies}^{aux}(t) \geq \max_{j\in J}\left\{k_j P_{Dies}(t) + o_j\right\}, \end{cases} \tag{3.31}$$

Eq. (3.31) guarantees that P_{Dies}^{aux} must be greater than or equal to the piecewise affine function which approximates the tangent P_{Dies}^2 at every discrete point in the feasible region. This approach is also used in the following quadratic terms to construct a model, it will not be repeatedly mentioned.

The power limits and ramping speed of the diesel generator are given as follows:

$$P_{Dies}^{min}\Delta_{Dies}(t) \leq P_{Dies}(t) \leq P_{Dies}^{max}\Delta_{Dies}(t), \tag{3.32a}$$

$$P_{Dies}^{RD}\Delta T \leq P_{Dies}(t) - P_{Dies}(t-\Delta T) \leq P_{Dies}^{RU}\Delta T. \tag{3.32b}$$

Eqs. (3.32a) and (3.32b) denote constraints for the diesel generator to adjust its power P_{Dies} on the lower and upper limits, ramping up and ramping down superscripts (as mentioned in nomenclature) to adjust the speed of diesel generator, respectively. ΔT represents the optimization step.

3.2.3.3 Development of a unitized regenerative fuel cell

Recently, fuel cell and electrolyzer manufacturers have increasingly focused on the lifespan of these systems, expressing their longevity in terms of operating hours, as noted in [114]. This is due to the fact that start up (SU) and start down (SD) cycles of the URFC, coupled with load demand fluctuations, can impact the functionality of these systems. Eq. (3.33) represents the URFC cost function, accounting for the life cycle, switching status, and

power fluctuations, as follows:

$$\begin{aligned} C_{urfc}(t) = \zeta_{urfc}\delta_{urfc}(t)\,\Delta T + C^{SU}_{urfc}\gamma^{on}_{urfc}(t) \\ + C^{SD}_{urfc}\gamma^{off}_{urfc}(t) + C^{flu}_{urfc}\Big(P_{urfc}(t) \\ - P_{urfc}(t-\Delta T)\Big)^2, \end{aligned} \tag{3.33}$$

where $\zeta_{urfc} = C^{Ins}_{urfc}/L_{H_2}$, while C_{urfc} denotes the cost coefficients for installation (Ins), and power fluctuations (flu) of the URFC. L_{H_2} is the life span in hours. $\Gamma^{on}_{urfc}(t)$ and $\Gamma^{off}_{urfc}(t)$ are the auxiliary logical variables that denote the SU and SD states, respectively, and are defined as:

$$\Gamma^{on}_{urfc}(t) = \max\{\Delta_{urfc}(t) - \Delta_{urfc}(t-\Delta T), 0\}, \tag{3.34a}$$

$$\Gamma^{off}_{\varepsilon}(t) = \max\{\delta_{urfc}(t-\Delta T) - \Delta_{urfc}(t), 0\}\Big|_{\varepsilon=urfc,Elz.} \tag{3.34b}$$

To avoid impacting the life span of the catalyst in the URFC, a standby period of 10-20 minutes is considered during the mode of the conversion process from the electrolyzer to the FC [114]. Using the Karnaugh map rules, Eqs. (3.34a) and (3.34b) can be expressed as a mixed logical dynamic (MLD) formulation in the form of

$$\Gamma^{on}_{urfc}(t) = \Delta_{urfc}(t) \cap \left(\neg\Delta_{urfc}(t-\Delta T)\right), \tag{3.35a}$$

$$\Gamma^{off}_{\varepsilon}(t) = \Delta_{\varepsilon}(t-\Delta T) \cap (\neg\Delta_{\varepsilon}(t))\Big|_{\varepsilon=urfc,elz.} \tag{3.35b}$$

To achieve a unified framework considering the evolution from an MLD to inequality constraints, as mentioned in [115], we incorporate based on the discrete-time system as

shown in Eqs. (3.36a) to (3.36f) below:

$$-\Delta_{urfc}(t)+\Gamma^{on}_{urfc}(t)\leq 0, \tag{3.36a}$$

$$-\left(1-\Delta_{urfc}(t-\Delta T)\right)+\Gamma^{on}_{urfc}(t)\leq 0, \tag{3.36b}$$

$$\Delta_{urfc}(t)+\left(1-\Delta_{urfc}(t-\Delta T)\right)-\Gamma^{on}_{urfc}(t)\leq 1, \tag{3.36c}$$

$$-\Delta_{\varepsilon}(t-\Delta T)+\Gamma^{off}_{\varepsilon}(t)\leq 0\Big|_{\varepsilon=urfc,Elz,} \tag{3.36d}$$

$$-(1-\Delta_{\varepsilon}(t))+\Gamma^{off}_{\varepsilon}(t)\leq 0\Big|_{\varepsilon=urfc,Elz,} \tag{3.36e}$$

$$\Delta_{\varepsilon}(t-\Delta T)+(1-\Delta_{\varepsilon}(t))-\Gamma^{off}_{\varepsilon}(t)\leq 1\Big|_{\varepsilon=urfc,Elz,} \tag{3.36f}$$

The power limitations and standby constraints of the URFC are defined as follows:

$$\Delta_{urfc}(t)=\Delta_{fc}(t)+\Delta_{elz}(t), \tag{3.37a}$$

$$P_{urfc}(t)=P_{fc}(t)-P_{Elz}(t), \tag{3.37b}$$

$$P^{min}_{FC}\Delta_{FC}(t)\leq P_{FC}(t)\leq P^{max}_{FC}\Delta_{FC}(t), \tag{3.37c}$$

$$P^{min}_{Elz}\Delta_{Elz}(t)\leq P_{Elz}(t)\leq P^{max}_{Elz}\Delta_{Elz}(t), \tag{3.37d}$$

$$P_{FC}(t)\leq P^{max}_{FC}(1-\Gamma^{off}_{Elz}(t-\Delta T)), \tag{3.37e}$$

$$P_{FC}(t)\leq P^{max}_{FC}(1-\Gamma^{off}_{Elz}(t)), \tag{3.37f}$$

in which Eqs. (3.37a) to (3.37d) represent the power limitation across the URFC and its switching states, while Eqs. (3.37e) and (3.37f) denote the standby constraints for the URFC when switching from the electrolyzer to the FC.

To describe the working state of the hydrogen storage tank, the pressure of tank (POT) is considered according to the Ideal Gas Law as follows:

$$\rho_{Elz}=\left(\Delta T\frac{P_{Elz}\eta_{Elz}}{3.55\times\mathcal{V}_m}RT_k\right)\mathcal{V}_T, \tag{3.38}$$

where $\mathcal{V}_m$ represent molar volume of gas, 22.4L/mol, $\mathcal{V}_T$ is the volume of the hydrogen tank, R and T_k denote the gas constant, 8.314J/(mol·K) and temperature in Kelvin, respectively. The term $P_{Elz}\cdot\eta_{Elz}/3.55$ indicates the volume of hydrogen that can be produced by the corresponding power of the electrolyzer after considering hydrogen production efficiency and specific data, as mentioned in [116].

The working efficiency of the electrolyzer and changes dynamically with power fluctuations, impacting the economy of the system. Therefore, the power and efficiency curves are linearized as affine functions based on real experiment results, as given in Eqs. (3.39a) to (3.39c). Pressure conditions of the hydrogen tank, upper and lower limits, and equality of the pressure at time terminals during optimized horizon constraints are represented in Eqs. (3.39d) to (3.39f).

$$\eta_{Elz} = \left(P_{Elz} - P_{Elz,r}\right) k_{\eta,Elz} + \eta_{Elz,r}, \tag{3.39a}$$

$$\rho_{FC} = \frac{1}{\eta_{FC}} P_{FC} \times \rho_{FC,r}, \tag{3.39b}$$

$$\eta_{FC} = \left(P_{FC} - P_{FC,r}\right) k_{\eta,FC} + \eta_{FC,r}, \tag{3.39c}$$

$$POT\left(t\right) = POT\left(t - \Delta T\right) + \rho_{Elz} - \rho_{FC}, \tag{3.39d}$$

$$POT_{min} \leq POT\left(t\right) \leq POT_{max}, \tag{3.39e}$$

$$POT\left(1\right) = POT\left(T\right). \tag{3.39f}$$

3.2.3.4 Design of battery energy storage system

The aggregated cost function for battery installation and degradation costs is formulated as follows:

$$\mathcal{C}_b\left(t\right) = \frac{1}{2 \times DoD}\left(\zeta_b E_r P_b^{char}\left(t\right) \Delta T\right) + \mathcal{C}_b^{deg}\left(P_b^{char^2}\left(t\right) + P_b^{dis^2}\left(t\right)\right), \tag{3.40}$$

where $\zeta_b = \mathcal{C}_b^{Ins} / \mathcal{L}_b$, while $\mathcal{C}_b$ denotes the overall cost of the battery, with $\mathcal{C}_b^{Ins}$ and $\mathcal{C}_b^{deg}$ denoting the installation and degradation costs of the battery, respectively, while DOD indicates the Depth of Discharge rate of the battery.

The battery works as a voltage source due to its fast response speed. Therefore, the charge and discharge power of the battery, as well as its capacity, are subject to security constraints to ensure enough margin to react during emergencies. This security constraint can be expressed as follows:

$$\mathcal{S}_b\left(t\right) = \xi_b^{pow}\left(P_b\left(t\right) - \frac{1}{2}\left(P_b^{max} - P_b^{min}\right)\right)^2 + \xi_b^{cap}\left(SOC\left(t\right) - SOC^{ref}\right)^2, \tag{3.41}$$

where $\mathcal{S}_b(t)$ represents the security constraint for the battery, formulated by considering

both the maximum power P_b^{max} and minimum power P_b^{min} of the battery, along with its reference state of charge SOC^{ref}. The power limitations and security constraints of battery charging and discharging are considered as follows:

$$SOC(t) = SOC(t-\Delta T) + \frac{\Delta T}{E_r} \times \left(P_b^{char}(t) \cdot \eta_{char} - P_b^{dis}(t) \cdot \eta_{dis} \right), \tag{3.42a}$$

$$P_b(t) = P_b^{dis}(t) - P_b^{char}(t), \tag{3.42b}$$

$$\Delta_b^{char}(t) + \Delta_b^{dis}(t) \leq 1, \tag{3.42c}$$

$$0 \leq P_b^{char}(t) \leq P_b^{max} \cdot \Delta_b^{char}(t), \tag{3.42d}$$

$$0 \leq P_b^{dis}(t) \leq -P_b^{min} \cdot \Delta_b^{dis}(t), \tag{3.42e}$$

$$SOC_{min} \leq SOC(t) \leq SOC_{max}, \tag{3.42f}$$

$$SOC(1) = SOC(T). \tag{3.42g}$$

in which Eq. (3.42a) represents the battery SOC conditions. Eqs. (3.42b) to (3.42e) denote the limitation on the upper and lower power of the battery, and ensure that the battery cannot charge and discharge simultaneously. Eqs. (3.42f) and (3.42g) indicate the upper and lower limits of battery capacity and the balance between the charging and discharging operations of the battery.

3.2.3.5 Design of N-1 principle of the system

In this study, ensuring the security of islanded microgrids is crucial. We incorporate the N-1 principle as mentioned in [117], as a constraint to guarantee that the secure power supply of the microgrid remains unaffected in the event of any DERs existing due to failures. It is important to note that islanded microgrid exits due to failures. It is worth noting that only VSC has the ability to dynamically participate in power compensation when N-1 events occur. Therefore, the constraints are expressed as follows:

$$\sum_{vs \in \mathcal{V} \setminus u} \left(P_{vs}^{max} - P_{vs}(t) \right) \geq P_u(t), \tag{3.43a}$$

$$\sum_{vs \in \mathcal{V} \setminus u} \left(P_{vs}(t) - P_{vs}^{min} \right) \geq -P_u(t), \tag{3.43b}$$

where $u \in \{\mathcal{V} \cup \mathcal{C}\}$ indicates the unit that is out of operation due to a fault or other reasons. Eqs. (3.43a) and (3.43b) describe the security constraints when they are cut off as power generation units or power supply units, respectively. Finally, to ensure the smooth operation of the proposed centralized hierarchical control framework while meeting the load demands, the power balance equation is expressed as follows:

$$P_l(t) = P_{urfc}(t) + P_{Dies}(t) + P_b(t) + P_{pv}(t). \tag{3.44}$$

Remark: The EMS optimization results in this subsection will be sent to the primary control layer control loop and secondary control layer, as shown in Fig. 3.10, and are used in Eqs. (3.25a) and (3.27).

Table 3.3: Parametric data about diesel generator and BESS

Energy Sources	**Parameters**						
Diesel Generator	P_{Dies}^{max}	P_{Dies}^{min}	P_{Dies}^{RU}	P_{Dies}^{RD}	b_o	b_1	b_2
	17kW	2kW	4kW	-4kW	0.3	0.6	0.04
Battery Storage	P_b^{max}	P_b^{min}	E_r	η_b	L_b	SOC_{max}	SOC_{min}
	11kW	-11kW	11kWh	95%	3000 cycles	0.8	0.2

Table 3.4: Parametric data about URFC (Fuel cell and Electrolyzer)

Energy Sources	**Parameters**								
Fuel cell	P_{FC}^{max}	P_{FC}^{min}	$P_{FC,r}$	$\eta_{FC,r}$	$\rho_{FC,r}$	$k_{\eta,FC}$	$\mathcal{L}_{H_2}$	$\mathcal{V}_T$	
	8kW	3kW	3.9kW	0.8	140kpa	$0.068e^{-3}$	60kWh	0.01m^3	
Electrolyzer	P_{Elz}^{max}	P_{Elz}^{min}	$P_{Elz,r}$	POT_{max}	POT_{min}	$\eta_{Elz,r}$	$k_{\eta,Elz}$	R	T_k
	20kW	4kW	9.5kW	1Mpa	1atm	0.875	$-0.0066e^{-3}$	8.314 J/(mol.K)	298K

3.2.4 Analysis of Simulation results and discussion

Following the full design and analysis of the problem formulation and the proposed hierarchical control methodology for frequency regulation, the results are presented and discussed. Tables 3.3 and 3.4 represent the main data about the DERs with hydrogen energy components (fuel cell and electrolyzer), respectively. Table. 3.5 presents the data about the islanded microgrid model under study and the weighting parameters that are chosen. The effectiveness of the proposed methodology has been evaluated by considering

Table 3.5: Data related to the microgrid and the weighting combinations

Categories	Description	Values
Parametric data of microgrid	Nominal frequency	f=50Hz
	Nominal voltage	V_m=311V, V_{rms}=220V
	LCL filters	R=0.1Ω, L=3.5mH, C=0.5μF
	Droop coefficients of P	$K_{dP,diesl}$=1e^{-5}, $K_{dP,bat}$=3e^{-5}
	Droop coefficients of Q	$K_{dQ,diesl}$1e^{-5}, $K_{dQ,bat}$=3e^{-5}
	Switching frequency	f_s=10kHz
Weighting combinations	$\alpha_{k,dies}$	10, 1, 1.5, 5, 1.5
	$\alpha_{k,bat}$	10, 1, 1.5, 5, 1.5

Matlab/Simulink. A Gurobi optimization solver, implemented via the YALMIP platform, is employed to solve the EMS-based optimization work.

This subsection demonstrates the simulation results of the proposed EMS approach. The EMS generates the references of the active and reactive power $(P_{vs}^{ref}, Q_{vs}^{ref})$ for both VSC and CSC, which are sent to the primary control and secondary control layers in the proposed hierarchical control framework. The sampling time Fig. 3.12 depicts the day-ahead prediction results of the PV and the load demands in the form of active power utilized in the EMS framework.

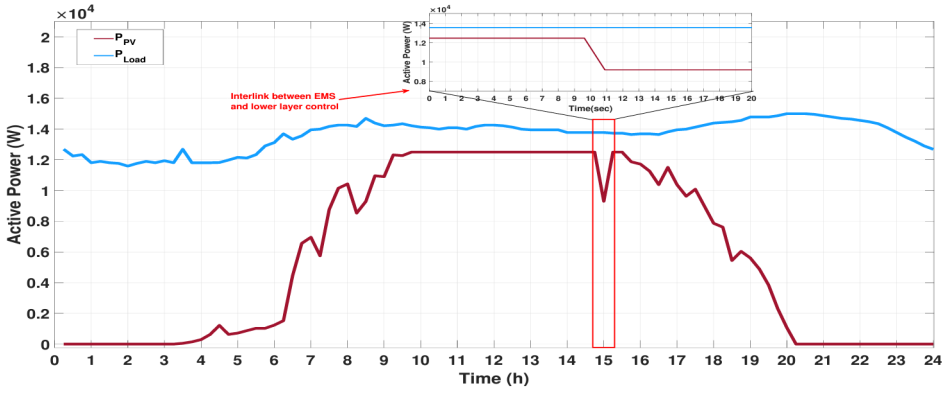

Figure 3.12: Prediction results of the P_{PV} and P_{Load}

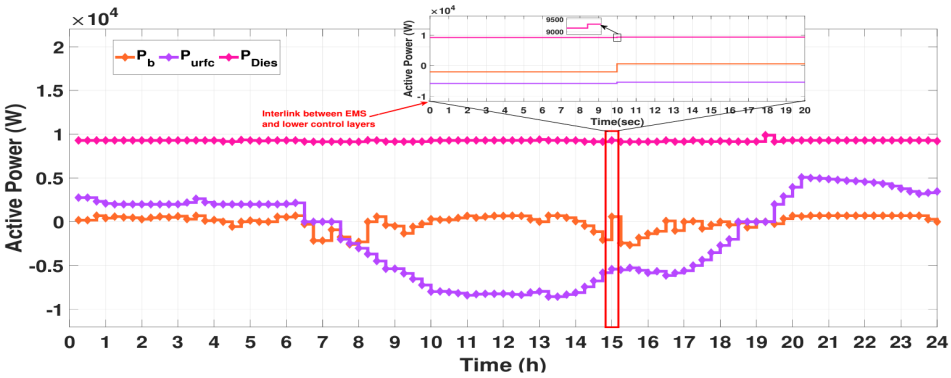

Figure 3.13: EMS dispatch results for the P_{Dies}, P_b and P_{urfc}

Furthermore, Fig. 3.13 shows the EMS based optimal dispatch results of P_{Dies}, P_b and P_{urfc}. Analysis of both figures, (Fig. 3.12 and Fig. 3.13) reveals that the EMS approach efficiently prioritizes the utilization of more power from the PV during the time interval of higher production of power from PV (5:30 AM to 19:30 PM). During this time, the URFC operates in electrolytic mode, storing hydrogen in a tank for use at night. From 19:30 PM to 5:00 AM, when there is no PV power production, the proposed EMS approach economically schedules the URFC in coordination with the battery to discharge and meet the load demands alongside the diesel generator, thereby reducing the overall operational cost in terms of both voltage sources and current sources.

It is worth mentioning that the simulation results illustrated in Fig. 3.13, show that the output power of the generator and the battery power are flattened within a certain power range, ensuring a sufficient power margin for emergencies. From these results, it can be analyzed that when the load and PV fluctuated, the BESS adjusted its output power more significantly than the diesel generator to achieve better economic benefits.

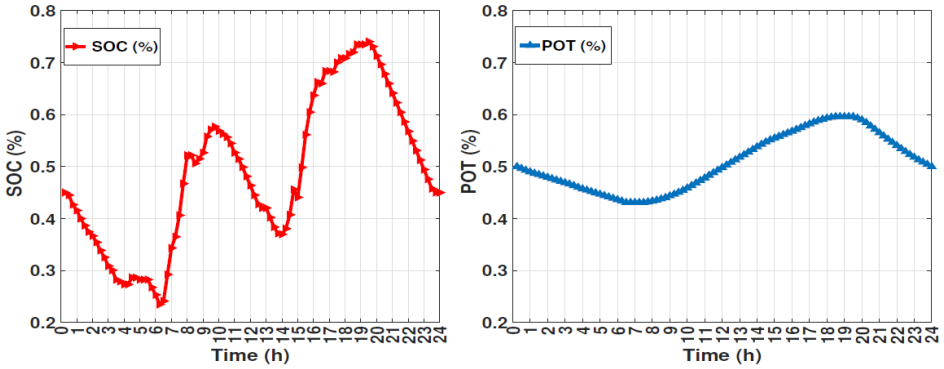

Figure 3.14: EMS results for the *SOC* and *POT*

Fig. 3.14 depicts the EMS-based optimized results of the pressure of tank (POT) and

SOC of the model under study. From Fig. 3.14, it can be observed that the optimized SOC results indicate that the proposed EMS approach efficiently operates by adhering to the constraints specified in Eqs. (3.42a) to (3.42f). This ensures better management of the battery charging and discharging cycles, thereby maintaining the battery life span and preventing the increased battery degradation costs from frequent cycling. Meanwhile, constrained by security considerations as outlined in Eq. (3.41), which incorporate the penalty factor of the battery SOC and power operation point, the battery does not reach the upper and lower limits as specified by Eq. (3.42f), thus providing additional margin to enhance the security.

Moreover, as shown in Fig. 3.14, the optimized POT results for the URFC demonstrate that the EMS-based optimization effectively manages POT while enhancing efficiency. This is achieved by satisfying the constraints specified in Eqs. (3.39a) to (3.39f). In terms of economic costs analysis, to consider the economic benefits from the EMS, we have considered the following costs C_b^{Ins} = 185$/kWh, C_{urfc}^{Ins} = 600$/kW, C_{urfc}^{SU} = 1.5$/kW, C_{urfc}^{SD} = 1.5$/kW and C_{urfc}^{flu} = 0.6$/kW for the proposed model under study.

3.2.5 Discussion on actual power dispatch from MPC

The MPC-based secondary control is proposed not only to enable the VSC to maintain the stability of the entire system while regulating the voltage and frequency of the system but also to accurately track the reference power from EMS under study according to different weight factors as specified in Eq. (3.27).

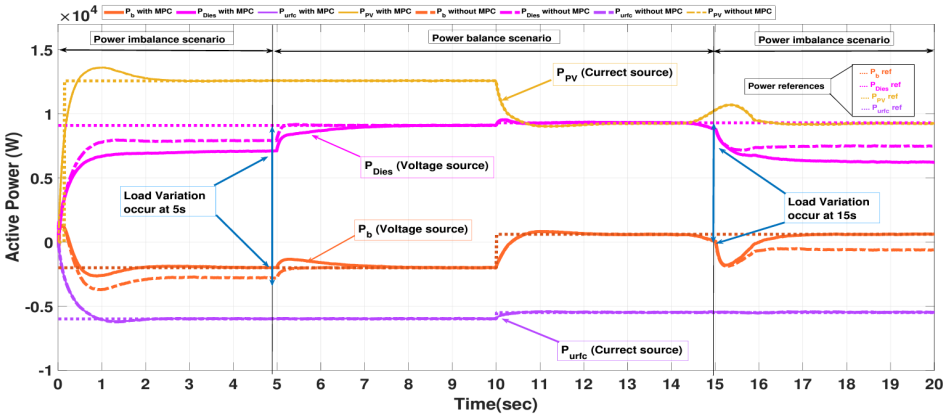

Figure 3.15: Results of the ω_{Dies} and ω_b with and without MPC consideration

Fig. 3.15 shows the actual control dispatch results of all the DERs, both with and without consideration of the MPC, and the comparison with the reference values. From

Fig. 3.15 it can be analyzed that the actual load demand in real-time, compared to the predicted value, considering two fluctuations at 5s and 15s over the simulation horizon. Over the 20-second simulation horizon, the actual power required by the system does not equal the predicted load demand from 0-5s and 15-20s (compare the zoomed-in window mentioned in Fig. 3.12 and the highlighted load variation areas in Fig. 3.15).

As demonstrated in Fig. 3.12, the PV fluctuated from 14s to 16s. Therefore, we simulated the EMS updating the reference value at 10 seconds to analyze the dynamic changes of the entire system under the control of EMS and MPC. As shown in Fig. 3.15, the CSC maintains accurate tracking of the power reference because, in this study, the current sources are considered to operate in grid-following mode with double-loop PI control. This enables URFC and PV to adhere to EMS instructions. The MPC in the secondary layer, which is employed for the VSC, successfully achieves frequency and voltage restoration. Among VSCs with MPC control, as shown in Fig. 3.15, the battery not only continuously tracks its active power even in power imbalance scenarios, but also dynamically adjusts its transient output power at 5s, 14s, and 15s when the PV and load power fluctuate due to the primary control layer behavior. On the other hand, the diesel generator with MPC control handles the steady-state power deviation during power imbalance scenarios as shown in Fig. 3.15, thus supporting the power balance in the islanded microgrid. This ensures the security, stability, and economic operation of the islanded microgrid.

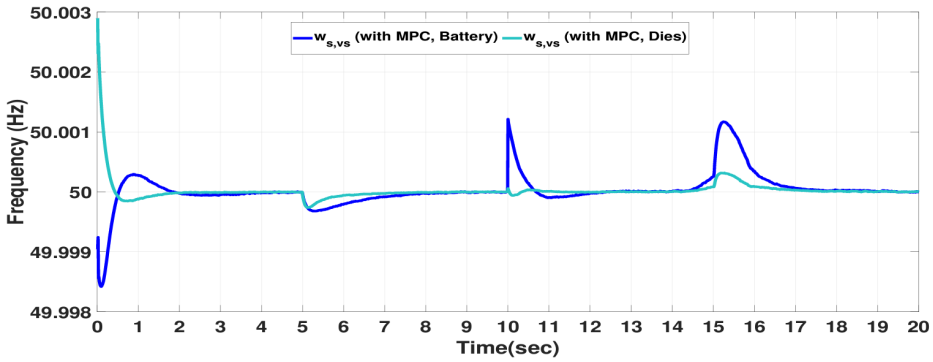

Figure 3.16: Results of the ω_{Dies} and ω_b with MPC consideration

Moreover, in the case without MPC consideration, as demonstrated by the results in Fig. 3.15, neither the diesel generator nor the battery can accurately follow the EMS scheduling instructions, rendering the EMS scheduling results meaningless. The system can still ensure the power balance under the control of the primary control layer, however, the security, capacity margin, and better economy of the power dispatch cannot be guaranteed.

In terms of frequency regulation, Fig. 3.16 compares the frequencies of the battery and the diesel generator in the proposed MPC scenario, where the stable state frequencies are both maintained at 50Hz. This proves that the proposed MPC-based secondary control layer strategy can compensate for the steady-state error. From the results, it can be analyzed that among both VSCs, the battery shows larger frequency control action when power fluctuations and reference values are updated. This is because MPC provides a large secondary control signal $\Delta\omega_s$ to maintain a significant power angle on the battery side VSC, ensuring EMS reference power tracking. In contrast, MPC imposes greater frequency stabilization requirements on the diesel generator, with its frequency curve exhibiting more robust frequency recovery.

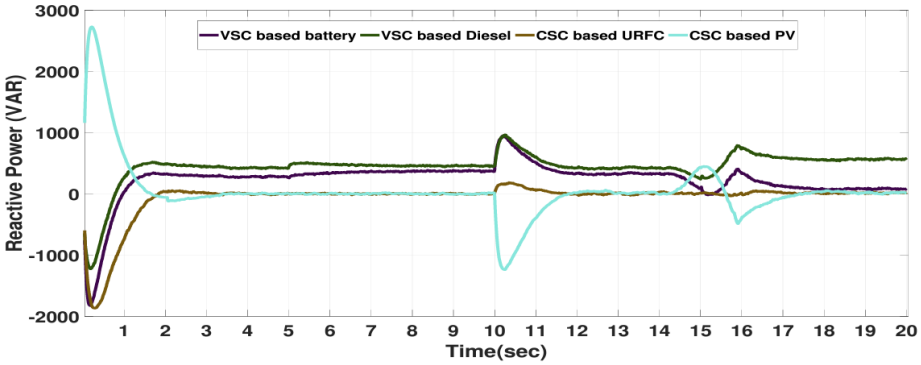

(a)

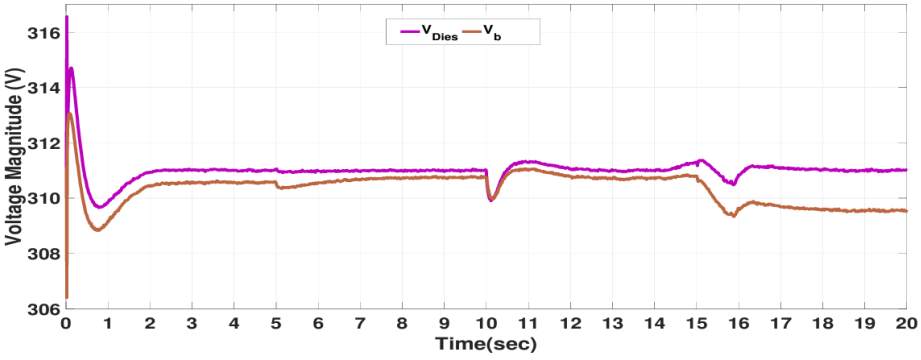

(b)

Figure 3.17: Results of VSC-based battery and diesel, and CSC-based URFC and PV

Fig. 3.17 (a) demonstrates the dynamic allocation curves of reactive power for DERs under the proposed control framework due to the involvement of power electronic control actions (VSCs and CSCs). The VSC distributes reactive power based on the droop control with the given reference value from EMS and supports the voltage of the islanded microgrid to improve the stability of the system. Fig. 3.17 (b) shows the voltage of VSC nodes under

the proposed methodology. From the voltage tracking result, it can be analyzed that the steady-state operating point of the diesel generator primarily equals the rated voltage under the proposed control architecture. The VSC node of the battery maintains a stable voltage difference from the rated voltage to ensure accurate power tracking.

3.3 Development of the modified Bolza optimal control approach and its applications in microgrid frequency regulation

The integration of RESs requires power converter control actions, such as enhanced grid-forming control in islanded MGs, to stabilize node voltages and frequency. However, as discussed in Section 3.2, the control actions of power converters within MGs, together with the presence of RESs and load variations, can lead to passive power fluctuations. These fluctuations may impact frequency and voltage regulation in the MG, potentially compromising the system's reliability and operational security. Although various studies in the literature propose converter-level optimization control for voltage and frequency regulation in MGs [118–121], these methods, while acceptable within certain limits, may not fully capture the actual system dynamics and could limit the scalability of control methodologies for similar challenges.

In this section, we formulate the novel modified Bolza problem with regularity and boundary conditions derived from the variational control problem to address complex power and frequency interactions in differential equations and to resolve issues related to passive control in grid-forming. We then examine its applications in MG frequency regulation.

The main contributions of this research work are;

- This research proposes a novel modified Bolza problem formulation that includes derivative terms in both the Hamiltonian functions and terminal constraints, making it suitable for optimizing control problems in power electronics.

- This study utilizes variational calculus to obtain a globally optimal solution. The regularity and boundary conditions for the proposed modified Bolza problem are defined and can be extended to other optimal control problems, including Pontryagin's principle, thereby expanding the range of potential applications.

- Furthermore, this study presents a methodology for developing an affine function substitution in the proposed case study, addressing the issue of initializing the multiplier at the start of the optimization process, while also simplifying the solution's dimensionality.
- To validate the performance of the proposed novel optimal control methodology, a MG with hybrid battery-hydrogen storage is applied, focusing on the frequency regulation of the system.

3.3.1 Problem Formulation

Consider a grid-forming droop control integrated with a secondary control for frequency recovery, as follows:

$$\Omega = \Omega_0 - K_D(P - P^{ref}) + \int_{t_0}^{t_q} (\Omega_0 - \Omega)dt, \tag{3.45}$$

which enables the distributed resources to operate as a voltage source. However, the lack of control inputs limits it to passive control. In some studies [122], variable droop coefficient regulation in primary control and rolling optimization strategies, such as MPC in secondary control, are employed to enhance frequency response and provide more flexible power scheduling for distributed power supplies. Now, consider adding a control signal u to form a controllable system, as follows:

$$\dot{\Omega}(t) = q\big(\Omega(t), \dot{P}(t), u\big) = \Omega_0 - \Omega - K_P\dot{P} + u. \tag{3.46}$$

In real-world applications, control behavior can become more complex, such as requiring the battery to maintain zero power output in a balanced power system during steady-state conditions. Alternatively, when tracking the power reference value provided by a higher-level energy management system, the control system may be reset, yet it can still be represented using a standard model as follows:

$$\mathcal{F}(\dot{x}(t), x(t), u, t) = \dot{x}(t) - q(\dot{x}(t), x(t), u, t) = 0, \tag{3.47}$$

where, $x \in R^v$, $u \in R^s$, $q \in J^s(R^v)$, $s \geq 1$.

In practical applications, our goal is to minimize transient fluctuations in both frequency and voltage. We also aim to minimize the deviation between active and reactive power and

their reference values. To achieve this, the proposed study formulates the system as an optimization problem and outlines a solution approach. Specifically, the model examined in this work is similar to the Bolza problem [123], as described in Eq. (3.48) and Eq. (3.49). However, the standard Bolza problem does not account for the inclusion of derivative terms in the Hamiltonian function. Thus, this paper introduces a modified version of the Bolza problem and demonstrates its validity through a case study. The general form of the Bolza problem, including the Hamiltonian function, is expressed as follows:

$$J = \varphi\big(x(t_q), t_q\big) + \int_{t_0}^{t_q} D[x(t), u(t), t]dt, \tag{3.48}$$

such that,

$$\dot{x}(t) = q\big(x(t), u(t), t\big). \tag{3.49}$$

3.3.2 Modified Bolza problem accessibility

Building on the original problem defined in Eqs. (3.50) and (3.51), we include the derivative term of the decision variable to formulate the modified Bolza problem as follows:

$$\begin{aligned} J &= \varphi\big(\dot{x}(t_q), x(t_q), t_q\big) + \int_{t_0}^{t_q} D\Big[\dot{x}, x, u, t\Big]dt, \\ s.t. \quad & \mathcal{F}\left(x(t), \dot{x}(t), u(t), t\right) = 0. \end{aligned} \tag{3.50}$$

where $\varphi, D \in R^s$, $x(t_0) = x_0$, and the ending $\dot{x}(t_q)$, $x(t_q)$ is met as mentioned below:

$$E\left(\dot{x}(t_q), x(t_q), t_q\right) = 0, \tag{3.51}$$

where $E \in R^a$, $a \leq q$.

Problem: Identify the optimal control u that minimizes $J = J_{min}$ as the system transitions from the initial state $x(t_0)$ to the final state $x(t_q)$.

The Lagrange multiplier method is used to formulate the unconstrained optimization problem, as described below:

$$J' = \varphi\big(\dot{x}(t_q), x(t_q), t_q\big) + \zeta^T E\left(\dot{x}(t_q), x(t_q), t_q\right) + \int_0^t \left\{ D\big[\dot{x}, x, u, t\big] + \sigma^T\left(q - \dot{x}\right) \right\} dt. \tag{3.52}$$

Let the Hamiltonian function H be defined as follows:

$$H[\dot{x},x,u,\sigma,t] = D[\dot{x},x,u,t] + \sigma^T q. \tag{3.53}$$

$$\begin{aligned}\Delta J' = {} & \Delta\dot{x}^T(t_q)\frac{\partial\varphi}{\partial\dot{x}(t_q)} + \Delta x^T(t_f)\frac{\partial\varphi}{\partial x(t_q)} + \Delta t_q\frac{\partial\varphi}{\partial t_q} \\ & + \Delta\dot{x}^T(t_q)\frac{\partial E^T}{\partial\dot{x}(t_f)}\mu + \Delta x^T(t_q)\frac{\partial E^T}{\partial x(t_q)}\zeta + \frac{\partial E^T}{\partial(t_q)}\zeta \\ & + \Delta\mu^T E + \int_{t_0}^{t_q}\left\{\Delta\dot{x}\frac{\partial H}{\partial\dot{x}} + \Delta x^T\frac{\partial H}{\partial x} + \Delta\sigma^T\frac{\partial H}{\partial x}\right. \\ & \left. + \Delta\mu^T\frac{\partial H}{\partial\mu} - \Delta\sigma^T\dot{x} - \Delta\dot{x}^T\lambda\right\}dt + H_{t_q}\delta t_f - \sigma^T(t_q) \\ & \times\dot{x}(t_f)\Delta t_q,\end{aligned} \tag{3.54}$$

where, $H_{t_q} = H(x(\dot{t_q}),x(t_q),u(t_q),\sigma(t_q),t_q)$, and

$$\dot{x}(t_q)t_q = x(t_q) - \Delta x\big|_{t_q}.$$

Proof of Remark 1: From Fig. 3.18, we observe that $BD = FC - UC$, where BD denotes the variation at time T, represented as $\Delta x\big|_{t_q}$. In this context, FC corresponds to the variation at the end point t_q, i.e., $\Delta x(t_q)$, which is the difference between the function values at the finishing terminal point. On the other hand, UC denotes the function's increment at time t_q, given by $\dot{x}(t_q)\Delta t_q$. Consequently, $\Delta x\big|_{t_q} = \Delta x(t_q) - \dot{x}(t_q)\Delta t_q$.

$$\begin{aligned}\Delta J' = {} & \Delta\dot{x}^T(t_q)\left\{\frac{\partial\varphi}{\partial\dot{x}(t_q)} + \frac{\partial E^T}{\partial\dot{x}(t_q)}\zeta\right\} + \delta x^T(t_q)\left\{\frac{\partial\varphi}{\partial x(t_q)}\right. \\ & \left. - \sigma(t_q) + \frac{\partial E^T}{\partial x(t_q)}\zeta\right\} + \Delta t_q\left\{\frac{\partial\varphi}{\partial t_q} + \frac{\partial E^T}{\partial t_q}\zeta + H_{t_q}\right\} \\ & + \Delta\zeta^T E + \int_{t_0}^{t_q}\left\{\left(-\Delta x^T\frac{d}{dt}\frac{\partial H}{\partial\dot{x}} + \Delta x^T\frac{\partial H}{\partial x} + \Delta x^T\right.\right. \\ & \left.\left.\times\dot{\sigma}\right) + \left(\delta\sigma^T\frac{\partial H}{\partial\sigma} - \Delta\sigma^T\dot{x}\right) + \delta\zeta^T\frac{\partial H}{\partial\zeta}\right\}dt + \Delta x^T \\ & \times\frac{\partial H}{\partial\dot{x}}\bigg|_{t_0}^{t_q} - \delta x^T\sigma\bigg|_{t_0}^{t_q} + \delta x^T\bigg|_{t_q}\sigma(t_q),\end{aligned} \tag{3.55}$$

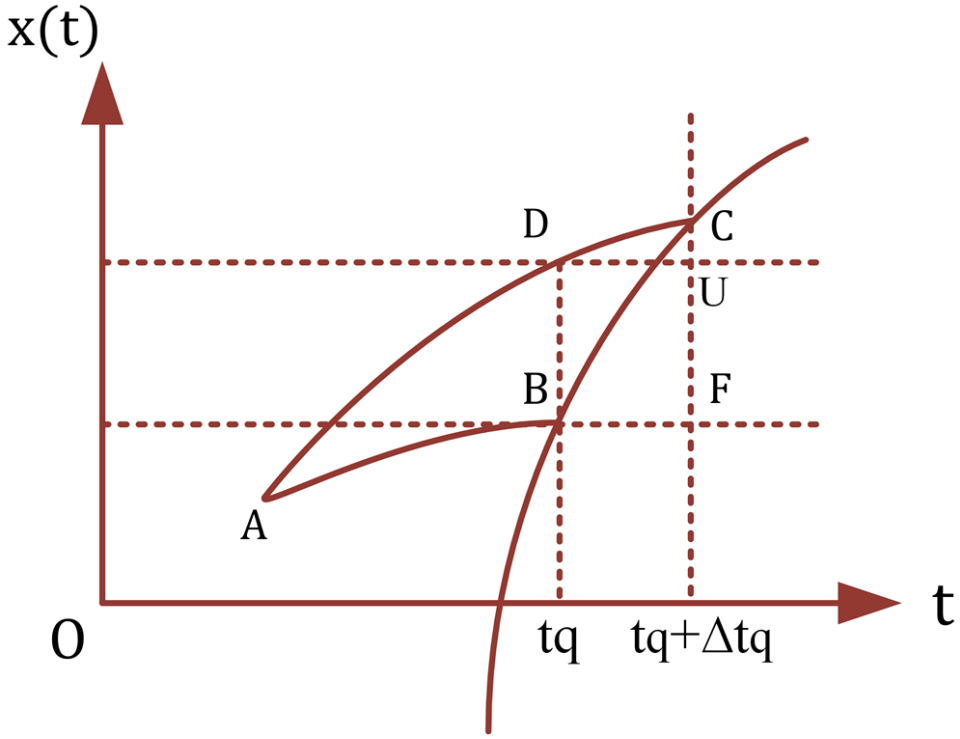

Figure 3.18: A graphical representation of the mathematical formulation

$$\begin{aligned}\Delta J' = {} & \Delta \dot{x}^T(t_q)\left\{\frac{\partial \Phi}{\partial \dot{x}(t_q)} + \frac{\partial E^T}{\partial \dot{x}(t_q)}\zeta\right\} + \Delta x^T(t_q)\left\{\frac{\partial \varphi}{\partial x(t_q)}\right. \\ & \left. - \sigma(t_q) + \frac{\partial E^T}{\partial x(t_f)}\zeta\right\} + \delta t_q\left\{\frac{\partial \varphi}{\partial t_q} + \frac{\partial E^T}{\partial t_f}\mu + H_{t_q}\right\} \\ & + \Delta\zeta^T E + \int_{t_0}^{t_q}\left\{\Delta x^T\left(\dot{\lambda} + \frac{\partial H}{\partial x} - \frac{D}{dt}\frac{\partial H}{\partial \dot{x}}\right) + \Delta\sigma^T\right. \\ & \left.\times\left(\frac{\partial H}{\partial \sigma} - \dot{x}\right) + \Delta u^T\frac{\partial H}{\partial u}\right\}dt + \left[\Delta x^T\frac{\partial H}{\partial \dot{x}}\right]_{t_0}^{t_f} + \Delta x^T\sigma\Big|_{t_0}. \end{aligned} \tag{3.56}$$

The canonical form of the proposed modified Bolza problem is presented below:

$$J' = \varphi\left[\dot{x}^T(t_q), x^T(t_q), t_q\right] + \zeta^T E\left[\dot{x}^T(t_q), x^T(t_q), t_q\right] + \int_{t_0}^{t_q}\left\{H - \sigma^T\dot{x}\right\}dt. \tag{3.57}$$

$$\Delta J' = \Delta \dot{x}^T(t_q)\left\{\frac{\partial \varphi}{\partial \dot{x}(t_q)} + \frac{\partial E^T}{\partial \dot{x}(t_q)}\zeta\right\} + \Delta x^T(t_q)\left\{\frac{\partial \varphi}{\partial x(t_q)} - \sigma(t_q) + \frac{\partial E^T}{\partial x(t_f)}\zeta + \frac{\partial H}{\partial \dot{x}(t_f)}\right\} + \Delta t_q\left\{\frac{\partial \varphi}{\partial t_q} + \frac{\partial E^T}{\partial t_q} \times \zeta + H_{t_q}\right\} + \Delta\zeta^T E + \int_{t_0}^{t_q}\left\{\Delta x^T\left(\dot{\sigma} + \frac{\partial H}{\partial x} - \frac{d}{dt} \times \left(\frac{\partial H}{\partial \dot{x}}\right) + \Delta\sigma^T\left(\frac{\partial H}{\partial \sigma} - \dot{x}\right) + \Delta u^T \frac{\partial H}{\partial u}\right\}dt + \left[\Delta x^T \times \sigma - \Delta x^T \frac{\partial H}{\partial \dot{x}}\right]_{t_0}, \tag{3.58}$$

Using Eq. (3.58), we establish the regularity and boundary conditions necessary for the objective function to achieve its minimum value, $\Delta J' = 0$, for arbitrary variations $\Delta x, \delta\sigma$, and Δu, as follows:

$$\begin{cases} \dot{\sigma} + \dfrac{\partial H}{\partial x} = \dfrac{d}{dt}\left(\dfrac{\partial H}{\partial \dot{x}}\right), \\ \dfrac{\partial H}{\partial \sigma} = \dot{x}, \\ \dfrac{\partial H}{\partial u} = 0, \end{cases} \tag{3.59a}$$

$$\begin{cases} x(t_0) = x_0, \\ \dfrac{\partial \varphi}{\partial \dot{x}(t_q)} + \dfrac{\partial E^T}{\partial \dot{x}(t_q)}\mu = 0, \\ E\left(\dot{x}(t_q), x(t_q), t_q\right) = 0, \\ \sigma(t_q) = \dfrac{\partial \varphi}{\partial x(t_q)} + \dfrac{\partial E^T}{\partial x(t_q)}\zeta + \dfrac{\partial H}{\partial \dot{x}(t_q)}, \end{cases} \tag{3.59b}$$

$$\left\{\frac{\partial \varphi}{\partial t_q} + \frac{\partial E^T}{\partial t_q}\zeta + H_{t_q} = 0, \right. \tag{3.59c}$$

Eq. (3.59a) presents the regularity condition for the modified Bolza problem, while Eqs. (3.59b) and (3.59c) define the boundary condition and the end time. This formulation provides a wider range of applications compared to the traditional Bolza problem and offers a more precise description of the problem.

3.3.3 A case study: Application of a modified Bolza problem for frequency regulation in a microgrid with integrated hybrid battery-hydrogen storage

The interaction between reference power tracking and frequency and voltage recovery in grid-forming converters is mutually dependent. This study examines battery control within a hydrogen-battery hybrid energy storage system, using it as a case study. The MG architecture and battery control hierarchy are illustrated in Fig. 3.19. In this system, the hydrogen FC acts as a virtual synchronous generator to handle steady-state loads, while the battery, governed by a droop controller, addresses transient loads, with both components operating under grid-forming control. The battery's fast response to power imbalances during transients, on the order of milliseconds, introduces an optimization challenge in balancing power offset with frequency recovery as load variations arise.

To address this challenge, this study proposes a hierarchical control system for energy storage batteries that incorporates power reference adjustments, load variations, and other practical considerations encountered in real-world applications.

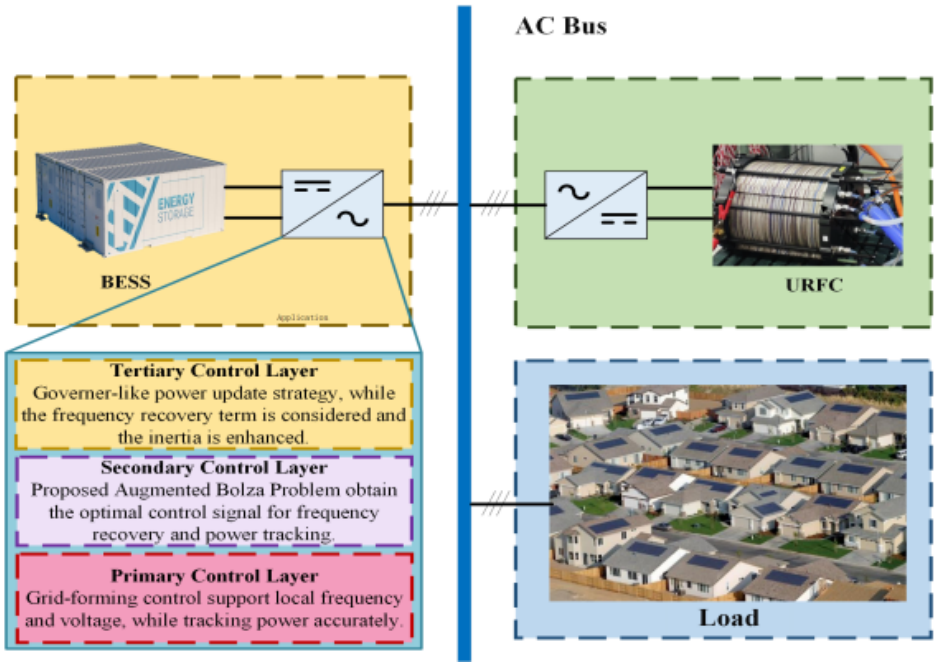

Figure 3.19: Architecture of the microgrid model under study

3.3.3.1 System constraints and functional performance

The control structure is illustrated in Fig. 3.20. At the primary level, grid-forming droop control is employed, while the optimized control signal u, obtained from the modified Bolza problem, is applied before determining the reference frequency. The modified Bolza problem collects real-time electrical data from the converter through secondary control to calculate the optimal control signal. Tertiary control is tasked with continuously updating the power reference values. Typically, tertiary control manages power optimization and scheduling over longer time horizons in discrete intervals based on day-ahead predictions. However, this paper concentrates on optimization within the differential equations that govern the system's dynamic behavior. By integrating a simple reference power update strategy into tertiary control, we implement a governor-like control, as described by the following equation:

$$P_{\beta}^{r} = P_{\beta}^{0} - k_D\left(k_p^w\left(\Omega^* - \Omega_0\right) + k_i^m \int_{t_0}^{t} \left(\Omega^* - \Omega_0\right) dt\right). \tag{3.60}$$

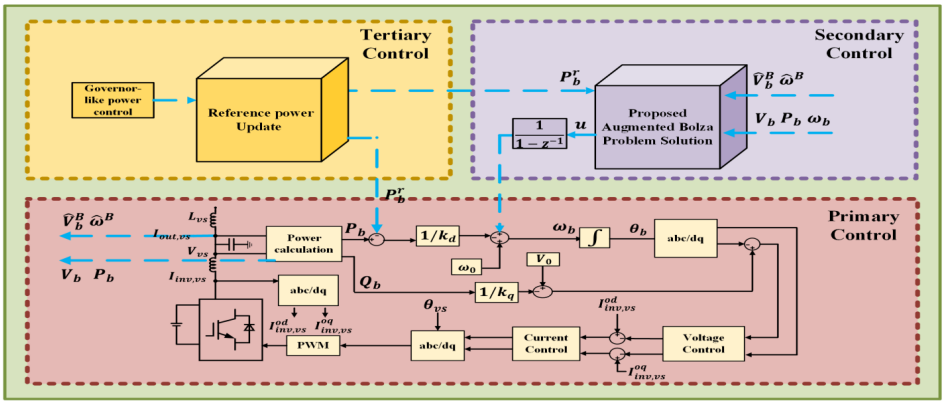

Figure 3.20: Hierarchical control diagram of storage units

In the lower layer, a grid-forming droop control integrated with an integral-type secondary control for power and frequency recovery is considered, with the addition of a

control signal u:

$$\Omega^* = \Omega_0 - \frac{1}{k_d}\left(P_\beta - P_\beta^r + k_i^{pow}\int_{t_0}^{t} P_\beta dt\right) + \int_{t_0}^{t} u dt; \tag{3.61a}$$

$$\begin{aligned}\omega^* = \Omega_0 - \frac{1}{k_d}\Bigg(& P_\beta + k_i^{pow}\int_{t_0}^{t} P_\beta dt - P_\beta^0 \\ & + k_d\left(k_p^m(\Omega^* - \Omega_0) + k_i^m\int_{t_0}^{t}(\Omega^* - \Omega_0)dt\right)\Bigg) + \int_{t_0}^{t} u dt;\end{aligned} \tag{3.61b}$$

$$\begin{aligned}\Omega^* - \Omega_0 = & -\frac{1}{k_D(1+k_p)}\left(P_\beta + k_i^{pow}\int_{t_0}^{t} P_\beta dt\right) \\ & - \frac{k_i^m}{(1+k_p^m)}\int_{t_0}^{t}\Big(\Omega^* - \Omega_o\Big)dt + \frac{\int_{t_0}^{t} u dt}{(1+k_p^m)}.\end{aligned} \tag{3.61c}$$

The predictive relationship model between active power and node frequency deviation [124] is expressed in the following equation, as

$$P_\beta = \mathcal{B} V_\beta \hat{V}_\beta^{\mathcal{B}} . \sin\left(\int_{t_0}^{t}\left(\Omega^*(t) - \hat{\Omega}^{\mathcal{B}}\right)dt\right). \tag{3.62}$$

To construct the modified Bolza problem, we make the following substitutions:

$$\int_{t_0}^{t}(\Omega^*(t) - \hat{\Omega}^{\mathcal{B}})dt = \overline{\Omega}^*; \tag{3.63a}$$

$$\int_{t_0}^{t} P_\beta(t)dt = \overline{P_\beta}. \tag{3.63b}$$

Hence, we have

$$\Omega^* - \Omega_o = \dot{\overline{\Omega}}^*(t) - (\Omega_0 - \hat{\Omega}^{\mathcal{B}}); \tag{3.64a}$$

$$P_\beta(t) = \dot{\overline{P_\beta}}(t). \tag{3.64b}$$

By substituting Eqs. (3.63a), (3.63b), (3.64a), and (3.64b) into Eqs. (3.61) and (3.62),

respectively, we can express the equations as follows:

$$\begin{aligned}\dot{\overline{\Omega}}^{*}(t) = &-\frac{1}{k_d(1+k_p^m)}\left(\mathcal{B}V_b\hat{V_b}^{\mathcal{B}}\sin(\overline{\omega}^{*}(t)) + k_i^{pow}\overline{P_\beta}(t)\right)\\ &-\frac{k_i^m}{(1+k_p^m)}\left(\Omega^{*}(t) - (t-t_0)(\Omega_0 - \hat{\Omega}^{\mathcal{B}})\right)\\ &+\frac{u}{(1+k_p^m)} + \left(\Omega_o - \hat{\Omega}^{\mathcal{B}}\right); \qquad (3.65a)\\ \dot{\overline{P_\beta}}(t) = &\mathcal{B}V_\beta\hat{V_\beta}^{B}\sin\left(\overline{\Omega}^{*}(t)\right). \qquad (3.65b)\end{aligned}$$

We replace Eqs. (3.65a) and (3.65b) with the following formulas to simplify the system

$$\begin{aligned}&\dot{X}_1 = \dot{\overline{\omega}}^{*}(t),\ \dot{X}_2 = \dot{\overline{P_b}}(t),\\ &A_1 = -\frac{1}{k_D(1+k_p^m)}\mathcal{B}V_\beta\hat{V_\beta}^{\mathcal{B}}, \mathcal{A}_2 = -\frac{k_i^{pow}}{k_D(1+k_p^w)},\\ &\mathcal{A}_3 = -\frac{k_i^m}{(1+k_p^m)},\ \mathcal{A}_4 = \frac{k_i^m}{(1+k_p^m)}(\Omega_0 - \hat{\Omega}^{\mathcal{B}}),\\ &\mathcal{A}_5 = \frac{1}{(1+k_p^m)},\ \mathcal{A}_6 = -\frac{k_i^m}{(1+k_p^m)}(\Omega_0 - \hat{\Omega}^{\mathcal{B}})t_0 + (\Omega_0 - \hat{\Omega}^{\mathcal{B}}),\\ &\mathcal{B}_1 = \mathcal{B}V_\beta\hat{V_\beta}^{\mathcal{B}}.\end{aligned}$$

Thus, we can express the state formulation in the form of constraints as follows;

$$\begin{aligned}\dot{X}_1 &= \mathcal{A}_1\sin X_1 + \mathcal{A}_2X_2 + \mathcal{A}_3X_1 + \mathcal{A}_4t + \mathcal{A}_5u + \mathcal{A}_6 = q_1; \qquad (3.66a)\\ \dot{X}_2 &= \mathcal{B}_1\sin X_1 = q_2. \qquad (3.66b)\end{aligned}$$

The objective function accounts for frequency and active power deviations, seeks to minimize control effort, and addresses the recovery time of the frequency, as described below:

$$J = \int_{t_0}^{t_q}\left(\mu_1P_\beta^2(t) + \mu_2\left(\Omega^{*}(t) - \Omega_0\right)^2 + \mu_3u^2\right)dt + \mu_4{t_q}^2. \qquad (3.67)$$

By substituting the replaced system variables $\dot{\bar{\omega}}$ and $\dot{\overline{P_\beta}}$ into Eq. (3.67), we obtain

$$J = \int_0^T \left(\mu_1 \overline{\dot{P}_\beta}^2(t) + \mu_2 \left[\dot{\bar{\omega}}^{2*}(t) + 2c_1 \dot{\bar{\omega}}^*\right] + \mu_2 c_1^2 + \mu_3 u^2\right) dt + \xi_4 {t_f}^2, \tag{3.68}$$

where $c_1 = \hat{\Omega}^{\mathcal{B}} - \Omega_0$ represents the frequency difference between the grid-forming converter and the connection node at each optimized time point.

In addition, extend Eq.(3.64) to a terminal condition, that is:

$$\dot{\bar{\Omega}}^*(t_q) - (\Omega_0 - \hat{\Omega}^{\mathcal{B}}) = 0. \tag{3.69}$$

Note that both Eqs. (3.68) and (3.69) contain derivative terms, which cannot be solved directly by the traditional Bolza problem or other optimization control methods.

3.3.3.2 Solution using modified Bolza Problem

The case study presents a problem with a derivative term in the objective function, which also appears in the Hamiltonian function. This requires solving it using the modified Bolza problem. The Hamiltonian function is defined as:

$$H = \mu_1 \dot{X}_2^2 + \mu_2 \left(\dot{X}_1^2 + 2c_1 \dot{X}_1\right) + \mu_2 c_1^2 + \sigma_1 q_1 + \sigma_2 q_2 + \mu_3 u^2. \tag{3.70}$$

According to the regularity condition given in Eq. (3.59), the optimal control can be obtained as follows:

$$\begin{cases} \dot{\sigma}_1 + \sigma_1 \dfrac{\partial q_1}{\partial X_1} + \sigma_2 \dfrac{\partial q_2}{\partial X_1} = \dfrac{d}{dt}(2\xi_2 \dot{X}_1 + 2\xi_2 c_1); \\ \dot{\sigma}_2 + \sigma_1 \dfrac{\partial q_1}{\partial X_2} + \sigma_2 \dfrac{\partial q_2}{\partial X_2} = \dfrac{d}{dt}(2\xi_1 \dot{X}_2); \\ \dot{X}_1 = q_1 = A_1 \sin X_1 + A_2 X_2 + A_3 X_1 + A_4 t + A_5 u + A_6; \\ \dot{X}_2 = q_2 = B_1 \sin X_1; \\ u = -\dfrac{\sigma_1 A_5}{2\mu_3}. \end{cases} \tag{3.71}$$

From Eq. (3.71), the optimal control signal can be determined by solving the corresponding set of equations, and this paper provides an example of solving such problems.

Given that the Hamiltonian function is linear with respect to the Lagrange multiplier, we can construct an affine function in terms of σ:

$$\begin{cases} q_1 = \dot{X}_1 = G_1 - a\sigma_1; \\ q_2 = \dot{X}_2 = G_2, \end{cases} \tag{3.72}$$

where, $G_1(x,t) = \mathcal{A}_1 \sin X_1 + \mathcal{A}_2 X_2 + \mathcal{A}_3 X_1 + \mathcal{A}_4 t + \mathcal{A}_6$, $a = \frac{{A_5}^2}{2\mu_3}$, while $G_2(x,t) = \mathcal{B}_1 \sin X_1$. Thus,

$$\begin{cases} (1+2a\mu_2)\dot{\sigma}_1 + \sigma_1 \dfrac{\partial G_1}{\partial X_1} + \sigma_2 \dfrac{\partial G_2}{\partial X_1} - 2\mu_2 \dot{G}_1 = 0; \\ \dot{\sigma}_2 + \sigma_1 \dfrac{\partial G_1}{\partial X_2} + \sigma_2 \dfrac{\partial G_2}{\partial X_2} - 2\mu_1 \dot{G}_2 = 0. \end{cases} \tag{3.73}$$

It is noted that

$$\dot{G}_1 = \frac{\partial G_1}{\partial X_1}\dot{X}_1 + \frac{\partial G_1}{\partial X_2}\dot{X}_2 + \frac{\partial G_1}{\partial t}, \tag{3.74a}$$

however,

$$\dot{G}_1 = \frac{\partial G_1}{\partial X_1}(G_1 - a\sigma_1) + \frac{\partial G_1}{\partial X_2} G_2 + \frac{\partial G_1}{\partial t}. \tag{3.74b}$$

similarly,

$$\dot{G}_2 = \frac{\partial G_2}{\partial X_1}\dot{X}_1 + \frac{\partial G_2}{\partial X_2}\dot{X}_2 + \frac{\partial G_2}{\partial t}, \tag{3.74c}$$

thus,

$$\dot{G}_2 = \frac{\partial G_2}{\partial X_2}(G_1 - a\sigma_1). \tag{3.74d}$$

By substituting Eq. (3.74) with Eq. (3.73), we get

$$\begin{aligned} \dot{\sigma}_1 = &-\frac{\partial G_1}{\partial X_1}\sigma_1 - \frac{1}{\beta}\frac{\partial G_2}{\partial X_1}\sigma_G + \frac{2}{\beta}\mu_2 \frac{\partial G_1}{\partial X_1} G_1 + \frac{2}{b}\mu_2 \frac{\partial G_1}{\partial X_2} G_2 \\ &+ \frac{2}{b}\mu_2 \frac{\partial G_1}{\partial t}; \end{aligned} \tag{3.75a}$$

$$\dot{\sigma}_2 = -\Big(\frac{\partial G_1}{\partial X_2} + 2\mu_1 a \frac{\partial g_2}{\partial X_1}\Big)\sigma_1 - \frac{\partial G_2}{\partial X_2}\sigma_2 + 2\mu_1 \frac{\partial G_2}{\partial X_1} G_1, \tag{3.75b}$$

where, $b = 1 + 2a\mu_2$. The above equations can be simplified to a state-space form as follows:

$$\dot{\sigma}_1 = \mathcal{A}_{11}\sigma_1 + \mathcal{A}_{12}\sigma_2 + \mathcal{B}_{11}; \tag{3.76a}$$

$$\dot{\sigma}_2 = \mathcal{A}_{21}\sigma_1 + \mathcal{A}_{22}\sigma_2 + \mathcal{B}_{21}; \tag{3.76b}$$

where,

$$\begin{cases} \dot{\sigma} = \mathcal{A}(x,t)\sigma + \mathcal{B}(x,t); \\ \mathcal{A}_{i,j} = \mathcal{A}_{i,j}(\mathcal{X}_1, \mathcal{X}_2, t) = \mathcal{A}_{i,j}(\mathcal{X}, t); \\ \mathcal{B}_{i,1} = \mathcal{B}_{i,1}(\mathcal{X}_1, \mathcal{X}_2, t) = \mathcal{B}_{i,1}(\mathcal{X}, t); \end{cases} \tag{3.77}$$

$x = (\mathcal{X}_1, \mathcal{X}_2)^T$. Thus,

$$\sigma(t) = e^{\int_{t_0}^{t} A(x(\tau),\tau)d\tau} C + \int_{t_0}^{t} e^{-\int_{t}^{s} \mathcal{A}(x(\tau),\tau)d\tau} \mathcal{B}(x(s),s)ds. \tag{3.78}$$

By substituting Eq. (3.78) into Eq. (3.71), we obtain an expression for the control variable u, at this point, the solution to the modified Bolza problem in this case study is complete.

Proof of Remark 2: The solution of the differential equations mentioned can be obtained using mathematical software such as Maple or MATLAB to drive the expression for the control input u. However, the initial condition of $\sigma(t_0)$ is unknown, which influences the outcome of the homogeneous solution. To address this issue, this paper introduces a method for constructing affine functions of decision variables $\mathcal{X}$. We further substitute Eq. (3.72) into Eq. (3.76) as follows:

$$\sigma_2 = \frac{1}{\mathcal{A}_{12}}(\mathcal{B}_{11} - \frac{\dot{g}_1 - \ddot{x}_1}{a} - \mathcal{A}_{11}\frac{G_1 - \dot{x}_1}{a}) \tag{3.79}$$

By Substituting Eq. (3.79) to Eq. (3.76) to derive the differential equation set that

includes only the state variable $\mathcal{X}$, we have

$$\begin{cases} -\frac{\dot{\mathcal{A}}_{12}}{{\mathcal{A}_{12}}^2}(\mathcal{B}_{11}-\frac{\dot{G}_1-\ddot{X}_1}{a}-\mathcal{A}_{11}\frac{G_1-\dot{A}_1}{a}) \\ +\frac{1}{\mathcal{A}_{12}}(\dot{\mathcal{B}}_{11}-\frac{\ddot{G}_1-\dddot{X}_1}{a}-\dot{\mathcal{A}}_{11}\frac{G_1-\dot{X}_1}{a}-A_{11}\frac{\dot{G}_1-\ddot{X}_1}{a}) \\ +\mathcal{A}_{21}\frac{G_1-\dot{X}_1}{a}+\frac{\mathcal{A}_{22}}{\mathcal{A}_{12}}(\mathcal{B}_{11}-\frac{\dot{G}_1-\ddot{X}_1}{a}-\mathcal{A}_{11}\frac{G_1-\dot{X}_1}{a}), \\ =\mathcal{B}_{21}, \\ \dot{X}_2=G_2. \end{cases} \tag{3.80}$$

This formula eliminates the need for the initial condition of σ and is transformed into an expression involving only the state variable $\mathcal{X}$, whose standard form is shown below:

$$\begin{cases} \dddot{X}_1=h(\ddot{X}_1,\dot{X}_1,X_1,X_2,t); \\ \dot{X}_2=G_2. \end{cases} \tag{3.81}$$

Thus, the constants C_1,C_2,C_3,C_4 can be determined by considering the initial value conditions and the ending time conditions shown below:

$$\begin{cases} X_1(0)=0,X_2(0)=0, \\ \dot{X}_1(t_q)=\Omega_0+\hat{\Omega}^{\mathcal{B}},\dot{X}_2(t_q)=0. \end{cases} \tag{3.82}$$

Finally, the model was implemented in Maple software, invoked from MATLAB, and the results were imported into Simulink for rolling optimization with a 0.1s sampling interval, to verify the feasibility of the proposed approach.

3.3.4 Results analysis and discussion

Following the design and analysis of the novel modified Bolza problem based on variational calculus, we examined the impact of the proposed optimal control methodology on the islanded microgrid to enhance the system's frequency regulation. Table.3.6 presents the data associated with the microgrid model under study, along with the weighting parameters. Additionally, three different weight combinations are designed to examine their effect on power tracking and frequency recovery optimization control. These combinations are substituted into Eq. (24), and the simulation results are displayed in Fig. 3.21. The three

Table 3.6: Data pertaining to the microgrid and the weighting factors

Categories	Description	Values
Parametric data of microgrid	Nominal frequency	f=50Hz
	Nominal voltage	V_m=311V, V_{rms}=220V
	LCL filters	R=0.1Ω, L=3.5mH, C=0.5μF
	Droop coefficients	K_D=1e^{-5}, K_Q=3e^{-5}
	Switching frequency	q_s=10kHz
Weighting combinations	case 0 (ρ0)	μ_1=0, μ_2=110, μ_3=8, μ_4=1
	case 1 (ρ1)	ξ_1=100$k_d{}^2$, ξ_2=100, ξ_3=8, ξ_4=3
	case 2 (ρ2)	μ_1=80$k_d{}^2$, μ_2=110, μ_3=58, μ_4=3
	case 3 (ρ3)	μ_1=110$k_d{}^2$, μ_2=110, μ_3=8, μ_4=3

optimization results offer distinct power scheduling strategies, each with corresponding frequency recovery capabilities. In the three cases, the frequency offset penalty weight coefficient in case 2 (C2) is the highest relative to the power offset, indicating a priority on frequency recovery. In contrast, case 3 (C3) focuses on ensuring the energy storage battery tracks the reference power, minimizing power fluctuations caused by grid-forming control.

Fig. 3.21 shows the optimal control signal, which reflects the level of frequency compensation provided by the modified Bolza problem from the secondary control side. This signal can be either positive or negative depending on the imbalance between power generation and load demand. From this figure, it can be analyzed that the signal curve at 1sec, the optimization target's weight influences the rate of change in the network-controlled node reference frequency. In other words, when the decision maker prioritizes power tracking over frequency recovery, the control signal intensifies frequency variations to minimize power fluctuations. Conversely, when the focus is on frequency recovery, the control signal slows the rate of change of frequency, enhancing the inertia and ensuring a more stable node frequency.

As shown in Fig. 3.22, under the optimal control derived from the Bolza problem, case

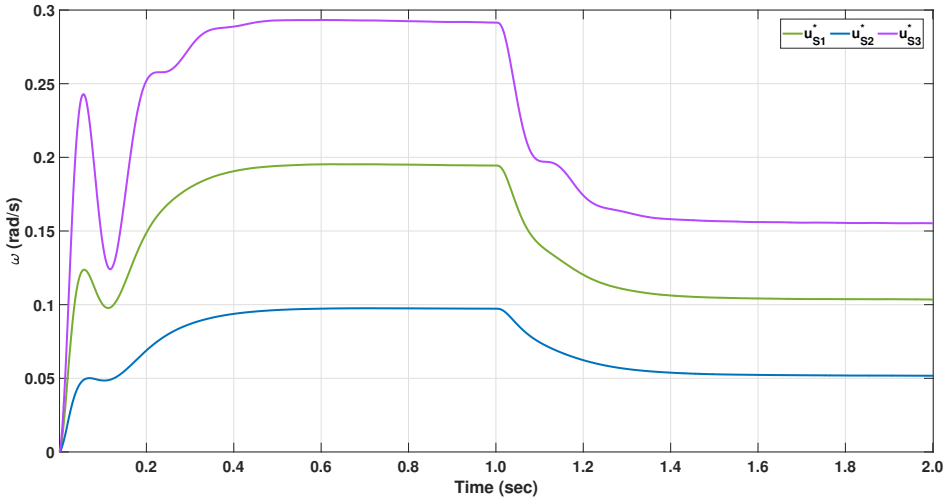

Figure 3.21: Patterns of the optimal control variable$u$

C2 demonstrates the smallest frequency fluctuation during load changes, although this results in a longer battery output recovery time. In contrast, case C3 exhibits the smallest output power deviation but experiences larger frequency fluctuations and significantly slower recovery. The weight coefficient in case 1 (C1) strikes a balance between C2 and C3, leading to a compromise in both the output power and frequency offset curves when compared to the simulation results of C2 and C3.

Figure 3.23 illustrates that the proposed modified Bolza problem effectively reduces frequency fluctuations caused by power imbalance. Additionally, the enforcement of terminal condition constraints enables the system to transition from power tracking to a steady state more quickly, compared to PI control. Finally, the simulation results demonstrate that the proposed modified Bolza problem is optimized by incorporating real-time converter parameters through secondary control, thereby transforming the original passive control system into an active optimal control system. This method achieves the optimal solution according to various predefined weightings. Therefore, it can be concluded that the proposed novel modified Bolza optimal control problem improved the microgrid's response while ensuring efficient frequency regulation of the MG in conjunction with the HESS.

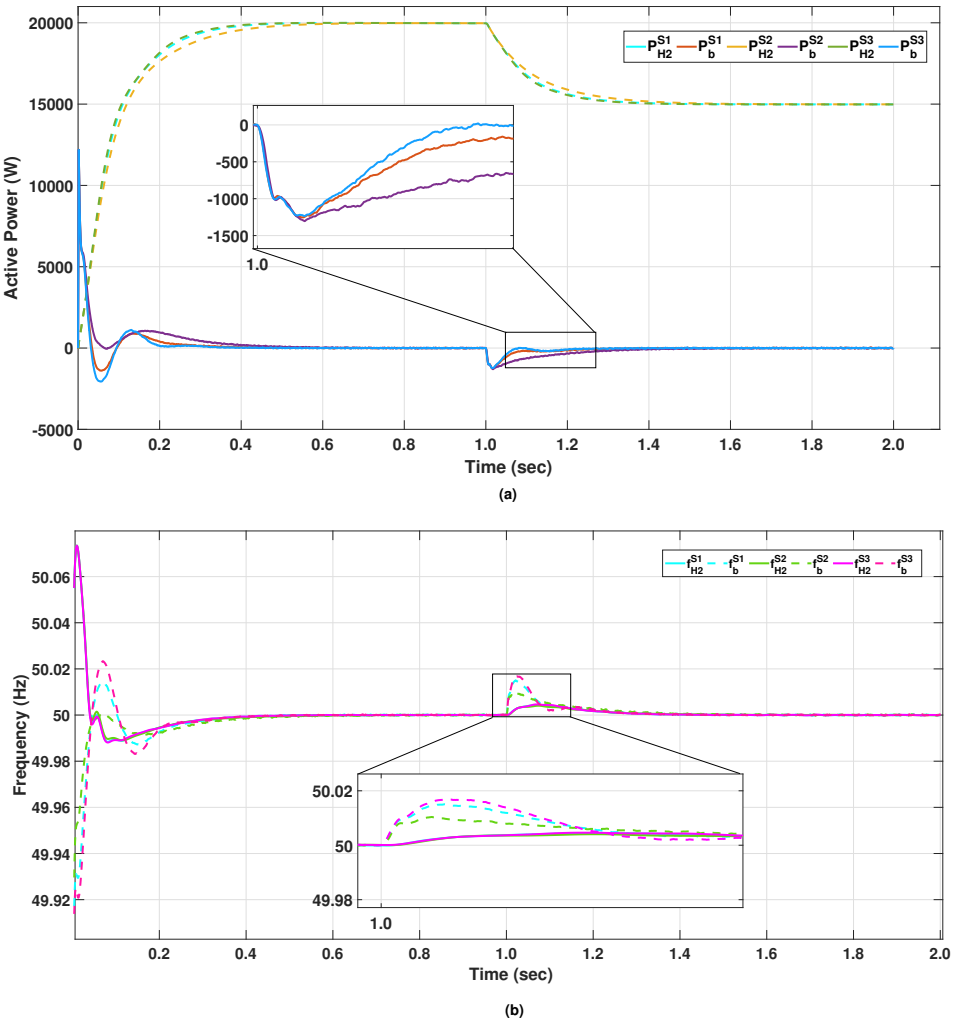

Figure 3.22: **(a)** Power tracking results **(b)** frequency regulation results, for the BESS and hydrogen.

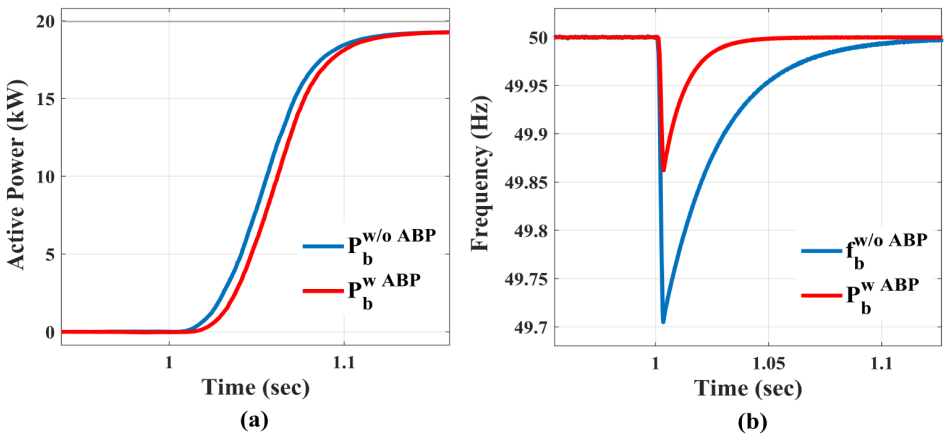

Figure 3.23: Patterns of the optimal control variable$u$

3.4 Design of a cost-effective controller for SI with DERs and testing through power hardware-in-the-loop simulations

This research focused on developing and testing a low-cost controller capable of autonomously measuring grid frequency, calculating frequency and rate of change of frequency (ROCOF), and implementing a Synthetic inertia (SI) control law on remotely controllable DERs [125]. As shown in Fig. 3.24, the controller was built using a Raspberry Pi 4 Model B single-board computer, programmed in Python, and equipped with an Analog to digital converter (ADC). The single-board computer also includes communication modules for USB, LAN, wireless, and Bluetooth, along with a 0-3.3 V General Purpose Input/Output (GPIO) interface for interaction with external devices.

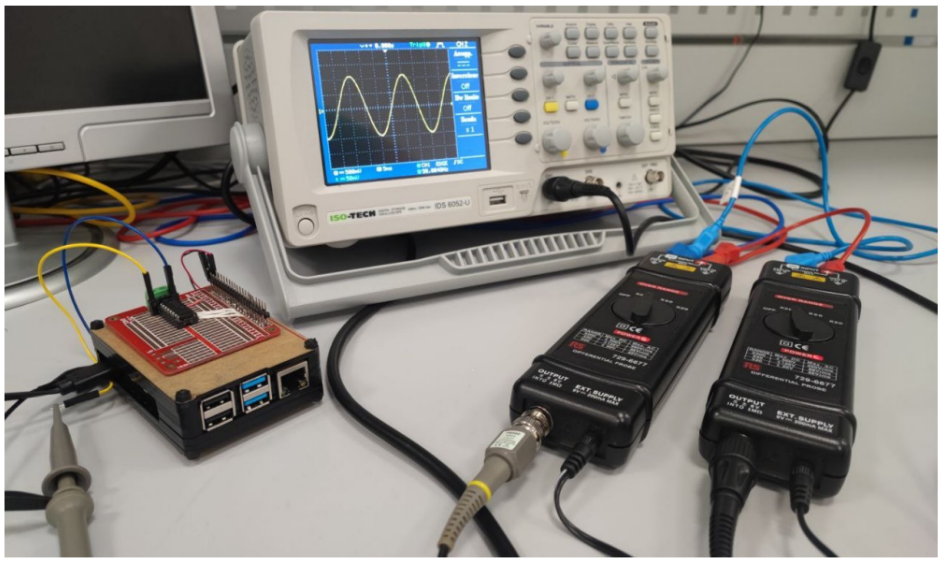

Figure 3.24: Frequency measurement test of the low-cost controller

The controller was designed to be a low-cost device (100 $) capable of implementing a Synthetic inertia (SI) control law on single-phase or three-phase remotely controllable DERs, without the need to modify their existing management systems. Fig. 5 shows the test bed architecture used to validate the SI controller.

Specifically, the blocks highlighted in green in Fig. 5 represent the key steps performed by the controller to generate the SI control action. The proposed controller acquires and samples a single-phase voltage waveform, which is first scaled by a transducer (e.g., 1/100). The ADC then converts the voltage into a 10-bit digital signal. The asynchronously

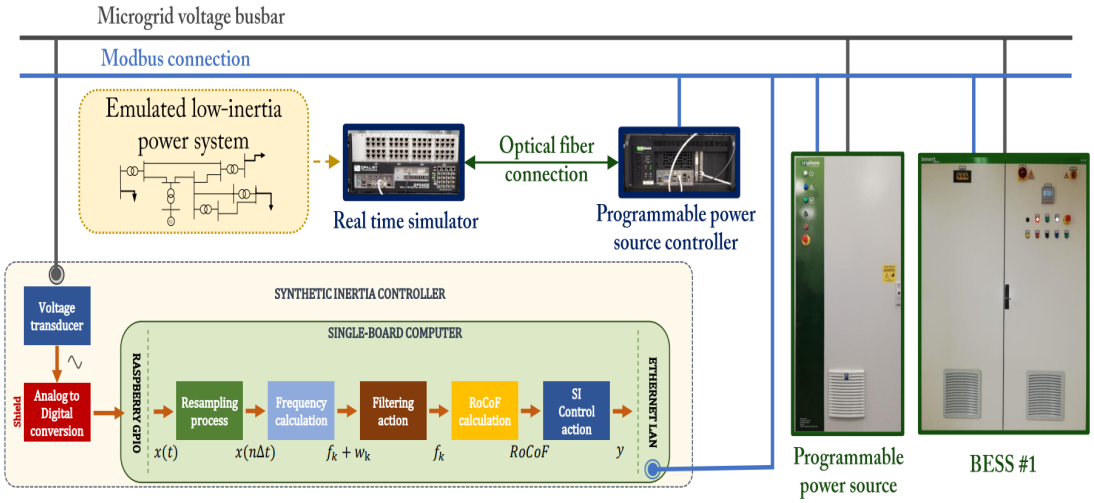

Figure 3.25: PHIL test set-up for the end-user controller validation

sampled data, $x(t)$, are sent to the single-board computer via the GPIO interface. These samples are resampled to create a regularly spaced signal, $x(t)$, necessary for running an autocorrelation algorithm that provides a fast and accurate frequency measurement. The proposed frequency measurement method requires two full waveforms (two cycles) for calculation. Once the voltage signal has been processed to obtain $f_k + w_k$, a moving average filter is applied to remove residual noise (w_k) from the frequency (f_k). Then, using two consecutive frequency samples, f_k and $f_k + 1$, the rate of ROCOF is calculated, and an SI control action (y), proportional to the ROCOF signal, is sent to the controlled DERs.

The PHIL tests conducted at LabZERO were used to evaluate the performance of the proposed controller and assess the impact of various design parameters, such as deadband, filter, gain, and reporting time. These tests were performed with the actual physical controller, which adjusted the active power setpoint of BESS 1. The setpoint was transmitted via mode bus TCP/IP to the battery management system (BMS) of the controllable BESS. As shown in Fig. 3.25, a real-time simulator emulated the electromechanical response of a low-inertia power system. The simulator calculated the time-varying frequency signal, which was applied to the microgrid through the programmable power source and its controller. Frequency excursions, caused by factors such as simulated contingencies or sudden load changes, were physically applied to both the BESS and the proposed controller. The controller then calculated the frequency and its derivative, generating an SI control law applied to the BMS of the BESS. The power exchanged between the BESS and the programmable power source was measured and sent back to the real-time simulator, allowing the response of the physical BESS to be included in the simulation.

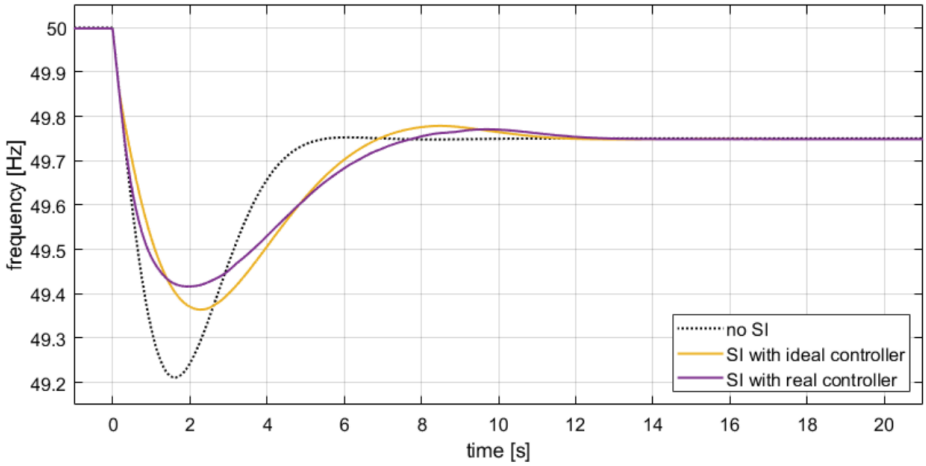

Figure 3.26: System frequency behavior with SI contribution by low-cost controller

The tests conducted, as described in [126], demonstrated the proposed controller's ability to provide accurate and rapid SI action, reducing ROCOF and frequency excursions during transients. For instance, Fig. 3.26 illustrates how the SI contribution from the BESS, controlled by the developed low-cost controller, improves frequency behavior after a load step disturbance. While the delays introduced by the entire measurement and control chain reduced the initial ROCOF reduction compared to an ideal frequency controller, the approach still resulted in a significant reduction in the nadir.

Chapter 4

Voltage Regulation

The integration of renewable energy sources (RESs), such as solar and wind, introduces voltage fluctuations due to their intermittent and variable nature, which can destabilize the voltage in Microgrid (MG)s. To maintain consistent voltage levels, advanced control techniques are required. In MG with multiple distributed energy resources (DERs) (e.g., batteries, fuel cells, photovoltaic (PV) systems), coordinating voltage control becomes complex, as each DERs has its own characteristics and control mechanisms that must be synchronized to prevent voltage imbalances. Additionally, the use of power electronics and inverters for voltage regulation presents challenges, including control delays, harmonics, and non-linearities, all of which can impact the quality of voltage regulation. Voltage regulation differs in grid-connected and islanded modes of operation: in islanded mode, the MG must be self-sufficient in maintaining voltage, while in grid-connected mode, it must harmonize with the external grid, which can affect voltage levels. Thus, achieving stable voltage regulation in MGs, particularly with hybrid systems involving various DERs, requires sophisticated control strategies capable of addressing dynamic power flow, network topology changes, and system disturbances [127–129].

Extending the main grid transmission lines to electrify remote rural areas is often not feasible due to high costs. As a more practical alternative, stand-alone MG, particularly those powered by renewable energy sources like solar and wind, offer a viable solution since these resources are abundant and environmentally friendly. This paper examines the implementation of DC-MGs for off-grid communities. DC-MGs are preferred for their efficient integration of various renewable generation units with DC outputs. Given the intermittent nature of renewable energy and the unpredictable demand profiles in islanded MG, a combination of energy storage systems and generation units is typically

used to ensure a continuous energy supply. However, this chapter introduces the electric spring—a smart demand-side management technique—as an alternative to traditional storage systems, aiming to enhance the flexibility of DC-MGs in managing the common bus voltage amid uncertainties. An adaptive droop control strategy is employed to ensure accurate power sharing among energy units and achieve effective voltage regulation, even under high-load conditions, while considering line impedances. This chapter discusses the voltage regulation of stand-alone DC-MGs with the implementation of electric springs alongside storage units.

4.1 Dcentralized control design

Voltage regulation in DC-MGs is crucial for maintaining system stability and ensuring the efficient operation of connected loads and distributed generations (DG) units. Accurate voltage control is required to prevent significant voltage fluctuations that could damage critical loads and disrupt system performance. As noted earlier, effective voltage regulation at the point of common coupling (PCC) ensures balanced power delivery between generation units and loads, which also helps extend the lifespan of end-user devices. In off-grid MG, which operates independently of the main grid, voltage regulation becomes even more challenging due to the intermittent nature of RESs and unpredictable load variations. The control system must quickly adjust to fluctuating power inputs and dynamic load demands, requiring effective algorithms. Therefore, a decentralized droop control strategy, which operates without relying on communication links, presents a viable solution for remote areas. The following subsections will present a modified decentralized droop-based algorithm that utilizes a non-linear curve for the droop gain (virtual resistance) rather than a linear approach. Fig. 4.1 depicts the schematic configuration of the ES integrated into an isolated DC-MGs.

4.1.1 Adaptive droop control design formulation

Conventional droop control defines the relationship between voltage and current for each unit with a straight decreasing line. This can be expressed mathematically as:

$$v_{ref}^{n} = V_{nom} - R_{dr}^{n}.I_{out}^{n}, \tag{4.1}$$

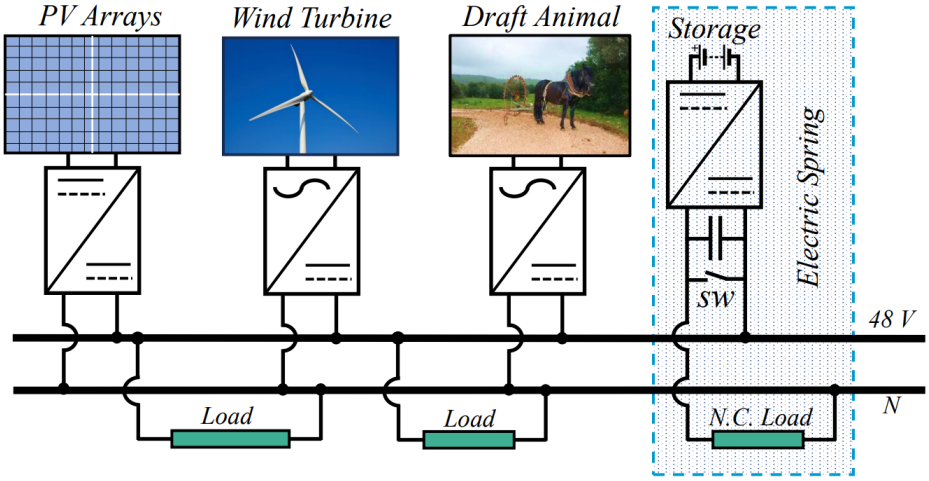

Figure 4.1: Schematic diagram of standalone DC MG, under study

where v^n_{ref}, R^n_{dr}, and I^n_{out} stand for the reference voltage, virtual resistance (droop gain), and the terminal current of the n-th unit, respectively. The V_{nom} is the DC-MGs nominal voltage. Not to mention that the value of R^n_{dr}, can be readily obtained, given that the utmost voltage drop must not fall below its permissible margin (i.e., V_{min}):

$$R^n_{dr} \leq \frac{V_{max}}{I^n_{nom}}, \; \Delta V_{max} = V_{nom} - V_{min} \tag{4.2}$$

where I^n_{nom} denotes the nominal current of the $n-th$ source.

To effectively evaluate the performance of a DC-MG, it is essential to consider such aspects as voltage regulation, accuracy in current sharing with respect to units' capability, the overall power dissipation (mainly arising from lines impedance), and the destabilizing impact of constant power loads (CPLs) on the system. The CPLs keep a fixed power even as the voltage changes (e.g., converter-based devices with power regulation techniques). It may also be worth mentioning that the stability challenge with CPLs stems from their negative incremental resistance [130].

These aspects have been explored in the literature [130–132], and the outcomes demonstrate that higher droop gains can result in more accurate current sharing and more effective mitigation of CPLs' destabilizing impact. Whereas, lower droop gains facilitate proper voltage adjustment and reduce power losses.

Considering the points mentioned above, it can be inferred that during light loadings, when the generation units' maximum capacity is significantly greater than the demand, the adverse impact of CPLs can be disregarded, and also, there is no serious concern

about the units' current contribution since they are well below their over-generation limits. Furthermore, as just stated, utilizing a small droop gain is well-suited for voltage regulation and minimizing power losses.

Turning to the opposite scenario, when demand approaches the maximum capacity of the generation units and there might be a meaningful contribution from CPLs, it is more prudent to choose a large droop gain. To conclude, it would be advisable to employ an adaptive droop curve rather than a straight line with a constant slope, in a way that its gain maintains small under light loads and increases gradually as the load grows. To do so, Eq. (4.1) can be redefined by adding a logarithmic term as follows:

$$v^n_{ref} = V_{nom} - R^n_{dr} \ln\left(1 + \left(\frac{I^n_{out}}{I^n_{nom}}\right)^{\alpha}\right) . I^n_{out} \tag{4.3}$$

In Eq. (4.3), α is a positive coefficient that specifies the position of the droop curve in the voltage versus current plane. This correlation is illustrated in Fig. 4.2. The value of the α coefficient for each unit depends on that unit's current contribution capacity and the impedance of the connection line. The rest of this subsection will focus on calculating this crucial quantity. As shown in Fig. 4.2, for the n-th unit and at each operating point, an equivalent droop gain (R^n_{eq}) can be defined as the slope of a tangent line to the curve.

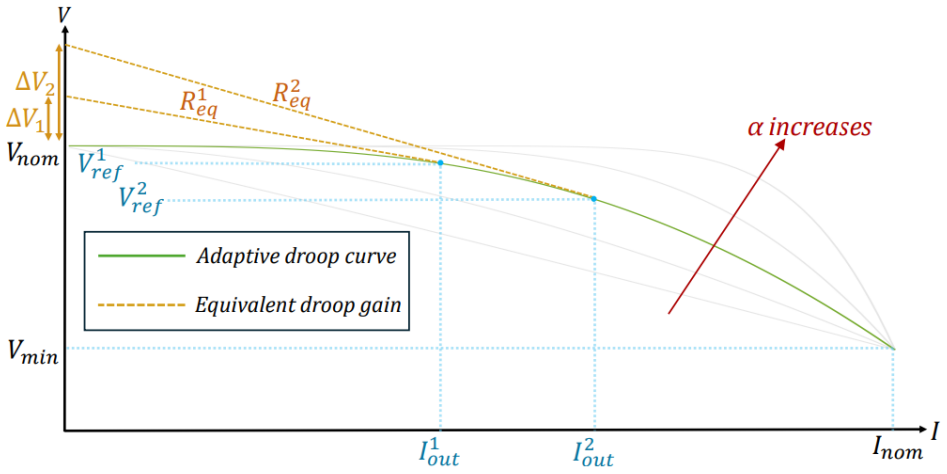

Figure 4.2: Schematic diagram of standalone DC MG, under study

$$R^n_{eq} = \frac{dv^n_{ref}}{dI^n_{out}} = -R^n_{dr}\left[\frac{\alpha\left(\frac{I^n_{out}}{I^n_{nom}}\right)^{\alpha}}{I^n_{nom}\left(1+\left(\frac{I^n_{out}}{I^n_{nom}}\right)^{\alpha}\right)} + \ln\left(1+\left(\frac{I^n_{out}}{I^n_{nom}}\right)^{\alpha}\right)\right] \tag{4.4}$$

Here, the negative sign solely denotes the descending slope. Referring to Fig. 4.2, at a specific loading condition, the intersection of the R^n_{eq} line with the voltage axis should indicate the required voltage shift ΔV_n to compensate for the voltage drop caused by line impedance, and consequently, ensure the PCC voltage close to its desirable value. Accordingly, based on the straight-line formula, this shift in the voltage can be estimated as follows:

$$\Delta V^n = R^n_{dr}.\left[\frac{\alpha\left(\frac{I^n_{out}}{I^n_{nom}}\right)^{\alpha}}{I^n_{nom}\left(1+\left(\frac{I^n_{out}}{I^n_{nom}}\right)^{\alpha}\right)}\right].I^n_{out} \tag{4.5}$$

Notably, the ΔV^n, which equals the voltage drop across the connecting line, reaches its maximum value during heavy loading periods, when the source's terminal current approaches its nominal value (i.e.,I^n_{out}=I^n_{nom}). Given this fact, the maximum equivalent droop gain ($R^n_{eq,max}$) could be determined as the slope of the tangent line at this operation point. After estimating the ($R^n_{eq,max}$), the α coefficient can be achieved from Eq. (4.4) considering the uppermost operating capacity of the $n-th$ unit (i.e., I^n_{out}=I^n_{nom}):

$$\alpha = \left(\frac{R^n_{eq,max}}{R^n_{dr}} - \ln(2)\right).2.I^n_{nom} \tag{4.6}$$

4.1.2 Voltage Regulation

Fig. 4.3 illustrates the block diagram of the proposed control scheme for the DC-MGs units (i.e., DGs and ES), based on the equations discussed above. As shown in the figure, the terminal voltages of the units are regulated using an inner current controller and an outer voltage controller. The proposed method determines the reference voltage (v_{ref}) for the outer voltage control loop, as given in Eq. (4.3), under various loading conditions. In over-current situations, the PI controller attempts to adjust the terminal voltage by increasing its output, which could result in saturation. To prevent this, an anti-windup mechanism, based on [133], is implemented to release the controller and avoid saturation.

The control mechanism of the adaptive algorithm consists of two stages. In the first stage, the method is applied to the DG units to automatically regulate the PCC voltage while ensuring accurate current sharing among the DGs, serving as the primary control for the DC microgrid. In the second stage, if the DGs generation capacity is insufficient to meet the demand and the voltage deviation at the common bus exceeds the permissible margin, the ES is activated to meet the requirements using the same adaptive control method. The

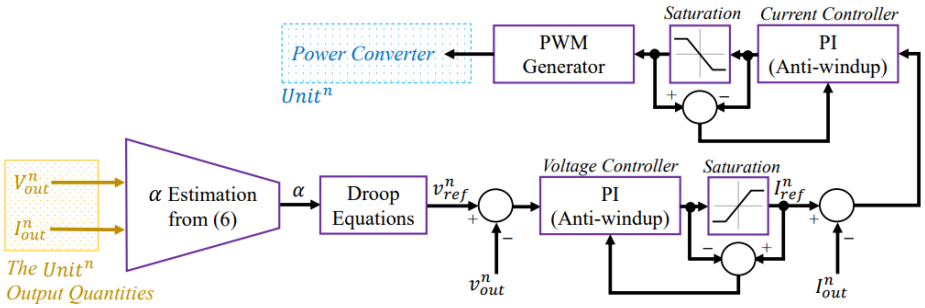

Figure 4.3: Control diagram of unit's power converter

Table 4.1: Characteristics of the test DC-microgrid

Parameters	**Symbol**	**Values**
Nominal voltage	V_{nom}	f=50Hz
Min. Permissible Voltage	V_{nom}	V_m=311V, V_{rms}=220V
Nominal current (DG_1, DG_2 & DG_3)	(I_{nom})	8A, 8A , 5A
Nominal current (ES)	(I_{nom})	12A
Line resistance (DG_1, DG_2 & DG_3)	(R_{dg1}, R_{dg2}, R_{dg3})	0.15Ω, 0.3Ω , 0.3Ω
Total resistive constant loads	R_l,	50Ω

main system parameters are listed in Table. 4.1, which also notes a permissible voltage deviation of 5%. This mechanism will be further discussed in the following section.

In this study on voltage regulation for standalone DC-MGs, the proposed scheme's performance is evaluated using the test DC-MGs shown in Fig. 4.1, simulated within the MATLAB® environment. The setup includes three distributed generation (DG) units: DG1 and DG2 represent two solar arrays with identical power ratings, while DG3 simulates a small wind turbine. As outlined in the Introduction, the ES system uses a half-bridge inverter, with its key characteristics provided in Table. 4.2.

4.1.3 Performance analysis of the proposed methodology

This proposed study compares two approaches: 1) the proposed adaptive droop control scheme, and 2) conventional droop control with a constant virtual resistor. To facilitate

Table 4.2: Characteristics of the electric spring

Parameters	Symbol	Values
Resistive non-critical loads	R_{nc},	15.6Ω
Switching frequency	f_{sw}	$25kHz$
Inverter circuit topology	type	Half-bridge
Output low-pass filter inductance	L_f	$25kHz$
Output low-pass filter capacitance	C_f	$140\mu F$

the comparison, two different modes for the conventional droop control are considered: one with low gains (0.3 for DG1 and DG2, 0.4 for DG3, and 0.2 for ES) and another with high gains (3 for DG1 and DG2, 4 for DG3, and 2 for ES). To verify the effectiveness of the proposed method, an intermittent step pattern is applied, assuming the demand profile stays within the DG generation capacity. In other words, it is assumed that the DG units do not experience an overload condition (i.e., $I^n_{out} \leq I^n_{nom}$). Using the proposed method, the terminal currents and voltages of the units at various loading levels are shown in Fig. 4.4, demonstrating a fast response to step changes while keeping voltage deviations within permissible limits. Additionally, the current is effectively shared among the DGs at both low and high loading levels, proportional to a fraction of their nominal currents. As shown in Fig. 4.4, the ES remains deactivated since the terminal voltages are above the permissible voltage drop. A similar scenario was tested using conventional droop control with low virtual resistances. The resulting output currents and voltages for this control scheme are shown in Fig. 4.5. This figure reveals that, at various loading levels, the voltage fluctuates above acceptable limits, and the current-sharing accuracy is sub-optimal. Notably, there is a discrepancy between the output currents of DG1 and DG2, despite their identical nominal values (as shown in Table. 4.1).

In contrast to the previous scenario, as shown in Fig. 4.6, using high virtual resistances in the conventional droop method significantly improves current-sharing accuracy. However, this improvement comes at the cost of exceeding permissible voltage limits, which activates the ES. Despite the ES activation, as indicated by Eq. 4.1, the high droop gain causes a substantial deviation of the reference voltage (v_{ref}) preventing effective voltage (v_{nom}) adjustment by the ES. Additionally, it is notable that ES activation in this scenario

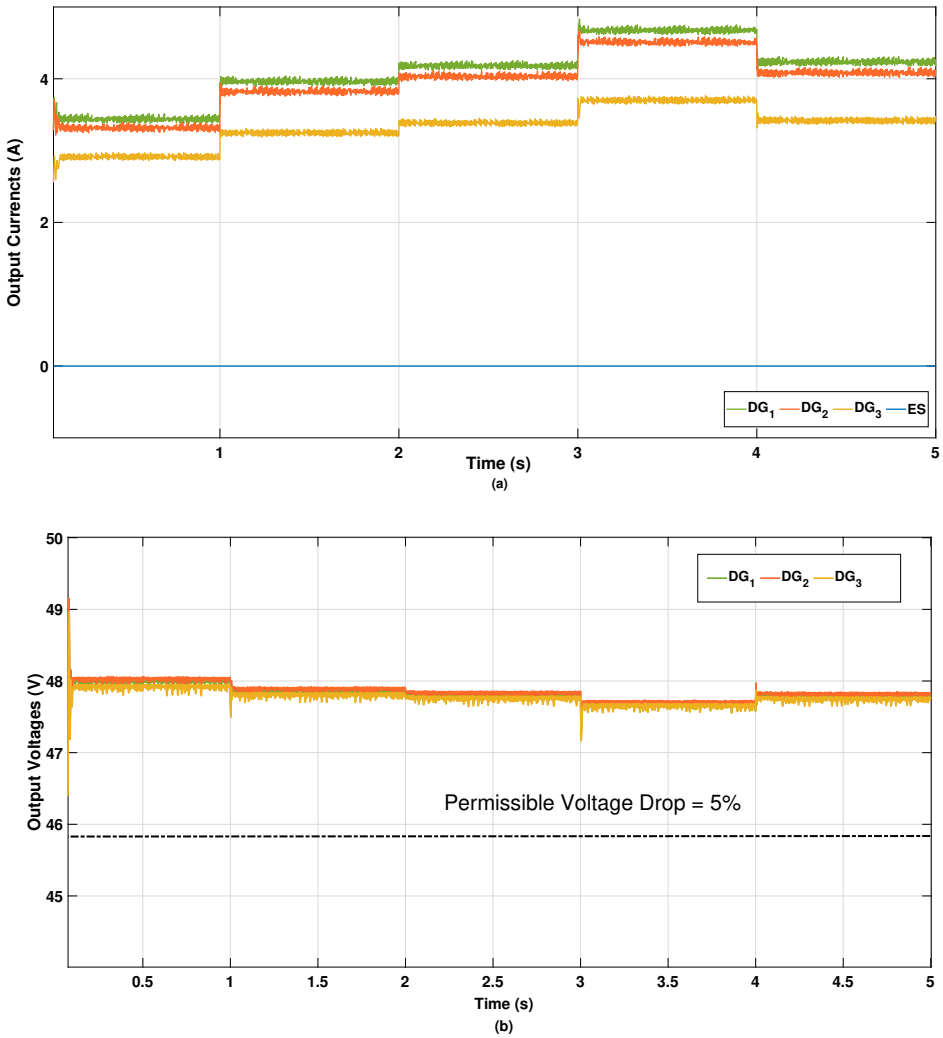

Figure 4.4: DGs response to the variable demand profile **(a)** permissible output current **(b)** permissible output voltage.

reflects poor management of stored battery energy, whereas, in both previous scenarios, voltage regulation was achieved without additional energy from the batteries.

To further investigate, the proposed control method's performance in voltage regulation at the PCC is compared with that of the conventional droop method, which applies fixed low and high droop gains regardless of load conditions. The following generic equation is used for this comparison:

$$V_{reg}(\%) = \frac{V_{nom} - V_{pcc}}{V_{nom}} \times 100 \tag{4.7}$$

where the V_{pcc} is the measured voltage at the common bus under different loading conditions. The results are shown in Fig. 4.7, as anticipated, using a constant high droop gain

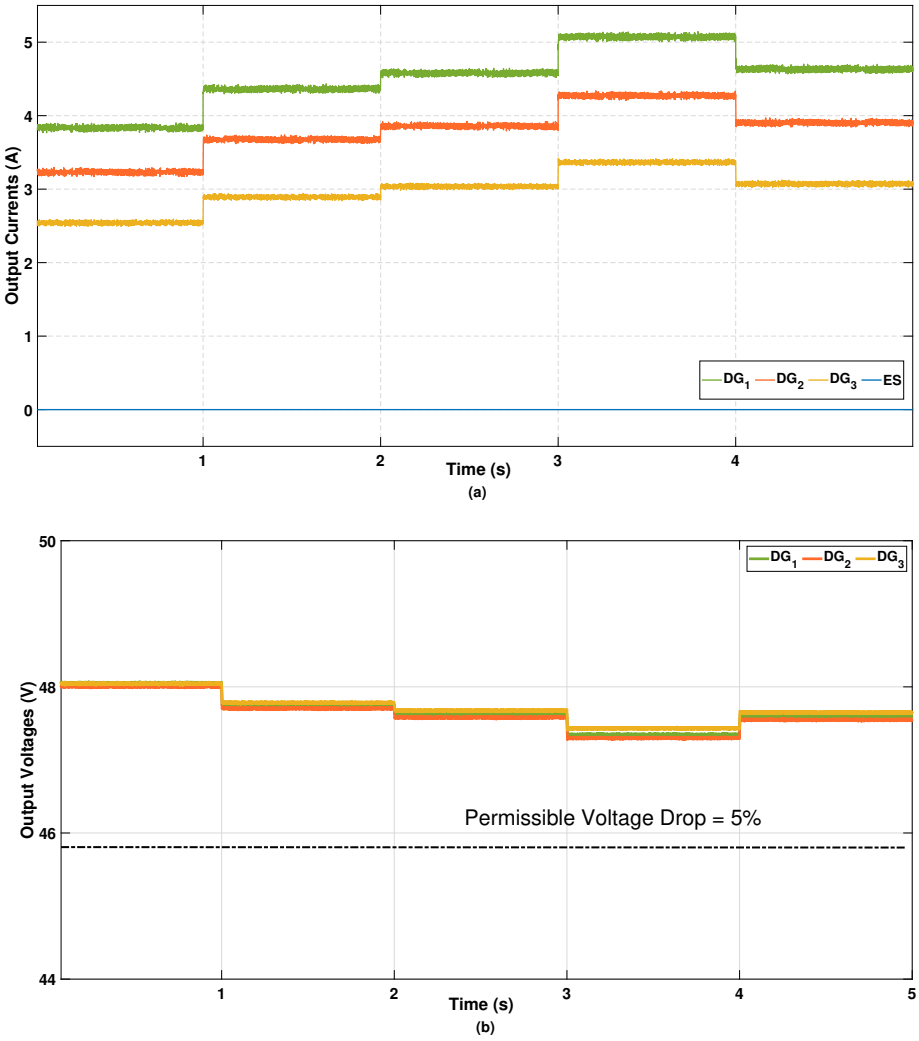

Figure 4.5: DGs response with conventional droop control**(a)** permissible output current **(b)** permissible output voltage.

disrupts voltage regulation. In contrast, the proposed method maintains voltage levels above the permissible threshold while providing a high equivalent droop gain under heavy loading conditions. To assess proper power sharing among the sources, the current-sharing error is defined as follows:

$$I_{err}(\%) = \frac{|I^n_{des} - I^n_{out}|}{I^n_{des}} \times 100 \tag{4.8}$$

where I^n_{des} is denoted as the desired output current of the $n-th$ unit, and can be defined as:

$$I^n_{des} = \frac{I^n_{nom}}{\sum_{n=1}^{N_u} I^n_{nom}} \times 100 \tag{4.9}$$

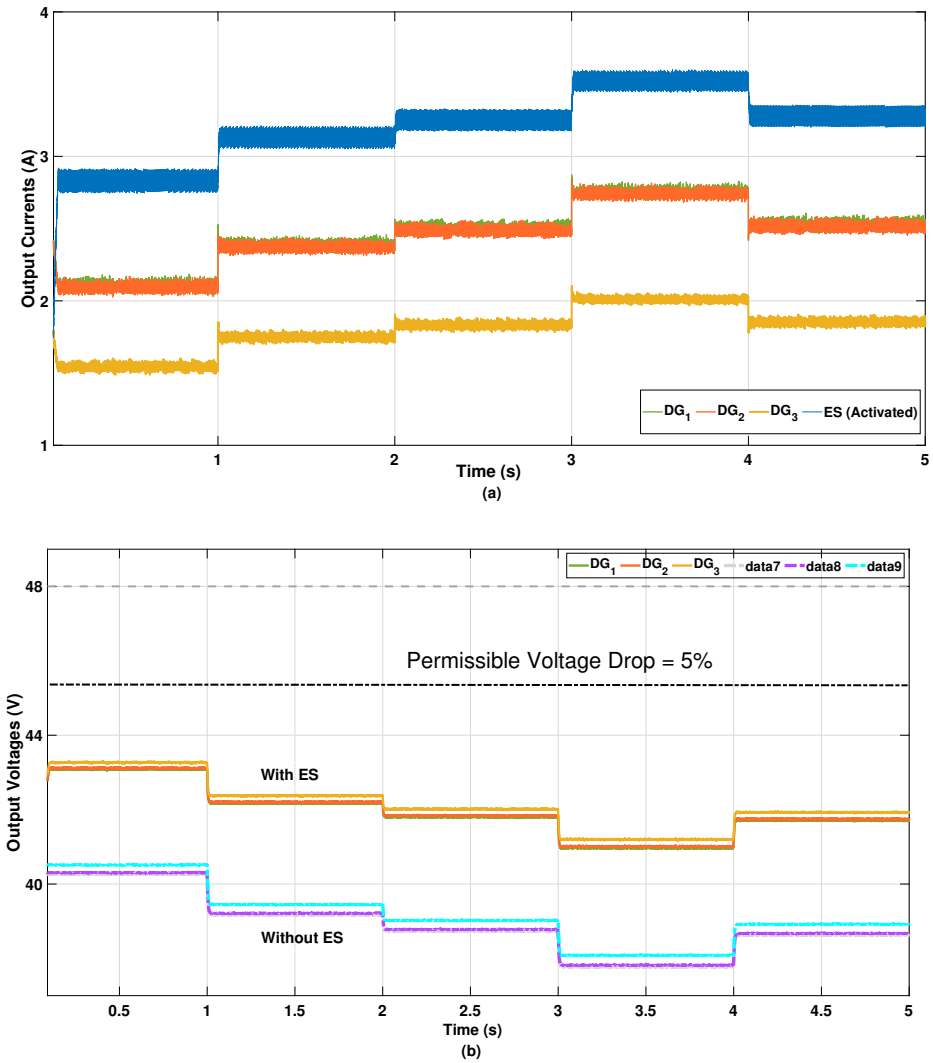

Figure 4.6: The response of the DG units with conventional droop control at high gain values **(a)** permissible output current **(b)** permissible output voltage.

and,

$$I^{n}_{Load} = \sum_{n=1}^{N_u} .I^{n}_{out} \tag{4.10}$$

In Eq. 4.10, N_u represents the total number of units. Fig. 4.8 illustrates the average current-sharing accuracy of the units across different operating modes. As shown in Fig. 4.8, small droop gains do not provide acceptable accuracy. In contrast, the proposed method achieves sufficient precision under high loading conditions, effectively meeting the need for improved power-sharing accuracy as load power increases.

Fig. 4.9 shows the impact of three different droop-based scenarios on the total power losses of the DC-MG, resulting from line resistances. As illustrated, at low load levels,

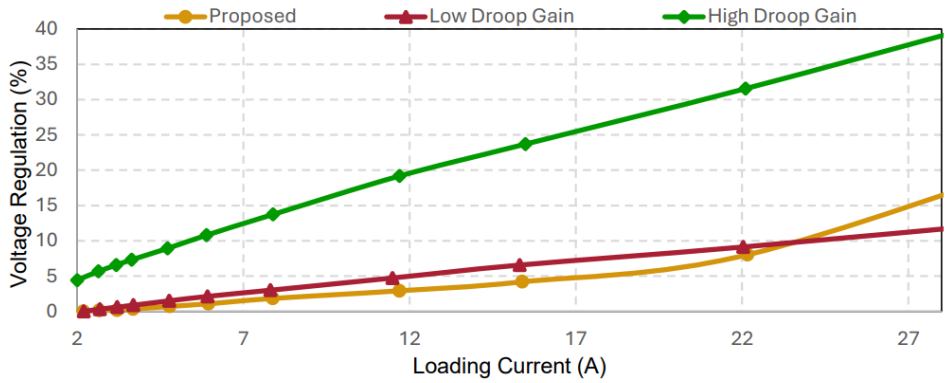

Figure 4.7: Voltage regulation comparison of proposed adaptive control approach and conventional droop control.

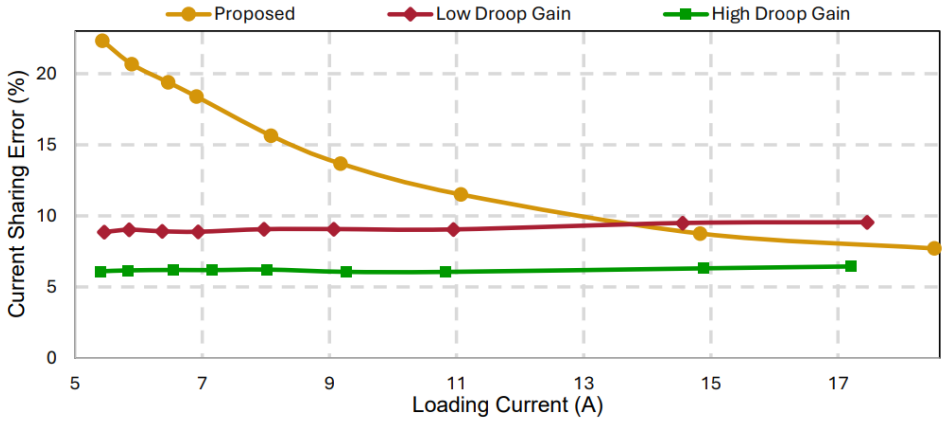

Figure 4.8: Comparison of the current-sharing error of the proposed control approach and that of the conventional droop control

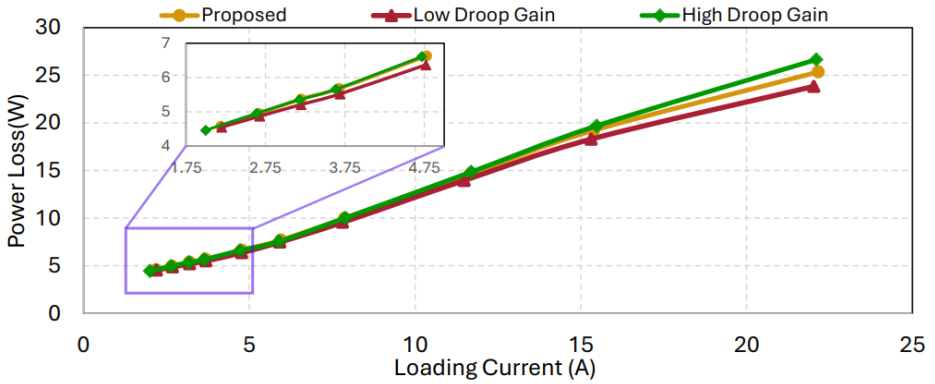

Figure 4.9: Comparison regarding total power loss in the case of the proposed methodology and the conventional droop control

the total power dissipation across the different approaches shows negligible differences. However, although smaller droop gains result in lower power dissipation at any load level,

at higher load levels—where large droop gains are required for accurate current sharing among units—the total losses with the proposed method are lower than those of a system with a fixed large droop gain. Additionally, to examine the role of the ES in enhancing the flexibility of the islanded DC-MG and maintaining voltage stability under overloading conditions, an intermittent power profile is simulated to represent overloading scenarios. In the first half of the test, a steady demand profile is assumed, matching the generation capacity of the RESs. After a certain period (i.e., t=5 s), a dynamic load is added to the DC-MG as an additional unscheduled load to simulate demand uncertainty, where demand may exceed the DGs generation capacity.

As shown in Fig. 4.10(a), during the first half of the test scenario, the ES remains inactive because the RES-based units are sufficient to meet the demand. After the dynamic load is introduced, Fig. 4.10(b) illustrates the ES's role in regulating the PCC voltage, where it functions like a suspension spring, keeping the voltage above the permissible limit. Furthermore, as demonstrated in Fig. 4.10(c), since the ES is connected in series with non-critical (NC) loads, the power dissipation in these loads is effectively managed in response to the intermittent power profile and the ES's reactive behavior.

In conclusion, the proposed adaptive droop control scheme for voltage regulation in remote islanded DC-MG is based on an effective power-sharing strategy among integrated resources, such as DGs. This approach ensures precise current sharing, mitigates the destabilizing effects of CPLs, improves voltage regulation, and reduces power losses by enabling the droop gain to vary non-linearly. Simulation results confirm its effectiveness, showing accurate load sharing among generation units with minimal voltage drop.

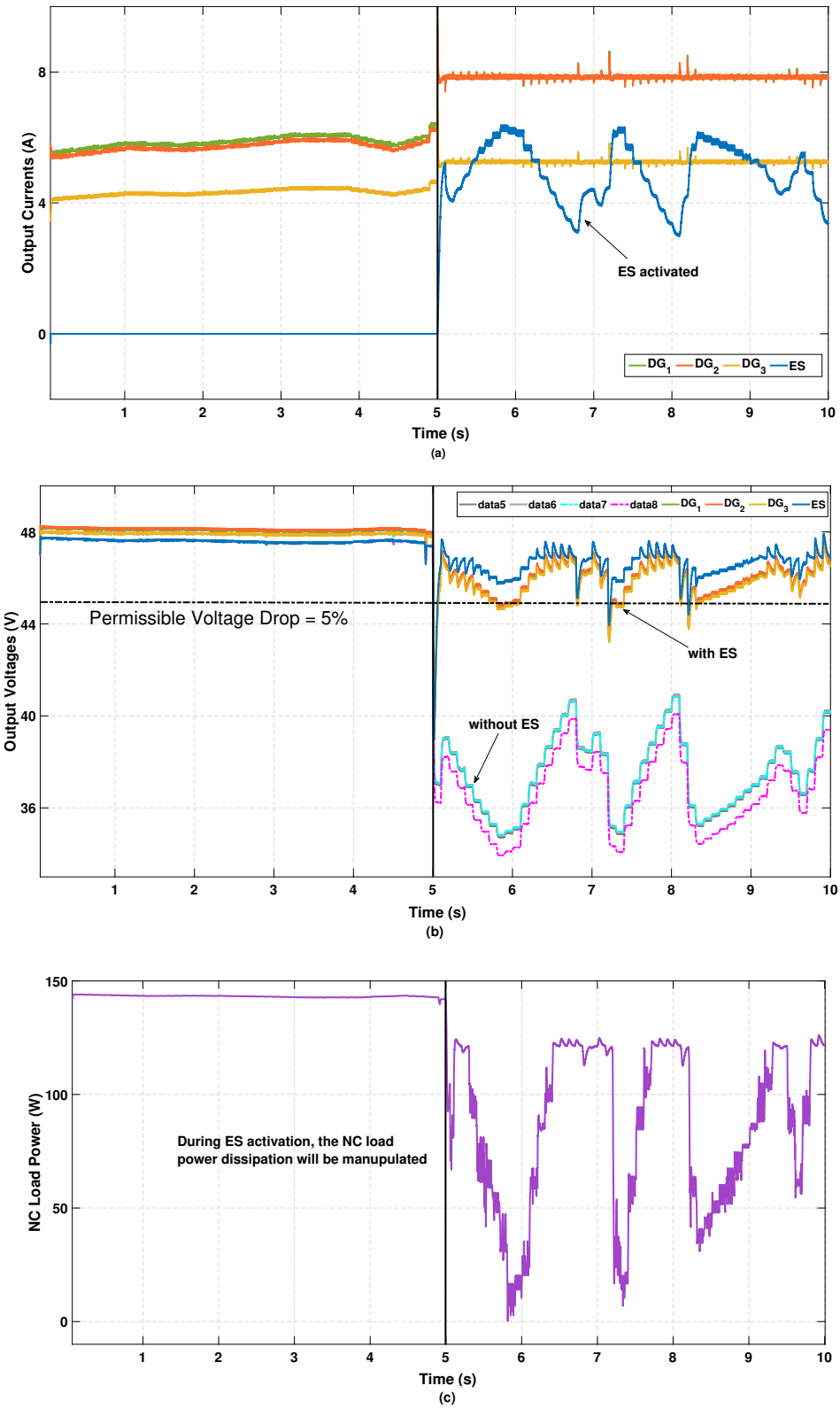

Figure 4.10: Energy storage bouncing reaction for the voltage regulation **(a)** terminal currents **(b)** terminal voltages **(c)** smart load power dissipation.

Conclusion

In this thesis, various control and optimization methodologies have been proposed to facilitate the implementation of MGs in power systems, with a particular focus on enabling the energy and ancillary services through MGs to enhance the reliability and stability of the power systems.

The proposed studies address challenges faced by small islands and grid-connected microgrids, which are characterized by high operational costs, heavy reliance on fossil fuels, and issues related to energy consumption and demand response in MMGs infrastructure. Additionally, high fuel costs and supply expenses create significant management challenges, leading to increased energy costs for the entire population. Achieving decarbonization and reducing greenhouse gas emissions in these regions is also a significant challenge. Addressing these vulnerabilities within the country's electricity system is a crucial step toward effective decarbonization.

Integrating higher levels of renewable energy into these systems is a complex challenge. It requires a thorough robust methodologies for system control, ensuring adequate resources to manage the low inertia typical of these setups and sufficient operating reserves to address the frequent and unpredictable fluctuations in renewable energy production.

This thesis proposes technical and methodological advancements in various aspects of MGs. Firstly, it examines the role of ESSs in providing energy and ancillary services, as well as the ENTSO-E and IEA standards for frequency and voltage regulation.

In all aspects and methodologies presented in this thesis, further studies and improvements can be pursued. The impact of both the presence and size of a BESS in islanded MGs can be evaluated using the approaches and methodologies outlined in Chapter 2. Subsequently, in Chapter 2, a real-time optimal control algorithm was proposed for a residential hybrid nanogrid to enhance self-consumption of energy to minimize the operational cost and maintain optimal operation for both AC and DC loads within the building, utilizing both open- and closed-loop optimal control methodologies. To analyze the impact of the

proposed robust optimization on high-voltage power systems, a robust optimal control methodology for energy management has been developed. This methodology, based on the column and constraint generation algorithm, aims to minimize operational costs while reducing battery degradation expenses, all while accounting for the uncertainties of RESs in the system under study.

In addition to these methodologies, Chapter 2 also proposes the Shapley value method and master-slave optimal methodologies for demand response management among various MGs. These approaches not only ensure load demand is met but also enable efficient energy trading to maximize revenue, which is then fairly distributed among all participants. These methodologies, developed as part of the doctoral research, involved in-depth modeling of dynamic networks to analyze trends, identify criticalities, and evaluate the impact of the proposed solutions

Chapter 3 presents a detailed study of frequency regulation and inertia control in MGs. Several control strategies and power hardware-in-the-loop tests were performed to evaluate the performance of isolated microgrids and to propose a cost-effective controller formulation for frequency regulation and synthetic inertia implementation. A novel hierarchical control framework is proposed for islanded MGs to improve frequency regulation and enhance energy management through multiple control layers. This chapter includes extensive modeling and testing to design efficient networks and methodologies, enabling real-time simulations and supporting power hardware-in-the-loop simulations.

Chapter 4 presents a thorough study of voltage regulation in DC-MGs, which is a critical ancillary service for ensuring system stability and reliability. In conclusion, this work aims to contribute to the technological advancement of these areas by supporting the seamless integration of renewable energy sources into isolated MGs through BESS and electric springs. The proposed study achieves precise current sharing, mitigates destabilizing CPLs effects, enhances voltage regulation, and reduces power losses by allowing the droop gain to vary non-linearly with loading levels.

Finally, by enhancing the stability and reliability of MGs operating in island mode, the goal is to enable their integration into interconnected grids. Future studies will focus on generalizing the methodologies proposed in this thesis for interconnected MGs and MMGs systems. These advancements could explore the possibility of nested MGs communicating to support the security of the national power system during severe contingencies. A network of dispersed MGs could contribute to re-powering parts of the system after a blackout, reducing downtime and improving service quality. In a future power system

of interconnected MGs, power system management issues could be resolved using MG resources, allowing for optimal reconfiguration or power flow solutions even when parts of the system are isolated. This would broaden network management options, reduce costs, and lower both MG implementation and electricity costs for end users.

References

[1] S. Bruno, G. Giannoccaro, M. Muzammal Islam, C. Iurlaro, M. La Scala, M. Menga, and C. Rodio, "Control and power hardware-in-the-loop tests for low-inertia power systems," in *2022 AEIT International Annual Conference (AEIT)*, 2022, pp. 1–6.

[2] S. Bruno, G. Giannoccaro, M. M. Islam, C. Iurlaro, M. L. Scala, M. Menga, and C. Rodio, "Predictive control based energy management of a residential hybrid ac-dc nanogrid," in *2022 4th International Conference on Electrical Engineering and Control Technologies (CEECT)*, 2022, pp. 1183–1187.

[3] M. M. Islam, S. Bruno, C. Iurlaro, and M. La Scala, "Robust adaptive integral backstepping control of fc-sc-battery and traction motor based hybrid electric vehicles," in *2022 AEIT International Annual Conference (AEIT)*, 2022, pp. 1–6.

[4] T. Yu, M. M. Islam, J. Wang, and M. L. Scala, "Robust optimization in energy management under ress uncertainties through bess integration," in *2023 5th International Conference on Electrical Engineering and Control Technologies (CEECT)*, 2023, pp. 85–91.

[5] M. M. Islam, T. Yu, M. L. Scala, and J. Wang, "Robust integral terminal sliding mode control for frequency regulation in islanded microgrids incorporating ress and hess using a disturbance observer," in *5th International Conference on Electrical, Communication and Computer Engineering (ICECCE)*, in press 2024, pp. 1–6.

[6] Z. Zhang, P. Lin, M. M. Islam, L. Zhou, and G. Yao, "Developing control strategies to enhance power quality in grid-connected natural gas pressure differential generation systems: Advancing clean energy practices," in *IEEE International Humanitarian Technologies Conference*, in press 2024, pp. 1–7.

[7] J. Kunqi, S. Zhang, M. M. Islam, T. Yu, Y. Wenda, and Z. Yating, "Optimization of multi-microgrid energy trading in distribution networks using a master-slave game

approach," in *IEEE International Humanitarian Technologies Conference*, in press 2024, pp. 1–5.

[8] M. M. Islam, T. Yu, M. La Scala, J. Wang, and L. Chengdong, "Optimizing cooperative alliance transactive energy framework for pv-based multi-microgrids using scheduling and cooperative game theory," in *2024 4th International Conference on Electrical Engineering and Informatics (ICon EEI)*, 2024, pp. 96–101.

[9] M. N. Rajabi, R. Cometa, C. Iurlaro, M. M. Islam, S. Bruno, and M. La Scala, "Stand-alone dc microgrids for rural areas: A decentralized energy management and voltage regulation approach," in *IEEE International Humanitarian Technologies Conference*, in press 2024, pp. 1–7.

[10] P. Lin, W. Song, Z. Zhang, L. Zhou, G. Yao, and M. M. Islam, "Sensorless control of high-speed dual three-phase permanent magnet synchronous motor," in *The Proceedings of the 19th Annual Conference of China Electrotechnical Society*. Singapore: Springer Nature Singapore, 2025, pp. 1–10.

[11] Z. He, S. Li, M. M. Islam, and G. Chen, "Study on the effect of plate rib-channel ratio on the performance of pemfc: a cleaner and sustainable energy practice," in *Springer*, in press 2024, pp. 1–8.

[12] T. Yu, M. M. Islam, L. Zhou, Z. Wang, M. La Scala, X. Guan, and G. Yao, "A novel hierarchical control framework for enhancing stability, security and reliable power dispatch tracking in islanded microgrids," *IEEE Transactions on Smart Grid*, pp. 1–10, in press 2024.

[13] M. M. Islam, T. Yu, M. La Scala, and J. Wang, "Robust nonlinear control design with optimal coordination methodology for bidirectional bev chargers in v2g/g2v applications," *Journal of Energy Storage*, pp. 1–18, in press 2024.

[14] T. Yu, M. Muzammal Islam, J. Wang, Z. Wang, M. La Scala, B. Yang, and G. Yao, "A novel augmented bolza problem and its applications in power systems to support grid services," *IEEE Transactions on Smart Grid*, pp. 1–9, , (under-review).

[15] M. Muzammal Islam, T. Yu, G. Giannoccaro, Y. Mi, M. la Scala, M. Rajabi Nasab, and J. Wang, "Improving reliability and stability of the power systems: A comprehensive review on the role of energy storage systems to enhance flexibility," *IEEE Access*, vol. 12, pp. 152 738–152 765, 2024.

[16] W. Ziqiang, Y. Haosen, X. Linyun, H. Wentao, M. Muzammal Islam, M. La Scala, and Y. Chen, "Voltage-frequency constrained control for dc-link voltage synchronization of renewable energy," *IEEE Power Engineering Letters*, vol. 12, pp. 1–3, , (under-review).

[17] I. U. Salam, M. Yousif, M. Numan, and M. Billah, "Addressing the challenge of climate change: The role of microgrids in fostering a sustainable future-a comprehensive review," *Renewable Energy Focus*, pp. 1–21, 2024.

[18] International Energy Agency (IEA), "Renewables, analysis and forecast to 2030," 2024, license: CC BY 4.0. [Online]. Available: https://www.iea.org/reports/renewables-2024

[19] Official Journal of the European Union, Brussels, Belgium, "Directive (eu) 2018/2001 of the european parliament and of the council of 11 december 2018 on the promotion of the use of energy from renewable source," 2018, license: CC BY 4.0.

[20] European Commission, Press release, Brussels, Belgium, "European green deal: Eu agrees stronger legislation to accelerate the rollout of renewable energy," 2023.

[21] Council of the European Union, "Council regulation (eu) 2024/230 of 22 december 2024 on a temporary emergency measure to streamline permit-granting procedures for renewable energy projects and facilitate power purchase agreement, official journal of the european union, brussels, belgium," 2024. [Online]. Available: https://www.astrid-online.it/static/upload/c_20/c_2024_2660_1_en_act_part1_v4.pdf

[22] E. Commission and D.-G. for Climate Action, *Going climate-neutral by 2050 – A strategic long-term vision for a prosperous, modern, competitive and climate-neutral EU economy*. Publications Office, 2019.

[23] A. M. Alonso, F. P. Marafão, and E. Tedeschi, "Dispatchable microgrids: An extended provision of systemic ancillary services to low-voltage distribution grids," *IEEE Access*, pp. 1–15, 2024.

[24] M. Uddin, H. Mo, D. Dong, S. Elsawah, J. Zhu, and J. M. Guerrero, "Microgrids: A review, outstanding issues and future trends," *Energy Strategy Reviews*, vol. 49, pp. 1–16, 2023.

[25] V. Khare and P. Chaturvedi, "Design, control, reliability, economic and energy management of microgrid: A review," *e-Prime-Advances in Electrical Engineering, Electronics and Energy*, pp. 1–20, 2023.

[26] M. Ganjian-Aboukheili, M. Shahabi, Q. Shafiee, and J. M. Guerrero, "Seamless transition of microgrids operation from grid-connected to islanded mode," *IEEE Transactions on Smart Grid*, vol. 11, no. 3, pp. 2106–2114, 2019.

[27] A. Elmouatamid, R. Ouladsine, M. Bakhouya, N. El Kamoun, M. Khaidar, and K. Zine-Dine, "Review of control and energy management approaches in micro-grid systems," *Energies*, vol. 14, no. 1, pp. 1–30, 2020.

[28] M. Kumar, S. C. Srivastava, and S. N. Singh, "Control strategies of a dc microgrid for grid connected and islanded operations," *IEEE Transactions on Smart Grid*, vol. 6, no. 4, pp. 1588–1601, 2015.

[29] J. F. Castro, R. A. Roncolatto, A. R. Donadon, V. E. Andrade, P. Rosas, R. G. Bento, J. G. Matos, F. A. Assis, F. C. Coelho, R. Quadros *et al.*, "Microgrid applications and technical challenges—the brazilian status of connection standards and operational procedures," *Energies*, vol. 16, no. 6, pp. 1–25, 2023.

[30] Y. Wang, P. Liu, D. Liu, F. Deng, and Z. Chen, "Enhanced hierarchical control framework of microgrids with efficiency improvement and thermal management," *IEEE Transactions on Energy Conversion*, vol. 36, no. 1, pp. 11–22, 2020.

[31] S. Xia, S. Bu, C. Wan, X. Lu, K. W. Chan, and B. Zhou, "A fully distributed hierarchical control framework for coordinated operation of ders in active distribution power networks," *IEEE transactions on power systems*, vol. 34, no. 6, pp. 5184–5197, 2018.

[32] S. E. Eyimaya and N. Altin, "Microgrids: Definitions, architecture, and control strategies," in *Power Electronics Converters and their Control for Renewable Energy Applications*. Elsevier, 2023, pp. 167–186.

[33] E. Kabalci, "Hierarchical control in microgrid," *Microgrid architectures, control and protection methods*, pp. 381–401, 2020.

[34] S. H. H. Dolatabadi, A. Soleimani, A. Ebtia, M. Shafie-khah, and T. H. Bhuiyan, "Enhancing voltage profile in islanded microgrids through hierarchical control strategies," *Electric Power Systems Research*, vol. 231, pp. 1–11, 2024.

[35] International Electrotechnical Commission, "IEC TS 62898-1:2017/AMD1:2023 Microgrids—Part1:Guidelines for Microgrid Projects Planning and Specification," IEC Publications, Geneva, Switzerland, Technical Specification, 2023.

[36] IEEE, "IEEE Standard for the Specification of Microgrid Controllers," *IEEE Std 2030.7-2017*, pp. 1–43, 2018.

[37] "Ieee standard for the testing of microgrid controllers," *IEEE Std 2030.8-2018*, pp. 1–42, 2018.

[38] "Ieee standard for interconnection and interoperability of distributed energy resources with associated electric power systems interfaces," *IEEE Std 1547-2018 (Revision of IEEE Std 1547-2003)*, pp. 1–138, 2018.

[39] International Electrotechnical Commission, "IEC TS 62898-2:2018 Microgrids—Part2:Guidelines for operations," IEC Publications, Geneva, Switzerland, Technical Specification, 2018.

[40] ——, "IEC TS 62898-3:2018 Microgrids—Part3: Technical Specifications: Microgrid monitoring and control systems," IEC Publications, Geneva, Switzerland, Technical Specification, 2018.

[41] M. Abdelsattar, M. A. Ismeil, M. M. Aly, and S. Saber Abu-Elwfa, "Analysis of renewable energy sources and electrical vehicles integration into microgrid," *IEEE Access*, vol. 12, pp. 66 822–66 832, 2024.

[42] K. Rahbar, C. C. Chai, and R. Zhang, "Energy cooperation optimization in microgrids with renewable energy integration," *IEEE Transactions on Smart Grid*, vol. 9, no. 2, pp. 1482–1493, 2018.

[43] M. Khalid, "Smart grids and renewable energy systems: Perspectives and grid integration challenges," *Energy Strategy Reviews*, vol. 51, pp. 1–26, 2024.

[44] L. Polleux, G. Guerassimoff, J.-P. Marmorat, J. Sandoval-Moreno, and T. Schuhler, "An overview of the challenges of solar power integration in isolated industrial

microgrids with reliability constraints," *Renewable and Sustainable Energy Reviews*, vol. 155, pp. 1–19, 2022.

[45] M. Hasan, Z. Mifta, N. A. Salsabil, S. J. Papiya, M. Hossain, P. Roy, O. Farrok *et al.*, "A critical review on control mechanisms, supporting measures, and monitoring systems of microgrids considering large scale integration of renewable energy sources," *Energy Reports*, vol. 10, pp. 4582–4603, 2023.

[46] F. Tooryan, H. HassanzadehFard, E. R. Collins, S. Jin, and B. Ramezani, "Smart integration of renewable energy resources, electrical, and thermal energy storage in microgrid applications," *Energy*, vol. 212, pp. 1–17, 2020.

[47] E. N. of Transmission System Operators for Electricity (ENTSO-E), "Scenario outlook adequacy forecast 2015," 2015.

[48] A. Mallick, A. Mishra, A. R. Hota, and P. Bajpai, "Distributed coordination of multi-microgrids in active distribution networks for provisioning ancillary services," *IEEE Systems Journal*, pp. 1492–1503, 2024.

[49] J. Engels, B. Claessens, and G. Deconinck, "Optimal combination of frequency control and peak shaving with battery storage systems," *IEEE Transactions on Smart Grid*, vol. 11, no. 4, pp. 3270–3279, 2019.

[50] Z. Xu, "The electricity market design for decentralized flexibility sources," 2019.

[51] P. Mancarella, G. Chicco, and T. Capuder, "Arbitrage opportunities for distributed multi-energy systems in providing power system ancillary services," *Energy*, vol. 161, pp. 381–395, 2018.

[52] D. Kanakadhurga and N. Prabaharan, "Demand side management in microgrid: A critical review of key issues and recent trends," *Renewable and Sustainable Energy Reviews*, vol. 156, p. 111915, 2022.

[53] S. Nikkhah, I. Sarantakos, N.-M. Zografou-Barredo, A. Rabiee, A. Allahham, and D. Giaouris, "A joint risk-and security-constrained control framework for real-time energy scheduling of islanded microgrids," *IEEE Transactions on Smart Grid*, vol. 13, no. 5, pp. 3354–3368, 2022.

[54] M. Farrokhabadi, C. A. Cañizares, and K. Bhattacharya, "Frequency control in isolated/islanded microgrids through voltage regulation," *IEEE Transactions on Smart Grid*, vol. 8, no. 3, pp. 1185–1194, 2015.

[55] Y. Shan, L. Ma, and X. Yu, "Hierarchical control and economic optimization of microgrids considering the randomness of power generation and load demand," *Energies*, vol. 16, no. 14, p. 5503, 2023.

[56] E. N. of Transmission System Operators for Electricity (ENTSO-E), "No 727481 reserve, drafting of ancillary services and network codes definitions v2," 2019.

[57] T. European Network of Transmission System Operators for Electricity (ENTSO-E), "Industrial demand response for frequency balancing and voltage control," 2021.

[58] S. Oshnoei, M. R. Aghamohammadi, S. Oshnoei, S. Sahoo, A. Fathollahi, and M. H. Khooban, "A novel virtual inertia control strategy for frequency regulation of islanded microgrid using two-layer multiple model predictive control," *Applied Energy*, vol. 343, pp. 1–13, 2023.

[59] V. Di Dio, G. Sciumè, G. Zizzo, R. Musca, and A. Vasile, "Analysis of a fast reserve unit behaviour with additional modular synthetic inertia control," in *2021 IEEE 15th International Conference on Compatibility, Power Electronics and Power Engineering (CPE-POWERENG)*. IEEE, 2021, pp. 1–6.

[60] V. Calderaro, V. Galdi, F. Lamberti, and A. Piccolo, "A smart strategy for voltage control ancillary service in distribution networks," *IEEE Transactions on Power Systems*, vol. 30, no. 1, pp. 494–502, 2014.

[61] E. N. of Transmission System Operators for Electricity (ENTSO-E), "Reactive power management at t – d interface," 2016.

[62] D. Jay and K. Swarup, "A comprehensive survey on reactive power ancillary service markets," *Renewable and Sustainable Energy Reviews*, vol. 144, pp. 1–15, 2021.

[63] W. Zhou, Y. Wang, F. Peng, Y. Liu, H. Sun, and Y. Cong, "Distribution network congestion management considering time sequence of peer-to-peer energy trading," *International Journal of Electrical Power & Energy Systems*, vol. 136, pp. 1–15, 2022.

[64] D. Villacci, F. Gasparotto, L. Orrú, P. Pelacchi, D. Poli, A. Vaccaro, G. Lisciandrello, and G. Coletta, "Congestion management in italian hv grid using novel dynamic thermal rating methods: first results of the h2020 european project osmose," in *2020 AEIT International Annual Conference (AEIT)*. IEEE, 2020, pp. 1–6.

[65] W. Sun, C.-C. Liu, and S. Liu, "Black start capability assessment in power system restoration," in *2011 IEEE Power and Energy Society General Meeting*. IEEE, 2011, pp. 1–7.

[66] K. M. Kurundkar and G. A. Vaidya, "Stochastic security-constrained economic dispatch of load-following and contingency reserves ancillary service using a grid-connected microgrid during uncertainty," *Energies*, vol. 16, no. 6, pp. 1–25, 2023.

[67] E. Union, "Basic schemes for tso-dso coordination and ancillary services provision," 2016.

[68] A. Emrani and A. Berrada, "A comprehensive review on techno-economic assessment of hybrid energy storage systems integrated with renewable energy," *Journal of Energy Storage*, vol. 84, pp. 1–36, 2024.

[69] T. F. Agajie, A. Ali, A. Fopah-Lele, I. Amoussou, B. Khan, C. L. R. Velasco, and E. Tanyi, "A comprehensive review on techno-economic analysis and optimal sizing of hybrid renewable energy sources with energy storage systems," *Energies*, vol. 16, no. 2, pp. 1–26, 2023.

[70] N. McIlwaine, A. M. Foley, D. J. Morrow, D. Al Kez, C. Zhang, X. Lu, and R. J. Best, "A state-of-the-art techno-economic review of distributed and embedded energy storage for energy systems," *Energy*, vol. 229, pp. 1–19, 2021.

[71] Y. He, S. Guo, J. Zhou, J. Ye, J. Huang, K. Zheng, and X. Du, "Multi-objective planning-operation co-optimization of renewable energy system with hybrid energy storages," *Renewable Energy*, vol. 184, pp. 776–790, 2022.

[72] Y. He, S. Guo, J. Zhou, F. Wu, J. Huang, and H. Pei, "The quantitative techno-economic comparisons and multi-objective capacity optimization of wind-photovoltaic hybrid power system considering different energy storage technologies," *Energy conversion and management*, vol. 229, pp. 1–18, 2021.

[73] U. T. Salman, S. Shafiq, F. S. Al-Ismail, and M. Khalid, "A review of improvements in power system flexibility: Implementation, operation and economics," *Electronics*, vol. 11, no. 4, pp. 1–25, 2022.

[74] M. M. Rahman, A. O. Oni, E. Gemechu, and A. Kumar, "Assessment of energy storage technologies: A review," *Energy Conversion and Management*, vol. 223, pp. 1–28, 2020.

[75] M. M. Rana, M. Uddin, M. R. Sarkar, S. T. Meraj, G. Shafiullah, S. Muyeen, M. A. Islam, and T. Jamal, "Applications of energy storage systems in power grids with and without renewable energy integration—a comprehensive review," *Journal of energy storage*, vol. 68, pp. 1–20, 2023.

[76] M. Reveles-Miranda, V. Ramirez-Rivera, and D. Pacheco-Catalán, "Hybrid energy storage: Features, applications, and ancillary benefits," *Renewable and Sustainable Energy Reviews*, vol. 192, pp. 1–15, 2024.

[77] S. Hajiaghasi, A. Salemnia, and M. Hamzeh, "Hybrid energy storage system for microgrids applications: A review," *Journal of Energy Storage*, vol. 21, pp. 543–570, 2019.

[78] D. Rekioua, "Energy storage systems for photovoltaic and wind systems: A review," *Energies*, vol. 16, no. 9, pp. 1–26, 2023.

[79] M. Numan, M. F. Baig, M. Yousif *et al.*, "Reliability evaluation of energy storage systems combined with other grid flexibility options: A review," *Journal of Energy Storage*, vol. 63, pp. 1–23, 2023.

[80] M. Kiehbadroudinezhad, A. Merabet, and H. Hosseinzadeh-Bandbafha, "Review of latest advances and prospects of energy storage systems: considering economic, reliability, sizing, and environmental impacts approach," *Clean Technologies*, vol. 4, no. 2, pp. 477–501, 2022.

[81] E. Rahmani, S. Mohammadi, M. Zadehbagheri, and M. Kiani, "Probabilistic reliability management of energy storage systems in connected/islanding microgrids with renewable energy," *Electric Power Systems Research*, vol. 214, pp. 1–11, 2023.

[82] J. Liu, H. Wu, H. Huang, and H. Yang, "Renewable energy design and optimization for a net-zero energy building integrating electric vehicles and battery storage

considering grid flexibility," *Energy Conversion and Management*, vol. 298, pp. 1–21, 2023.

[83] J. Zhang, J. Liu, L. Chen, L. Zhang, P. Zeng, and Y. Li, "Reliability evaluation of high permeability renewable energy distribution network considering energy storage charge and discharge strategy," *Energy Reports*, vol. 9, pp. 361–368, 2023.

[84] S. Sahoo and P. Timmann, "Energy storage technologies for modern power systems: A detailed analysis of functionalities, potentials, and impacts," *IEEE Access*, vol. 11, pp. 49 689–49 729, 2023.

[85] A. Z. A. Shaqsi, K. Sopian, and A. Al-Hinai, "Review of energy storage services, applications, limitations, and benefits," *Energy reports*, vol. 6, pp. 288–306, 2020.

[86] G. Raman, G. Raman, J. C.-H. Peng, and W. Xiao, "Bridging the transition to dc distribution: A hybrid microgrid for residential apartments," in *2017 IEEE Innovative Smart Grid Technologies-Asia (ISGT-Asia)*. IEEE, 2017, pp. 1–6.

[87] Z. Yan, X. Zhu, Y. Chang, X. Wang, Z. Ye, Z. Xu, and A. Fars, "Renewable energy effects on energy management based on demand response in microgrids environment," *Renewable Energy*, vol. 213, pp. 205–217, 2023.

[88] G. Raman, G. Raman, J. C.-H. Peng, and W. Xiao, "Bridging the transition to dc distribution: A hybrid microgrid for residential apartments," in *2017 IEEE Innovative Smart Grid Technologies-Asia (ISGT-Asia)*. IEEE, 2017, pp. 1–6.

[89] S. Bruno, M. Dicorato, M. La Scala, R. Sbrizzai, P. A. Lombardi, and B. Arendarski, "Optimal sizing and operation of electric and thermal storage in a net zero multi energy system," *Energies*, vol. 12, no. 17, pp. 1–16, 2019.

[90] S. Bruno, G. Giannoccaro, M. M. Islam, C. Iurlaro, M. L. Scala, M. Menga, and C. Rodio, "Predictive control based energy management of a residential hybrid ac-dc nanogrid," in *2022 4th International Conference on Electrical Engineering and Control Technologies (CEECT)*, 2022, pp. 1183–1187.

[91] M. S. Alam and S. A. Arefifar, "Energy management in power distribution systems: Review, classification, limitations and challenges," *IEEE Access*, vol. 7, pp. 92 979–93 001, 2019.

[92] D. Wang, L. Liu, H. Jia, W. Wang, Y. Zhi, Z. Meng, and B. Zhou, "Review of key problems related to integrated energy distribution systems," *CSEE Journal of Power and Energy Systems*, vol. 4, no. 2, pp. 130–145, 2018.

[93] M. H. Saeed, W. Fangzong, B. A. Kalwar, and S. Iqbal, "A review on microgrids' challenges & perspectives," *IEEE Access*, vol. 9, pp. 166 502–166 517, 2021.

[94] S. Sharma, P. Jain, A. Sant, and A. Kumar, "Fair pricing in transactive energy management for peer-to-peer trading: A shapley value analysis using game theory," in *2023 7th International Conference on Computer Applications in Electrical Engineering-Recent Advances (CERA)*. IEEE, 2023, pp. 1–6.

[95] A. J. Onumanyi, S. J. Isaac, C. P. Kruger, and A. M. Abu-Mahfouz, "Transactive energy: State-of-the-art in control strategies, architectures, and simulators," *IEEE Access*, vol. 9, pp. 131 552–131 573, 2021.

[96] M. Moafi, R. R. Ardeshiri, M. W. Mudiyanselage, M. Marzband, A. Abusorrah, M. Rawa, and J. M. Guerrero, "Optimal coalition formation and maximum profit allocation for distributed energy resources in smart grids based on cooperative game theory," *International Journal of Electrical Power & Energy Systems*, vol. 144, pp. 1–14, 2023.

[97] L. Wang, Z. Wang, Z. Li, M. Yang, and X. Cheng, "Distributed optimization for network-constrained peer-to-peer energy trading among multiple microgrids under uncertainty," *International Journal of Electrical Power & Energy Systems*, vol. 149, p. 109065, 2023.

[98] H. Hou, Z. Wang, B. Zhao, L. Zhang, Y. Shi, and C. Xie, "Peer-to-peer energy trading among multiple microgrids considering risks over uncertainty and distribution network reconfiguration: A fully distributed optimization method," *International Journal of Electrical Power & Energy Systems*, vol. 153, p. 109316, 2023.

[99] N. Nasiri, S. Zeynali, S. N. Ravadanegh, and S. Kubler, "Moment-based distributionally robust peer-to-peer transactive energy trading framework between networked microgrids, smart parking lots and electricity distribution network," *IEEE Transactions on Smart Grid*, vol. 15, no. 2, pp. 1965–1977, 2023.

[100] Z. Chen, R. Jia, S. Wang, H. Nan, L. Zhao, X. Zhang, S. Hu, and Q. Xu, "Two-layer optimal scheduling of distribution network-multi-microgrids based on master–slave game," *Frontiers in Energy Research*, vol. 12, pp. 1–14, 2024.

[101] B. Zhu and D. Wang, "Master–slave game optimal scheduling for multi-agent integrated energy system based on uncertainty and demand response," *Sustainability*, vol. 16, no. 8, pp. 1–27, 2024.

[102] Y. Chen, S. He, W. Wang, Z. Yuan, J. Cheng, Z. Cheng, and X. Fan, "Optimization strategy for shared energy storage operators-multiple microgrids with hybrid game-theoretic energy trading," *Processes*, vol. 12, no. 1, pp. 1–26, 2024.

[103] F. Marzbani and A. Abdelfatah, "Economic dispatch optimization strategies and problem formulation: A comprehensive review," *Energies*, vol. 17, no. 3, pp. 1–31, 2024.

[104] K. E. Fahim, L. C. D. Silva, F. Hussain, and H. Yassin, "A state-of-the-art review on optimization methods and techniques for economic load dispatch with photovoltaic systems: Progress, challenges, and recommendations," *Sustainability*, vol. 15, no. 15, pp. 1–29, 2023.

[105] Q. Zhou, J. Zhang, P. Gao, R. Zhang, L. Liu, S. Wang, L. Cheng, W. Wang, and S. Yang, "Two-stage robust optimization for prosumers considering uncertainties from sustainable energy of wind power generation and load demand based on nested c&cg algorithm," *Sustainability*, vol. 15, no. 12, pp. 1–23, 2023.

[106] M. Mansouri, M. Eskandari, Y. Asadi, P. Siano, and H. H. Alhelou, "Pre-perturbation operational strategy scheduling in microgrids by two-stage adjustable robust optimization," *IEEE Access*, vol. 10, pp. 74 655–74 670, 2022.

[107] A. A. Shah, X. Han, H. Armghan, and A. A. Almani, "A nonlinear integral backstepping controller to regulate the voltage and frequency of an islanded microgrid inverter," *Electronics*, vol. 10, no. 6, p. 660, 2021.

[108] H. Bevrani, F. Habibi, P. Babahajyani, M. Watanabe, and Y. Mitani, "Intelligent frequency control in an ac microgrid: Online pso-based fuzzy tuning approach," *IEEE transactions on smart grid*, vol. 3, no. 4, pp. 1935–1944, 2012.

[109] A. Mohammadzadeh and E. Kayacan, "A novel fractional-order type-2 fuzzy control method for online frequency regulation in ac microgrid," *Engineering Applications of Artificial Intelligence*, vol. 90, p. 103483, 2020.

[110] D. Qiu, L. Peng, X. Lai *et al.*, "kw-grade unitized regenerative fuel cell stack design for high round-trip efficiencies," *Energy Conversion and Management*, vol. 270, pp. 1–11, 2022.

[111] E. Rute-Luengo, A. Navas-Fonseca, J. S. Gómez, E. Espina, C. Burgos-Mellado, D. Saez, M. Sumner, and D. Munoz-Carpintero, "Distributed model-based predictive secondary control for hybrid ac/dc microgrids," *IEEE Journal of Emerging and Selected Topics in Power Electronics*, vol. 11, no. 1, pp. 627–642, 2022.

[112] A. Leon and J. A. Solsona, "Design of reduced-order nonlinear observers for energy conversion applications," *IET Control Theory & Applications*, vol. 4, no. 5, pp. 724–734, 2010.

[113] C. Burgos-Mellado, A. Costabeber, M. Sumner, R. Cárdenas-Dobson, and D. Sáez, "Small-signal modelling and stability assessment of phase-locked loops in weak grids," *Energies*, vol. 12, no. 7, pp. 1–30, 2019.

[114] F. Garcia-Torres and C. Bordons, "Optimal economical schedule of hydrogen-based microgrids with hybrid storage using model predictive control," *IEEE Transactions on Industrial Electronics*, vol. 62, no. 8, pp. 5195–5207, 2015.

[115] A. Weiß, A. Siebel, M. Bernt, T.-H. Shen, V. Tileli, and H. Gasteiger, "Impact of intermittent operation on lifetime and performance of a pem water electrolyzer," *Journal of the electrochemical society*, vol. 166, no. 8, pp. F487–F497, 2019.

[116] J. Wang, F. Xu, H. Jin, Y. Chen, and Y. Wang, "Non-noble metal-based carbon composites in hydrogen evolution reaction: fundamentals to applications," *Advanced materials*, vol. 29, no. 14, pp. 1–35, 2017.

[117] K. T. Martin, A. C. Marchesan, O. C. B. de Araújo, G. Cardoso, and M. F. da Silva, "Mixed integer linear programming applied to adaptive directional overcurrent protection considering n-1 contingency," *IEEE Transactions on Industry Applications*, vol. 59, no. 3, pp. 2807–2821, 2023.

[118] H. Dagdougui, A. Ouammi, and R. Sacile, "Optimal control of a network of power microgrids using the pontryagin's minimum principle," *IEEE Transactions on Control Systems Technology*, vol. 22, no. 5, pp. 1942–1948, 2014.

[119] T. Liu, A. Chen, F. Gao, X. Liu, X. Li, and S. Hu, "Double-loop control strategy with cascaded model predictive control to improve frequency regulation for islanded microgrids," *IEEE Transactions on Smart Grid*, vol. 13, no. 5, pp. 3954–3967, 2022.

[120] M. Mao and A. Astolfi, "Optimal dynamic economic dispatch for microgrid using pontryagin's minimum principle," in *2023 IEEE Power Energy Society General Meeting (PESGM)*. IEEE, 2023, pp. 1–5.

[121] Z. Tu, B. Fan, J. Khazaei, W. Zhang, and W. Liu, "Optimal reset-control-based load frequency regulation in isolated microgrids," *IEEE Transactions on Sustainable Energy*, vol. 13, no. 4, pp. 2239–2249, 2022.

[122] F.-J. Lin, K.-H. Tan, X.-Y. Weng, and Y.-R. Li, "An improved droop-controlled microgrid using intelligent variable droop coefficient estimation," *IEEE Journal of Emerging and Selected Topics in Power Electronics*, vol. 12, no. 4, pp. 4117–4132, 2024.

[123] P. Bettiol and C. Mariconda, "Regularity and necessary conditions for a bolza optimal control problem," *Journal of Mathematical Analysis and Applications*, vol. 489, no. 1, pp. 1–17, 2020.

[124] E. Rute-Luengo, A. Navas-Fonseca, J. S. Gómez, E. Espina, C. Burgos-Mellado, D. Saez, M. Sumner, and D. Munoz-Carpintero, "Distributed model-based predictive secondary control for hybrid ac/dc microgrids," *IEEE Journal of Emerging and Selected Topics in Power Electronics*, vol. 11, no. 1, pp. 627–642, 2022.

[125] S. Bruno, G. Giannoccaro, C. Iurlaro, M. La Scala, and C. Rodio, "A low-cost controller to enable synthetic inertia response of distributed energy resources," in *2020 IEEE International Conference on Environment and Electrical Engineering and 2020 IEEE Industrial and Commercial Power Systems Europe (EEEIC/I&CPS Europe)*. IEEE, 2020, pp. 1–6.

[126] S. Bruno, G. Giannoccaro, M. Muzammal Islam, C. Iurlaro, M. La Scala, M. Menga, and C. Rodio, "Control and power hardware-in-the-loop tests for low-inertia power

systems," in *2022 AEIT International Annual Conference (AEIT)*. IEEE, 2022, pp. 1–6.

[127] M. M. Kamal, I. Ashraf, and E. Fernandez, "Optimal sizing of standalone rural microgrid for sustainable electrification with renewable energy resources," *Sustainable Cities and Society*, vol. 88, pp. 1–21, 2023.

[128] M. Muzammal Islam, T. Yu, G. Giannoccaro, Y. Mi, M. la Scala, M. Rajabi Nasab, and J. Wang, "Improving reliability and stability of the power systems: A comprehensive review on the role of energy storage systems to enhance flexibility," *IEEE Access*, vol. 12, pp. 152 738–152 765, 2024.

[129] J. S. Gomez, D. Saez, J. W. Simpson-Porco, and R. Cárdenas, "Distributed predictive control for frequency and voltage regulation in microgrids," *IEEE Transactions on Smart Grid*, vol. 11, no. 2, pp. 1319–1329, 2019.

[130] L. Herrera, W. Zhang, and J. Wang, "Stability analysis and controller design of dc microgrids with constant power loads," *IEEE Transactions on smart grid*, vol. 8, no. 2, pp. 881–888, 2015.

[131] T. Dragičević, X. Lu, J. C. Vasquez, and J. M. Guerrero, "Dc microgrids—part i: A review of control strategies and stabilization techniques," *IEEE Transactions on power electronics*, vol. 31, no. 7, pp. 4876–4891, 2015.

[132] A. Khorsandi, M. Ashourloo, and H. Mokhtari, "A decentralized control method for a low-voltage dc microgrid," *IEEE Transactions on Energy Conversion*, vol. 29, no. 4, pp. 793–801, 2014.

[133] I. Alhamrouni, M. Hairullah, N. Omar, M. Salem, A. Jusoh, and T. Sutikno, "Modelling and design of pid controller for voltage control of ac hybrid micro-grid," *International Journal of Power Electronics and Drive Systems*, vol. 10, no. 1, p. 151, 2019.

Acronyms

AC alternating current. 14, 37, 39–41, 44–46, 76, 144

ADC Analog to digital converter. 128

ARERA Autorita di Regolazione per Energia Reti e Ambiente. 24

AS Ancillary services. 26, 27

AVR automatic voltage regulation. 25

BESS battery energy storage systems. 16, 39, 40, 42, 44–52, 55, 56, 67, 68, 71, 76, 77, 79, 80, 82, 83, 94, 98, 107, 129, 130, 144, 145

BMS battery management system. 129

CPLs constant power loads. 133, 134, 142, 145

CSC current source converter. v, 93, 99, 106, 109, 110

DC Direct Current. 8, 9, 14, 37, 39–41, 44–46, 76, 131–133, 135, 136, 140, 142, 144, 145

DERs distributed energy resources. iii, iv, 12–18, 21, 22, 26, 27, 29, 34, 35, 80, 93, 94, 104, 105, 108, 110, 128, 129, 131

DG distributed generations. vi, 10, 82, 132, 135–140, 142

DO disturbance observer. 81, 85, 86, 88, 90–92

DOD depth of discharge. 71, 103

DR Demand response. 21

DSO Distribution system operator. 26, 27, 57–63, 65–67

DTR Dynamic thermal rating. 25

ED economic dispatch. 67

EMS Energy management system. ii, v, 16, 18, 69, 76, 77, 79, 92–95, 98, 99, 105–110

ENTSO-E European Network of Transmission System Operators for Electricity. 20, 21, 144

ES Energy storage. 132, 135–137, 142

ESSs energy storage systems. 9, 12, 14, 19, 20, 28–30, 33–35, 52, 59, 144

EU European Union. 10, 11, 26

EV electric vehicles. 13, 20

FC fuel cell. 82, 83, 101, 102, 117

FCR Frequency Containment Reserve. 24

FESS flywheel energy storage system. 82, 83

FFR fast frequency regulation. 24

GHGs greenhouse gases. 10, 11, 18, 19

GPIO General Purpose Input/Output. 128, 129

HESS hybrid energy storage systems. ii, 30, 81, 82, 92, 99, 126

IEA International Energy Agency. 10, 144

ISMC Integral sliding mode control. 90, 91

ITSMC Integral terminal sliding mode control. 81, 82, 85, 86, 88, 90, 91

LB lower bound. 68, 69

LV low voltage. 12

MERGE Microgrids for Efficient, Reliable, and Green Energy. 14

MG Microgrid. v, 6–10, 12–22, 24, 28–30, 34, 35, 37, 48–63, 65, 66, 76, 81, 82, 84–86, 90–92, 111, 112, 117, 126, 131–133, 135, 136, 140, 142, 144–146

MILP mixed integer linear programming. 53, 92

MLD mixed logical dynamic. 101

MMGs Multi-microgrids. ii, iv, 8, 9, 35, 47–49, 52, 53, 56–58, 60, 65, 67, 144, 145

MPC model predictive control. iii, v, 37, 44–47, 92, 95–97, 108–110, 112

MV medium voltage. 12

OPF optimal power flow. 73, 77

PCC point of common coupling. 42, 132, 135, 138, 142

PHIL Power hardware-in-the loop. 89

PI proportional integrator. 91, 135

PLL phase locked loop. 95

POT pressure of tank. 102, 107, 108

PV photovoltaic. ii, iv, v, 16, 29, 40, 44–52, 54, 55, 57, 60, 76, 81, 82, 90, 92–94, 106, 107, 109, 110, 131

QCLP quadratic constraint linear programming. 68

RESs renewable energy sources. ii, 6–8, 10–12, 18–22, 24, 28–30, 34, 35, 47, 57, 67, 81, 82, 90, 92, 111, 131, 132, 145

ROCOF rate of change of frequency. 24, 128–130

SD start down. 100, 101

SI Synthetic inertia. 128–130

SOC sate of charge. 39, 44–46, 56, 71, 72, 77, 98, 104, 108

SSCI system self-consumption index. 40, 44

SU start up. 100, 101

TOU Time of Use. 48, 54, 65

TSO Transmission System Operator. 23, 26, 27

TSRO two stage robust optimization. 67–69, 76, 79

UB upper bound. 68, 69

URFC Unitized regenerative fuel cell. v, 81, 92–94, 99–102, 107–110

V2G vehicle-to-grid. 29

VSC voltage source converter. v, 93, 94, 98, 99, 104, 106, 108–111

WTG wind turbine generator. 82, 90